



FRIEDRICH-SCHILLER-
UNIVERSITÄT
JENA

Palladium-Platinum nanoparticles: well-structured bimetallic catalysts for fuel cells

Dissertation

(kumulative)

zur Erlangung des akademischen Grades doctor rerum naturalium

(Dr. rer. nat.)

vorgelegt dem Rat der Chemisch-Geowissenschaftlichen Fakultät
der Friedrich-Schiller-Universität Jena

von M.Sc. Simon Tymen

geboren am 26.02.1985 in Clermont-Ferrand (Frankreich).

Gutachter:

1. Prof. Dr. Ulrich S. Schubert, Institut für Organische Chemie und Makromolekulare Chemie (IOMC), Friedrich-Schiller-Universität Jena
2. Prof. Dr. Michael Stelter, Institut für Technische Chemie und Umweltchemie, Friedrich-Schiller-Universität Jena

Tag der öffentlichen Verteidigung: 11 Juli 2018

Contents

Documentation of authorship	i
Introduction	1
1 Theoretical background	5
1.1 Proton-exchange membrane fuel cells	5
1.2 Thermodynamic of the reactions in fuel cells	7
1.3 The oxygen reduction reaction in PEMFC	11
1.4 Catalysts for the oxygen reduction reaction	16
2 One-step synthesis and analysis of PdPt nanoparticles: the influence of halides	21
2.1 Synthesis and physical characterization of the PdPt nanoparticles	22
2.2 Catalytic performances and stability of the particles	24
2.3 Study of the mass transport phenomena by impedance spectroscopy	30
2.4 The degradation	34
2.5 Conclusion	35
3 Core-shell palladium-platinum nanoparticles synthesized by galvanic replacement	37
3.1 The galvanic replacement: an innovative method for the synthesis of PdPt NPs	38
3.2 Evolution with the time of synthesis	38
3.3 Chemical properties and catalytic activity	45
3.4 Studies via impedance spectroscopy	54
3.5 Conclusion	58
4 Characterization and comparison of the particles via <i>in-situ</i> XAFS	59
4.1 Structure of nanoparticles after different times of synthesis	60
4.2 EXAFS measurements	61
4.3 <i>In-situ</i> measurements	63
4.4 Evolution of the structure in function of the potential	65
4.5 The relative concentrations and their changes followed by the ITFA	67

4.6 Catalytic performances of the particles	68
4.7 Conclusion	69
Abstract	71
Zusammenfassung	75
List of Abbreviations	79
References	81
Acknowledgements	89
List of publications	91
Declaration of Authorship / Selbstständigkeitserklärung	93
Publications	95

Documentation of authorship

This section contains a list of the individual contributions of authors to the publications present in this thesis.

P1)"Pt-Pd catalytic nanoflowers: Synthesis, characterization and the activity toward electrochemical oxygen reduction"
S. Tymen ¹, A. Undisz ², M. Rettenmayr ³, A. Ignaszak ⁴, *J. Mater. Res.* **2015**, 30, 2327-2339.

	1	2	3	4
Conception	X			X
Synthesis	X			
Characterization (TEM-EDS)	X	X		
Electrochemical experiments	X			
Impedance analysis	X			X
Correction of the manuscript	X	X	X	X
Supervision of S. Tymen				X
Proposal for crediting the publication equivalent	1.0			

P2) "From cubic palladium to concave core-shell platinum palladium nanoparticles: Evolution of their structure and the electrochemical properties",
S. Tymen¹, A. C. Scheinost², M. J. Lozano-Rodriguez³, C. Friebe⁴, U. S. Schubert⁵
J. Electrochem. Soc. **2018**, 165 (3) H67-H77.

	1	2	3	4	5
Conception	X	X			
Synthesis	X				
EXAFS	X	X	X		
Electrochemical analysis	X				
Correction of the manuscript	X	X		X	X
Supervision of S. Tymen				X	X
Proposal for crediting the publication equivalent	1.0				

P3) "*In-situ* XAFS Characterization of PtPd Nanoparticles synthesized by galvanic replacement"
S. Tymen¹, A. C. Scheinost², C. Friebe³, U. S. Schubert⁴, *Adv. Nanoparticles* **2017**, 6, 75-91.

	1	2	3	4
Conception	X	X		
Synthesis	X			
In-situ XAFS	X	X		
IFTA	X			
Electrochemical study	X			
Correction of the manuscript	X	X	X	X
Supervision of S. Tymen			X	X
Proposal for crediting the publication equivalent	1.0			

Erklärung zu den Eigenanteilen des Promovenden/der Promovendin sowie der weiteren Doktoranden/Doktorandinnen als Koautoren an den Publikationen und Zweitpublikationsrechten bei einer kumulativen Dissertation.

Für alle in dieser kumulativen Dissertation verwendeten Manuskripte liegen die notwendigen Genehmigungen der Verlage („Reprint permissions“) für die Zweitpublikation vor.

Die Co-Autoren der in dieser kumulativen Dissertation verwendeten Manuskripte sind sowohl über die Nutzung, als auch über die oben angegebenen Eigenanteile informiert und stimmen dem zu.

Die Anteile des Promovenden/der Promovendin sowie der weiteren Doktoranden/Doktorandinnen als Koautoren an den Publikationen und Zweitpublikationsrechten bei einer kumulativen Dissertation sind in der Anlage aufgeführt.

Name des Promovenden/der Promovendin	Datum	Ort	Unterschrift
M.Sc. Simon Tymen			

Ich bin mit der Abfassung der Dissertation als publikationsbasiert, d.h. kumulativ, einverstanden und bestätige die vorstehenden Angaben. Eine entsprechend begründete Befürwortung mit Angabe des wissenschaftlichen Anteils des Doktoranden/der Doktorandin an den verwendeten Publikationen werde ich parallel an den Rat der Fakultät der Chemisch-Geowissenschaftlichen Fakultät richten.

Name Erstbetreuer(in)	Datum	Ort	Unterschrift

Name Zweitbetreuer(in)	Datum	Ort	Unterschrift

Introduction

Today, in our society with the population spread all over the world using different means of transport, there is a high consumption of petroleum and gases. With limited resources and the problem of the climate change (in particular by the emission of gases produced by combustion motors), alternatives to petroleum and fossil fuel systems have to be developed. Electrical motors represent promising candidates to replace combustion motors, but the production and storage of electricity in vehicles is problematic. Different solutions and technologies are explored, based on electrochemistry, with the aim to develop a highly efficient conversion of the chemical energy to electricity. The development of new batteries and fuel cells, with a sufficient (electro)chemical performance is important to substitute the combustion engines. To be competitive, the devices require low cost, high performance, and long-term stability. In particular, the fuel cells receive more attention, with their high efficiency and low emissions of gaseous pollutants, they are good candidates to replace the combustion motors. The fuel cells are electrochemical devices with a direct and continuous conversion of the energy provided by the oxido-reduction reactions to electricity. The performance and stability of the cells are enhanced by choosing suitable catalyst materials. These materials contribute to the improvement of the efficiency of the oxido-reduction reaction and, hence, the conversion of chemical energy to electricity.

The fuel cell: History

The first fuel cells were invented independently by C. Schönbein, a German scientist and W. Grove, judge and amateur scientist, in 1839. They discovered that the reverse of electrolysis is possible and produces electricity. The electrolysis of water splits water molecules to hydrogen and oxygen when an electrical current is applied. The reverse process could be realized in a special cell with a suitable catalyst: this is a fuel cell.[1] In 1842, W. Grove mounted 50 fuel cells together and called it a gaseous battery. The term *fuel cell* was used for the first time by L. Mond and C. Langer for the preparation of the first practical cell using air and industrial coal gas in 1889. The actual research about fuel cells, with different materials (solids and liquids) for the electrodes, the electrolytes, and the gases, began in 1912 with E. Baur and his colleagues.[2] The first practical modern fuel cell was constructed by F. T. Bacon in 1932, with three decades of research to develop an effective working model. From the 1930s to the 1960s, important progresses were done with the first solid fuel cell (SOFC) in 1937, an improved molten-carbonate fuel cell (1946), an alkaline fuel cell (1954), and the proton-exchange membrane fuel cell (PEMFC).[3, 4] The space projects contributed to the accelerated development of PEM cells after 1950, with the projects of the NASA (project *Gemini*), where the PEM fuel cells were employed for the vehicles and the water produced by the cells as drinking water for long missions (1965).[5] The first car powered by a fuel cell, an A-40 Austin, was built in 1970 by K. Kordesch, and prototypes for buses and cars with passengers were tested in the 1990s. The Honda FCX is the first car approved for a commercial use in the USA in 2002. In 2008, the application of the fuel cell to power the airplanes was demonstrated by Boeing Research and Technology Europe.

Currently, five principal types of cells are existing [6]:

- 1 Proton-exchange membrane fuel cells (PEMFC) are based on the exchange of protons. The electrodes are separated by a selective proton-conductive polymer as electrolyte. The fuel is a chemical that is rich in hydrogen (H), like pure hydrogen gas (H_2) or methanol solution (CH_3OH), used in direct methanol fuel cells (DFMC), and the oxidant, which is rich in oxygen (O), like the air. These cells work from ambient temperature to 90 °C.
- 2 Solid-oxide fuel cells (SOFC) are utilized at 850 °C. The charges are carried by the oxide anions (O^{2-}) through a hard ceramic solid electrolyte of metal oxide like zirconium (Zr) or calcium (Ca). The presence of nickel (Ni) catalyzes the reaction at the anode.

- 3 Alkaline fuel cells (AFC) use generally a highly concentrated potassium hydroxide (KOH) solution (10 mol L^{-1}) as electrolyte and electrodes that are constituted of carbon covered by a catalyst (like platinum, Pt). The hydroxide anions OH^- are charge carriers and the fuel, hydrogen, must be pure for a good efficiency at $100 \text{ }^\circ\text{C}$.
- 4 Molten-carbonate fuel cells (MCFC) work at high temperature (650°C) with carbonates like sodium Na_2CO_3 or MgCO_3 , as electrolyte and carbonate anions (CO_3^{2-}) as charge carriers. These cells are highly efficient with nickel as catalyst but a high temperature is required and the carbonate anions of the electrolyte act as reactant; therefore it is necessary to add carbon dioxide as compensation.
- 5 Phosphoric-acid fuel cells (PAFC), where the electrolyte, the phosphoric acid, is contained in a silicon matrix and the electrodes, in graphite, are covered by a Pt catalyst to enhance the performance. The cells commercially used operate between 150 and $200 \text{ }^\circ\text{C}$.

To be competitive, the fuel cells require low cost, high performance, and stability over a long time. Currently, this is not possible for the PEM fuel cells due to the high quantity of platinum (Pt) used as catalyst for the oxygen reduction reaction (ORR). The Pt, an expansive transition metal, is the best catalyst for the main chemical reaction in PEM fuel cells. A diminution of the quantity of Pt in the fuel cells with the development of new materials to catalyze the chemical reactions (particularly the oxygen reduction reaction in PEMFC) could help to reduce the price of the cells and improve their performance, stability and life time.

Objectives

After a bibliographic and theoretical review about the oxygen reduction reaction (ORR), the bimetallic nanoparticles based on Pt used as catalyst in proton-exchange membrane fuel cells (PEMFCs) (Chapter 1), and the possibilities to realize the synthesis and characterization in our laboratory, we decided to work on the development of Pt-Pd bimetallic nanoparticles. The density functional theory (DFT) demonstrated that Pd is the second material of choice for the catalysis of the ORR in acidic solution.[7] The palladium (Pd) is a silvery-white transition metal (block d, group 10), atomic number (Z) 46 and with a molar mass of $106.42 \text{ g mol}^{-1}$, less expensive than Pt and with advantageous properties for the synthesis of bimetallic nanoparticles. Depending on the method of synthesis, the nanoparticles possess different shapes and chemical

compositions. To be competitive, the catalysts must be synthesized with a cheap and easy method, permitting to obtain well-structured and homogeneous materials. The synthesis in aqueous solution, with salts as metallic precursors, a surfactant, and the possible addition of halide anions (Br^- , I^- , Cl^-) is efficient to prepare different well-structured nanoparticles.[8–10] The characterization of the catalysts and the measurement of their performance and stability are essential to select the best materials for fuel cells. Studying PdPt nanoparticles with distinct structures, prepared following different methods, allowed the comparison of the methods and the particles. To see the influence of the experimental conditions during the synthesis, two synthesis methods were employed. First, the synthesis was done in one step with the simultaneous oxidation of Pt and Pd salt precursors. This permitted the preparation of PdPt nanoparticles with a dendritic shape and the investigation of the influence of the experimental conditions on the structure, composition, and electrochemical properties of the particles (Chapter 2). Core-shell nanoparticles with a core of Pd and a thin shell of Pt feature a high catalytic activity and stability for the ORR. These clusters could be prepared using a two-step method based on the galvanic replacement.[11, 12] Based on this method, the particles prepared after different times of synthesis, from pure cubic Pd nanocubes to concave cubic core-shell PdPt nanoparticles, were studied. The evolution of the structure and the electrochemical performance of the catalysts as function of the time of synthesis was examined (Chapter 3). A detailed analysis of the structure of the particles was possible using the X-ray absorption fine structure (XAFS) measurements performed at the European Radiation Facility (ESRF) in Grenoble (France). The formation and the dissolution of the oxide at the surface of the particles during the ORR was observed and analyzed after *in-situ* XAFS measurements at different potentials (Chapter 4).

Chapter 1

Theoretical background

1.1 Proton-exchange membrane fuel cells

Fuel cells are formed out of two compartments separated by a membrane. The main component of the PEMFC is a membrane-electrode assembly (MEA), a polymer electrolyte in contact with two electrodes, an anode and a cathode, on each side. The first membrane of the PEM was constituted by sulfonated polystyrene but rapidly replaced by per-fluorinated acidic polymers, like Nafion[®], a material with higher stability and better properties regarding the performance of the cells. Today, the majority of the electrodes of PEMFCs are made with carbon covered by one layer of catalyst to enhance the chemical reactions. Contrary to the battery, the fuel cell need an external source to work. In the anodic part of the cell, the fuel is the hydrogen gas, H₂ (or methanol for the direct methanol fuel cell, DMFC), and in the cathodic part, the fuel is an oxidant, namely air (containing oxygen O₂) for most of the cells. The conversion of the chemical energy to electricity is directly based on the electrochemical reactions in the cell via a constant flow (in) of the reactants and of the products (out). At the anode, the hydrogen is decomposed into protons passing through the proton-exchange membrane and the electrons arrive via an external circuit to the cathode, generating an electrical current. At the cathode, the oxygen reduction reaction and the recombination of protons with the reduced oxygen forms water (Figure 1.1).

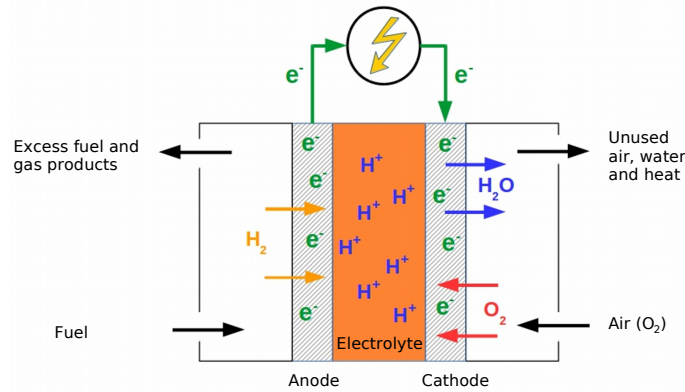
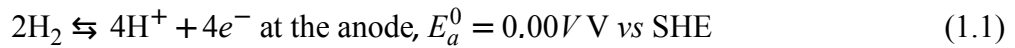


Figure 1.1 Simplified scheme of a PEM H₂–air fuel cell.

For the PEM based on hydrogen and air, two chemical reactions occur at the surface of the electrodes:



with a voltage of $E_0 = 1.23\text{V}$ at the equilibrium in standard conditions.

The splitting of hydrogen (H₂) to protons is easier with noble metals used as catalyst, especially Pt. The conduction of protons through the membrane requires material with selective proton-exchange properties and permitting an effective separation of hydrogen and oxygen on both sides of the cell. Currently, the perfluorinated acidic polymers are the main material for the membrane but still expensive and with problem concerning recycling. Researchers are working on new membranes, like hydrocarbon-type polymers and sulfonated aromatic hydrocarbon polymers, to reduce the price and to enhance the performance of the cells.[13] Contrary to the hydrogen, splitting the oxygen-oxygen double bond is hard, so the oxygen reduction reaction (ORR) is difficult and not possible in fuel cells without catalyst. In commercial fuel cells, the Pt is the best catalyst used for the ORR. But this metal is expensive, and before PEMFCs can be used for different applications, their price must decrease.

The production of low-cost and efficient fuel cells is a challenge. Today, many research groups are working on the development of new materials as catalysts for the ORR, trying to synthesize efficient catalysts with cheaper materials and excellent catalytic properties.

Different strategies are used to reduce the quantity of Pt in the cells and to improve their catalytic properties. The synthesis of bimetallic nanoparticles represents an interesting way to respond to the mentioned challenges.

1.2 Thermodynamic of the reactions in fuel cells

Basis of thermodynamic

Internal energy: The intern energy of a system, U , is the sum of the potential and the kinetic energy. It can be defined as

$$dU = dQ + dW \quad (1.4)$$

with Q corresponding to the heat (associated to the kinetic energy) and W corresponding to the work in the system (associated to the potential energy). The non thermal forms of the energy could be convert to an equivalent quantity of heat via the enthalpy (H).

Enthalpy: The enthalpy change (ΔH) represents the heat transfer into or out of a system at a constant pressure.

$$\Delta H = H_p - H_r \quad (1.5)$$

When the reactants r have more energy than the products p in a reaction, heat is produced and the enthalpy is negative, i.e. the reaction is exothermic. When the products have more energy than the reactants, it is necessary to furnish energy to maintain the chemical reaction, the enthalpy is positive, i.e. the reaction is endothermic.

Entropy: The entropy, S is a measure for the number of ways that the system can store energy. This is related to the structure of the system (ordered or disordered).

Gibbs energy: The Gibbs energy, G , describes the maximum of reversible work that can be performed by a system at constant pressure and temperature:

$$G = H - T \cdot S \quad (1.6)$$

The changes of the Gibbs energy, ΔG , permit to know whether a driving force for a reaction occurs. At constant pressure (p) and temperature (T), ΔG is simplified:

$$\Delta G = \Delta H - T \cdot \Delta S \quad (1.7)$$

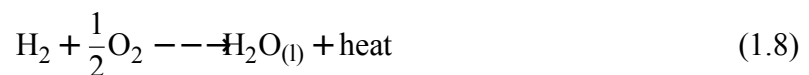
with $\Delta G < 0$ the reaction is spontaneous.

$\Delta G = 0$ equilibrium

$\Delta G > 0$ disfavored reaction (necessity to bring energy for the reaction)

Enthalpy in Fuel Cells

In fuel cells, the overall reaction between hydrogen and oxygen to form water is exothermic:



The final enthalpy of the reaction, $\Delta_R H_f$, is the difference of the enthalpy of formation of the products $\Delta_B H_p$ and the enthalpy of formation of the reactants $\Delta_B H_r$:

$$\Delta_R H_f = \Delta_B H_p - \Delta_B H_r \quad (1.9)$$

$$\Delta_R H_f = \Delta_B H_{\text{H}_2\text{O}(l)} - \frac{1}{2}\Delta_B H_{\text{O}_2} - \Delta_B H_{\text{H}_2} \quad (1.10)$$

By definition, the enthalpy of formation of the elements is equal to zero and the transformation from gas to liquid water at 25 °C is $286 \times 10^{-3} \text{ J mol}^{-1}$, so:

$$\Delta_R H_f = \Delta_B H_{\text{H}_2\text{O}(l)} \quad (1.11)$$

$$\Delta_R H_f = \Delta_B H_{\text{H}_2\text{O}(g)} - 286 \times 10^{-3} \text{ J mol}^{-1} \quad (1.12)$$

The negative value of the final enthalpy confirms that the overall reaction in fuel cells is exothermic at 25 °C with water produced in liquid form. During the formation of water by combustion of hydrogen, one mole of hydrogen (H_2) reacts with $\frac{1}{2}$ mol of oxygen (O_2).

Gibbs energy of the reaction

As we defined the Gibbs energy before, the change for the reaction in a fuel cell is:

$$\Delta_R G = \Delta_B G_{products} - \Delta_B G_{reactants} \quad (1.13)$$

$$= \Delta_B G_{H_2O} - \Delta_B G_{H_2} - \frac{1}{2} \Delta_B G_{O_2} \quad (1.14)$$

The changes of the Gibbs energy $\Delta_R G$ depend on the pressure p and temperature T , following the law:

$$\Delta_R G = \Delta_R G_0 - RT \cdot \ln \left[\frac{p_{H_2} \cdot p_{O_2}^{\frac{1}{2}}}{p_{H_2O}} \right] \quad (1.15)$$

with $\Delta_R G_0$ the Gibbs energy at standard pressure and temperature, R the universal gas constant, p_{H_2} the partial pressure of hydrogen, p_{O_2} the partial pressure of oxygen, and p_{H_2O} the partial pressure of water (gas).

A negative value of $\Delta_R G_0$ indicates that energy is released from the reaction. If the chemical reactions in a fuel cell would be fully reversible, all the Gibbs energy was converted in electrical energy, and the voltage of the cell was directly linked to the free energy:

$$\Delta_R G = -n \cdot F \cdot E \quad (1.16)$$

F is the Faraday constant, E is the voltage, and n the number of electrons per reaction. For a hydrogen fuel cell, two electrons pass by the external circuit ($n = 2$) and E is the thermodynamic (or reversible) voltage of the cell.

Working conditions and efficiency

For a reversible fuel cell, the reversible voltage (or Nernst voltage) is defined by the Nernst equation

$$E = \frac{-\Delta_R G}{nF} \quad (1.17)$$

$$E = \frac{-\Delta_R G_0}{2F} + \frac{RT}{2F} \cdot \ln\left[\frac{p_{H_2} \cdot p_{O_2}^{\frac{1}{2}}}{p_{H_2O}}\right] \quad (1.18)$$

As we saw before, the Gibbs energy of the fuel cell is dependent on the pressure and the temperature. Under standard conditions ($T = 25 \text{ }^\circ\text{C}$, $p = 1 \times 10^5 \text{ Pa}$), $\Delta_R G_0 = 237.10 \times 10^3 \text{ J mol}^{-1}$, so $E = 1.229 \text{ V}$.

In fuel cells, the input of energy is the enthalpy of the hydrogen (the reaction at the anode is spontaneous). Depending on the working conditions of the cell, the reversible voltage and the theoretical efficiency vary. Considering a perfect fuel cell, where all the Gibbs energy is converted in electricity, the maximum theoretical efficiency of the cell, η , under standard conditions, is defined by the equation:

$$\eta = \frac{\Delta_R G_0}{\Delta_R H_0} = \frac{237.1 \times 10^3}{286 \times 10^3} = 0.83 \quad (1.19)$$

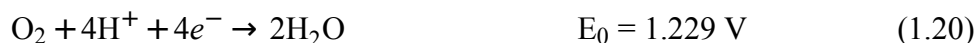
In reality, considering the production of heat, non-perfect chemical reactions and more, the PEM fuel cells with Pt as catalyst for the oxygen reduction reaction have an efficiency between 0.4 and 0.6.[14] Enhancing the efficiency of the oxygen reduction reaction is a priority regarding high performance for the fuel cells, for example by the development of new catalysts.

1.3 The oxygen reduction reaction in PEMFC

Mechanisms

The molecular oxygen reduction reaction (ORR) is an important reaction in biology, corrosion and energy conversion (fuel cells, metal-air batteries, solar cells). In the PEMFC, the cathodic ORR is essential to produce electricity and it is also the factor limiting the efficiency of the cells. The general scheme for the reaction follows two pathways: The direct four-electron reaction or the two two-electron reductions reactions including the formation of the hydrogen peroxide (H_2O_2) as intermediate.[15] In non-aqueous aprotic solvents, a reaction involving one electron could appear with the formation of oxygen super-oxide anions (O_2^-). When the four-electron mechanism occurs, in acidic medium, the oxygen is electrochemically reduced and the combination with protons permits the formation of water.

The overall equation for the four-electron process is:



And for the reduction with two electrons:



With the reactions in ideal conditions, the potentials are the thermodynamic potentials, E_0 .

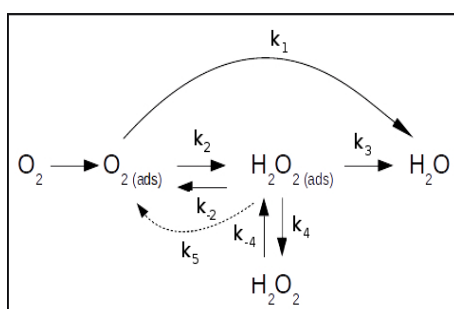
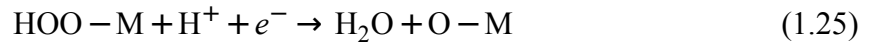


Figure 1.2 Schematic representation of the oxygen reduction reaction at a metallic surface.

The different simplified mechanisms of the ORR (Figure 1.2) show that the reduction of O_2 in PEMFCs follows different ways: The production of water, via a direct four-electron reduction with the rate constant k_1 and via a two-electron reductions. The adsorption and production of hydrogen peroxide adsorbed at the surface of the electrode (reaction rate k_2) reduced to water with the rate constant k_3 , desorption from the catalyst (reaction rate k_4) or re-oxidized to oxygen (reaction rate k_5).

With the very slow rate of the reaction, catalysts are necessary. The development of new materials with different structures enables the improvement of the kinetic and the reaction rate, and many investigations are realized about the ORR with different theoretical and experimental methods. After analysis and development of models and calculations using the density functional theory (DFT), two mechanisms, divided in elementary steps, were proposed: The associative one for the four-electron and the dissociative one for the two-electron reduction reaction.[16] Considering an ideal catalyst, the Gibbs energy of the reaction is close to the thermodynamic potential (1.229 V) at the equilibrium. The ORR with the four charges transfer may have a Gibbs energy for the reaction that is of the same magnitude and equal to the equilibrium potential.[7, 17]

The associative mechanism is divided in different steps for the charges transfer:



where the M corresponds to a chemical active site on the catalyst. The catalytic activity for this associative mechanism relies on the stability of the intermediates (O_2 , OOH , O , OH). Different scaling relationships were established among the oxygen intermediates. The activity is governed by a single parameter, depending on the binding energy of OH .[18] When the oxygen intermediates are too strongly bound, the rate determining step (RDS) is the removal of the hydroxide adsorbed into the surface of the catalyst (equation 1.27). For a material with a too weakly adsorption of oxygen intermediates, the activation of O_2 (equation 1.24) is the RDS.

For the second process, based on the transfer of two electrons, a dissociative mechanism is proposed:



Following these two mechanisms (associative and dissociative), under ideal conditions, there is no production of hydrogen peroxide. But considering the chemical processes presented in Figure 1.2 and the experimental results, H_2O_2 was detected as intermediate or final product, causing a decrease in the performance of the cells.[19]

Kinetic of the reaction

In fuel cells, the anodic reaction with hydrogen



is a fast reaction, 5 to 6 orders of magnitude faster than the reduction of oxygen in the cathodic part of the cell.[20] Thus, improving the kinetic of the oxygen reduction reaction is the main factor to increase the performance of the cells.

When a potential E is applied (or appears) between the electrodes, an overpotential, η , occurs defined as:

$$\eta = E - E_{Eq} \quad (1.33)$$

E_{Eq} is the equilibrium potential under ideal conditions for the ORR.

The dependence of the electric current and the potential at an electrode is described by the Butler-Volmer equation, considering reversible reactions (oxidation and reduction) at the surface of the electrodes:

$$j = j_0 \cdot \left[e^{\frac{(-\alpha)nF\eta}{RT}} - e^{\frac{(1-\alpha)nF\eta}{RT}} \right] \quad (1.34)$$

j is the current density, j_0 the exchange current density (A m^{-2}), α the charge transfer coefficients and n is the number of electrons exchanged during the reaction. F is the Faraday constant, R is the universal gas constant, and T is the temperature (in K). The current density, generated by the reactions occurring at the surface of the electrode, depends on the thermodynamic conditions of the system (pressure of H_2 and O_2 , temperature), the membrane of the cell, but also on the materials at the surface of the electrode. The exchange of charges is possible on the chemically active sites of the material at the surface of the electrode and is visible via the current density. The number of active sites is varying with the material and its shape, structure and chemical composition.[21–23] In PEMFCs, the current density is defined as negative at the anode and positive at the cathode. Applying the equation for the PEMFC:

at the anode (a):

$$j_a = j_{0, \text{H}_2} \cdot \left[e^{\frac{(-\alpha_H)nF\eta_a}{RT}} - e^{\frac{(1-\alpha_H)nF\eta_a}{RT}} \right] \quad (1.35)$$

and at the cathode (c):

$$j_c = j_{0, \text{O}_2} \cdot \left[e^{\frac{(-\alpha_O)nF\eta_c}{RT}} - e^{\frac{(1-\alpha_O)nF\eta_c}{RT}} \right] \quad (1.36)$$

where: j_{0, H_2} is the current exchange density at the anode (oxidation of the hydrogen), α_H the transfer coefficient of the rate determining step for the H_2 oxidation, j_{0, O_2} the current exchange density at the cathode (reduction of the oxygen) and α_O the transfer coefficient of the rate determining step for the O_2 reduction.

Without catalyst, the ORR is very slow and not viable to be used for many applications. The catalysts, mainly Pt and Pt-based materials, improve the reaction rate and the reaction is faster. Two limiting cases exist for this equation:

- Low overpotential ($\eta \approx 0$), the equation can be reduced to:

$$j = j_0 \cdot \frac{nF}{RT} \cdot \eta \quad (1.37)$$

- High overpotential: the equation can be considered as linear and is simplified to the Tafel equation:

The forward reaction,

$$j = j_0 \cdot \left[e^{\frac{(-\alpha n F \eta)}{RT}} \right] \quad (1.38)$$

can be rearranged:

$$\eta = \frac{RT}{\alpha n F} \cdot \ln(j_0) - \frac{RT}{\alpha n F} \cdot \ln(j) \quad (1.39)$$

$$\eta = a + b \cdot \log(j) \quad (1.40)$$

This is the Tafel equation assuming $a = \frac{2.303RT}{\alpha n F} \cdot \log(j_0)$ and $b = -\frac{2.303RT}{\alpha n F}$ for the forward reaction.

For the backward reaction

$$\eta = \frac{RT}{(1 - \alpha)nF} \cdot \ln(j_0) - \frac{RT}{(1 - \alpha)nF} \cdot \ln(-j) \quad (1.41)$$

$$\eta = a + b \cdot \log(-j) \quad (1.42)$$

with $a = \frac{2.303RT}{(1-\alpha)nF} \cdot \log(j_0)$ and $b = -\frac{2.303RT}{(1-\alpha)nF}$

With the Tafel equation, the exchange current density of the ORR is obtained by extrapolation of the linear function to the potential at the equilibrium, E_{Eq} . At the cathode, for the ORR, no electrical current is visible when the potential is higher than 1 V.

Actually, the maximum voltage of the PEMFC is 1 V (vs SHE). Different strategies are applied to study the kinetic of the ORR, like the constant application of a potential (steady state polarization) to calculate the reaction rate and the voltammetry (linear or cyclic), permitting to study the evolution of the current density with the potential and the monitoring of the kinetic of the reaction.

1.4 Catalysts for the oxygen reduction reaction

Today, an improvement of the oxygen reduction reaction is a key to enhance the performance of the PEMFC. The catalyst deposited at the surface of the electrodes are constituted by materials that possess favorable chemical properties towards the improvement of the ORR, with a higher reactivity and a faster kinetic, enabling the development of efficient cells. The platinum, a gray-white transition metal (atomic number $Z = 78$, block d, group 10 and a molar mass of $195.084 \text{ g mol}^{-1}$) with a face-centered cubic (*fcc*) crystalline structure shows the best catalytic properties for the reactions in fuel cells (hydrogen, formic acid, methanol oxidation and oxygen reduction).[17, 24] In combination with the chemical properties for the reduction of oxygen, the physical characteristics of the material are important. Rough and nanostructured surfaces with different morphologies are reported to be more active than flat surfaces.[25] A porous and nanostructured material possesses a larger chemical surface, with more active sites for the reaction, than for a macrostructured material with the macroscopic area. Hence, catalytic nanoparticles with a high surface area are ideal for fuel cells. Several types of nanoclusters with different sizes, shapes and materials are used, with a thin layer of the catalyst deposited on the electrodes. The crystalline structure and the shape of the Pt nanoparticles, with highly faceted orientation, is reported to affect their catalytic properties, whereas the Pt orientated (111) surface is the most stable and is present in many Pt and Pt-based nanoparticles.[26] Thus, it is very important to develop new methods to control the crystalline structure, the size and the morphology of the nanoparticles to prepare efficient catalysts. In parallel to pure systems, bimetallic (or trimetallic) particles are prepared and tested in fuel cells.[27] Bimetallic nanoparticles with different structures and sizes represent promising catalysts to improve the efficiency of the ORR. A different chemical composition, with two (or more) metals can conduct to new chemical properties like the selectivity for the chemical reaction and better catalysis, mostly due to a ligand effect. The most common metals used to prepare the Pt-based nanoparticles are Ru, Pd, Ni, Fe, Cu and Co.[28–33]

Synthesis of the Pt and Pt-based nanoparticles

Two distinct ways exist to prepare the nanoparticles. Firstly by physical methods via the fragmentation of bulk metals. Secondly by chemical process through the formation of the particles from molecular or ionic precursors.

The laser ablation is a physical method used to synthesize nanoparticles. To prepare the particles, a metallic precursor immersed in a liquid (water, acetone, methanol) is ablated by laser pulses at different frequencies and intensities, for a variation of the size and the shape of the particles.[34] Nanoparticles, directly coated on a support (graphene oxide), with high catalytic activities, are also produced by laser ablation.[35] The laser vaporisation on metallic (alloy) rod is done in an evaporation chamber. The presence of a helium or argon gaseous flow permits a deposition of well-formed Pt-Pd nanoparticles, directly on the support (α -Alumina).[36]

The chemical methods to prepare nanoparticles are mainly based on the reduction or oxidation of metallic precursors, electrodeposition and galvanic replacement in order to create particles with different structures (core-shell, alloys), size and chemical composition.[37–40] Contrary to the physical method (laser ablation), after the nucleation of the atoms of metal coming from the ionic or molecular precursors, the particles are growing. The usage of salts (hexachloroplatinate acid H_2PtCl_6 , potassium hexachloroplatinate K_2PtCl_6 , ammonium hexachloroplatinate $(NH_3)_2PtCl_6$, sodium hexachloroplatinate Na_2PtCl_6 , potassium tetrachloroplatinate K_2PtCl_4 ...) or organic precursors (platinum acetylacetonate, $Pt(acac)_2$) and their oxidation or reduction in different solvents (aqueous or organic) is possible. The polymers (hexadecyltrimethylammonium bromide (CTAB), poly(vinylpyrrolidone) (PVP)) that are usually present in the solvents are used as capping agent to stabilize and to prevent the agglomeration of the particles during the synthesis. A supplementary addition of ionic halides (bromide Br^- , iodine I^-) as shape controlling agent is also possible to receive variation of a specific crystalline surface orientation.[38] The time, the pH value, the concentrations of the different chemical species in solution, and the synthesis temperature enable to obtain different morphologies and compositions. Furthermore, there are differences between particles synthesized in a solution heated on an electric plate and the particles prepared using a microwave assisted heating method.[41]

For the methods based on the reduction of metallic precursors, different reducing agents, like ascorbic acid, citric acid and sodium borohydride ($NaBH_4$) are used.[37, 42, 43] After their reduction, the nucleation of the metals atoms begins and the particles grow. Depending of the experimental conditions (temperature, presence of halide, capping agent, stirring, and synthesis time), different structures are generated.

Preparation of Pt-based bimetallic particles based on the reduction of a metallic precursor

Bimetallic nanostructures revealed a high potential towards the development of less expensive catalysts with better performance and stability than the pure Pt. Using the density functional theory (DFT) and experimental tests, different bimetallic structures with several transition metals were investigated namely gold, rhodium, ruthenium, palladium, iron, copper, silver, and nickel.[31, 44–51] Thus, the usage of different experimental methods combined by chemical models (mostly created using DFT) is necessary to gain a better understanding of the chemical mechanisms during the synthesis, like the modification of the electronic structure induced by addition of a second metal, and during the catalysis (by the variation of the molar ratio between the metals, the properties of the catalyst change).[7, 52] Depending on the method of synthesis, different architectures are obtained for the bimetallic particles based on Pt. The principal structures are briefly presented below:

Heterogeneous structures

Heterostructures like dendrites are mainly prepared following the method based on the reduction of a metallic precursor and show a high catalytic activity. They are principally constituted of a dense array of Pt branches with the second metal as a core. Lim *et al.* synthesized Pt-Pd nanoparticles consisting of a core of Pd and dense branches of Pt with a catalytic performance five times higher than commercial Pt coated on carbon catalyst.[42]

Core-shell structures

Core-shell structures based on Pt are constituted by a core of metal surrounded by a Pt or Pt-rich active shell. The synthesis of such catalysts can be realized in one step by a co-reduction reaction. This method is based on the difference of the reduction potentials of the two metals. The reduction of the first metal cations is followed by the nucleation and growth of the core. With the reduction of the second metal, the growth of the shell is induced and the Pt-metal core-shell nanoparticle is structured. A well-controlled kinetic of the reaction is necessary to generate homogeneous and well structured core-shell nanoparticles.

These particles can also be prepared in two steps by successive reduction reactions like the seed-mediated growth method with a first synthesis of the core and the addition of a second metal to form the Pt-shell.[53] For a two-step approach, the galvanic replacement represents an attractive method: The first step is the synthesis of a seed with a less noble metal than Pt via the reduction of the metallic precursor (Pd, Ag or Cu) in a solution containing a reducing agent (ascorbic acid) and a capping agent (polyvinylpyrrolidone, PVP) with a possible addition of halides.[40, 54, 55] With the halides, the seeds are covered by anions, attracted by the high electronegativity of the fresh core metal. The presence of a surfactant (like PVP) prevents the formation of agglomerates. During the second step of the synthesis, the formation of a metallic shell begins after the introduction of the second metallic precursor. Two phenomena occur in parallel namely the dissolution of the first metal and the growth of a shell covering the core of the particles by deposition of the second metal. Specific surfactants and the presence of halides during the synthesis enable the selection of the chemical sites for the deposition of the second metal and so the preparation of clusters with a well controlled size, shape and crystallographic structure.[49, 56]

Alloys

Today, most of the alloys used as catalysts for the oxygen reduction reaction are binary, based on Pt and another transition metal, like Cu, Co, Ni, Pd and others.[57, 58] The preparation of an alloy is possible using a strong reducing agent (like sodium borohydride) to simultaneously reduce both metals, with a well-controlled kinetic for the reaction and with the selection of the right surfactant (like CTAB).[59]

Chapter 2

One-step synthesis and analysis of PdPt nanoparticles: the influence of halides

Parts of this chapter have been published in:

S. Tymen, A. Undisz, M. Rettenmayr, A. Ignaszak, *J. Mater. Res.* **2015**, *30*, 2327-2339.
DOI:10.1557/jmr.2015.212.

Among the different methods to prepare PdPt bimetallic nanoparticles, the synthesis based on the reduction of metallic precursors is of high interest. Controlling the morphology, the size and the chemical composition of the particles is essential for the creation of new catalysts for the ORR. The chemical composition and the presence of halides (Br^- , Cl^- , I^-) have a significant influence on the size and shape of the particles.[9, 38, 60] The stability of the material in acidic conditions is also important for an application in PEMFCs. Following a facile method supported by the reduction of Pt and Pd precursors, the particles were synthesized under different experimental conditions, aiming at the production of efficient and stable catalysts. Their morphology and chemical composition was studied by TEM-EDS correlated to their catalytic performance and stability (determined with electrochemical methods). Electrochemical impedance spectroscopy permitted a complementary study of the degradation phenomena.

2.1 Synthesis and physical characterization of the PdPt nanoparticles

Based on different articles, the particles were synthesized in aqueous solutions at low temperature avoiding a large amount of organic waste.[12, 61–63] For a typical preparation, an aqueous solution containing Pt and Pd metallic precursors (K_2PtCl_4 and Na_2PdCl_4) and a surfactant (hexadecyltrimethylammonium bromide, CTAB) to prevent the formation of agglomerates during the synthesis was used. After homogenization by sonication, the L-ascorbic acid was added as reducing agent and the solution was heated at $90^\circ C$ under magnetic stirring for 3.5 hours. The clusters prepared with this method are the reference sample, called 30 NPs. The reaction time was experimentally adjusted to prevent the formation of agglomerates. To study the influence of halides as shape control factor, potassium bromide (KBr) was added to the solution before the addition of the L-ascorbic acid and the synthesis was extended to 17 h. These particles are denoted as 60 NPs. To investigate the formation of particles with two metallic phases (labeled 45 NPs), a two-step method was used with the same reactants and concentrations. During the first step, the L-ascorbic acid was added to the solution with bromide and without Pt to reduce the Pd precursor. In a second step, the addition of the Pt metallic precursor (K_2PtCl_4) led to the reduction of the Pt precursor and to the formation of a shell of Pt over the Pd particles. The time of the reaction, as for the particles prepared in one step with bromide, was also 17 h. For all the electrochemical experiments, a typical powder with 20 wt. % of catalyst was made by a combination of a commercial black carbon powder and the particles.

Investigations on the structures of the particles (Figure 2.1) were realized by electronic microscopy. The observations made with a high resolution TEM coupled to a X-ray analyzer revealed different sizes nanostructured objects. For all the samples, the clusters morphology is similar to nanoflowers: A rough porous corona formed with an interconnection of Pt grains (size ≈ 3 nm) is covering a core, mainly constituted of Pd. The particles prepared without bromide and with simultaneous reduction of platinum and palladium (30 NPs) possess a cubic structure with an average size of 30 nm. With addition of bromide and a longer time of synthesis (60 NPs), the size of the particles increased to 60 nm. They also feature a more spherical shape and a more compact structure, with a more pronounced connection of the Pt grains. Agglomeration of the particles appeared after coating on the carbon support. The shape of the 45 NPs, prepared via the two-step method, is close to shape of the clusters fabricated in one step with bromide (60 NPs) but with an increased formation of large agglomerates.

2.1 Synthesis and physical characterization of the PdPt nanoparticles

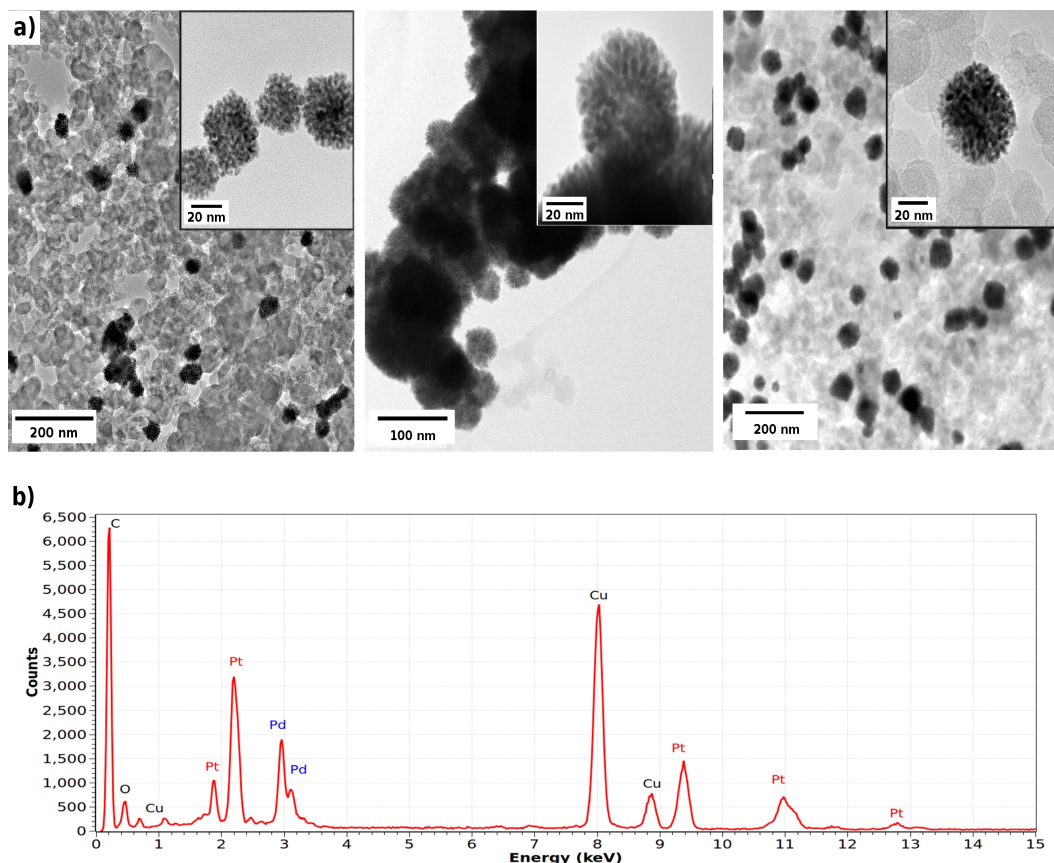


Figure 2.1 a) TEM images of the particles on carbon support: 30 NPs (left), 45 NPs (middle), 60 NPs (right). The insets (with a high magnification) show the pure particles. b) Typical EDS spectrum for the 45 NPs.

Concerning the morphology of the clusters, no significant impact of bromide was observed besides a shape that is a little bit more spherical. The density of particles is affected by the bromide with more compact nanoflowers. Similar structures were reported by other groups.[64] EDS measurements confirmed the presence of Pt and Pd for all the particles (Figure 2.1), with the core mainly constituted of Pd and the corona formed by Pt grains. Some trace of bromide coming from the synthesis and a copper contamination due to the TEM support were also detected. The EDS mapping on individual particles revealed the following chemical compositions: 60 wt. % of Pt and 40 wt. % Pd for the 30 NPs, 55 wt. % Pt and 45 wt. % Pd for the 45 NPs and 67.5 wt. % Pt and 32.5 wt. % Pd for the 60 NPs. With a theoretical weight ratio Pt:Pd of 1, the particles 45 NPs were the closest to the aspired stoichiometry. The different chemical compositions for the 30 NPs and the 60 NPs could be due to the precipitation of small particles (≈ 5 nm) only composed of Pt (Figure 2.1).

2.2 Catalytic performances and stability of the particles

Electrochemically active surface area and mass activity for the oxygen-reduction reaction

The electrochemically active surface area (ECSA) of the particles was determined following the method of the deposition of hydrogen under potential. This method is based on the adsorption/desorption of the hydrogen in dependence of the potential applied to the system.[65] The charge of the monolayer of hydrogen, varying with the adsorption/desorption on the metallic surface, was calculated by the integration of the peak between 0.05 and 0.4 V visible in the cyclic voltammograms (Figure 2.2).

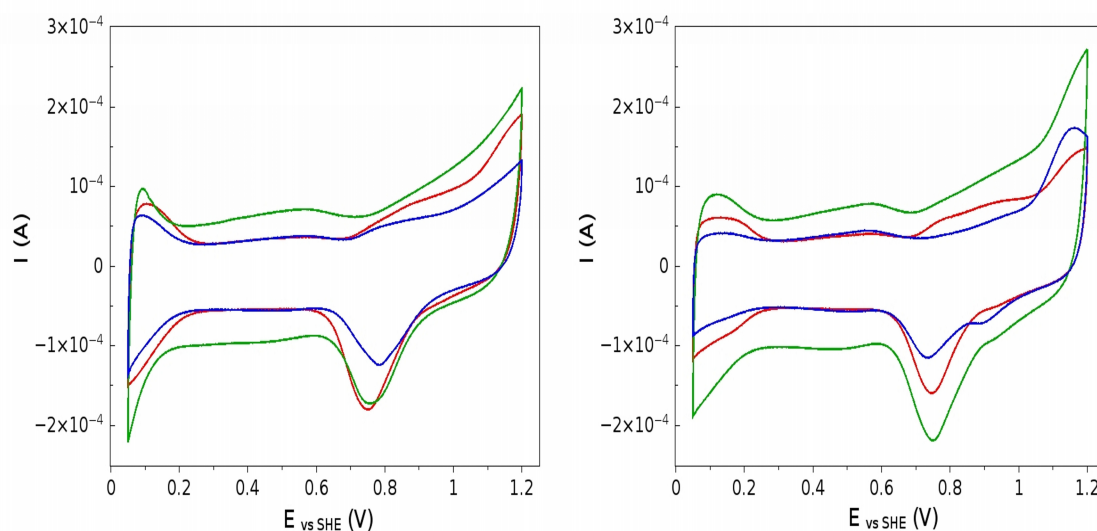


Figure 2.2 Cyclic voltammograms to measure the ECSA of the catalysts before (left) and after the degradation (right): 30 nm (red), 45 nm (green), 60 nm (blue).

The charge of the hydrogen activity was calculated according to the equation:

$$Q_H = \frac{\int i dE}{\nu} \quad (2.1)$$

where i is the current (A), E the potential (V), and ν is the scan rate (20 mV s^{-1} here).

Additionally, the chemically active surface area ($\text{m}^2 \text{ g}^{-1}$) was determined by comparison of the experimental catalysts (nanoparticles) and the theoretical charge of the hydrogen adsorption on

polycrystalline Pt ($2.1 \times 10^{-4} \text{ C cm}^{-2}$) and normalized to the mass of deposited metal on the electrode. The following equation was used to determine the electrochemical surface area of the nanoparticles:

$$ECSA = \frac{1}{2.1 \times 10^{-4}} \cdot \frac{Q_H}{m_{(PdPt)}} \quad (2.2)$$

with m_{PdPt} is the mass of the catalyst deposited on the glassy carbon electrode and Q_H is the previously calculated charge of the hydrogen (Eq 2.1).

The ORR measurements were performed by linear sweep voltammetry (LSV) using a rotational disk electrode (RDE, with a geometric area of 0.196 cm^2) and a rotation speed of 1600 rpm. After the experiments, three characteristic regions, representing the principal chemical phenomena controlling the system, were visible in the voltammograms (Figure 2.2): from 0.35 to 0.7 V, the mass transport is dominant, followed by a mixed mass transfer-kinetic between 0.7 and 0.85 V, and a pure kinetic-controlled region above 0.85 V. With the rotation of the electrode, the resulting convection ensures a fast transport of the redox active species from the electrolyte to the surface of the electrode.

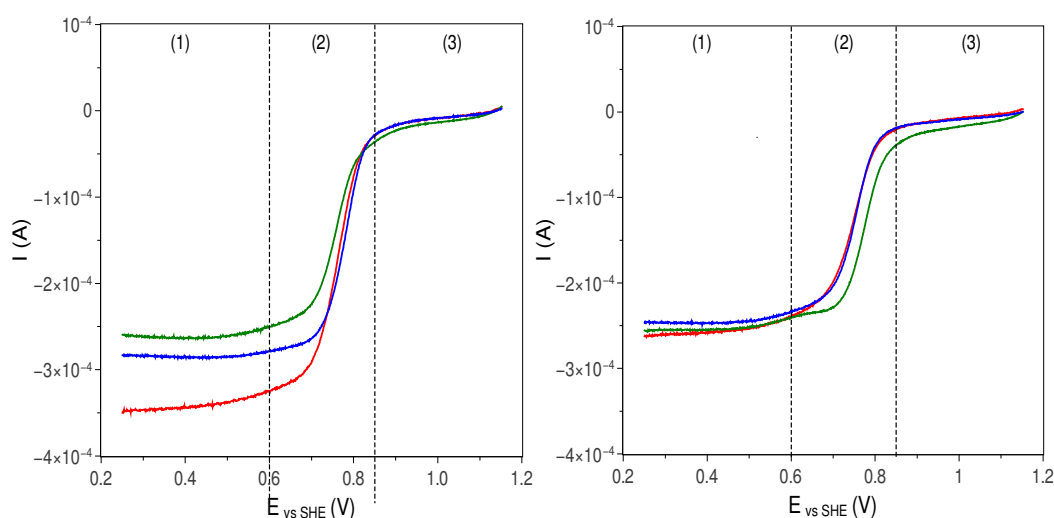


Figure 2.3 Linear sweep voltammograms before (left) and after (right) stability tests for the oxygen reduction reaction (1600 rpm): 30 NPs (red), 45 NPs (green) and 60 NPs (blue) and the different area controlling the reaction: (1) Mass transfer, (2) mixed mass transfer-kinetic and (3) kinetic.

The mass activity (the kinetic current density normalized to the mass of catalyst, $A \cdot g^{-1}$) was calculated using the Koutecky-Levich equation (neglecting the Nafion film diffusion-limited current density):

$$\frac{1}{j} = \frac{1}{j_k} + \frac{1}{j_d} \quad (2.3)$$

with j as total current density, j_d the diffusion limited current density (mass transport) and j_k the kinetic current density.

Considering the evolution of the current density with the potential (Figure 2.3), the mass activity was calculated using the values of the current density measured at 0.85 V and the diffusion limited current density at 0.4 V.

The ECSA and the mass activity of the different particles were compared to a commercial catalyst (Pt coated on carbon XC72R powder, 20 wt. % Pt). The stability of the particles was studied by cyclic voltammetry (CV), via measurement of the ECSA before and after 2000 cycles. The voltammograms of the ECSA (Figure 2.2) showed a well-defined peak between 0.05 to 0.3 V corresponding to the adsorption/desorption of the hydrogen on the surface of the catalyst (Pt and Pd surface). The intensity of the peak depends on the size of the particles, with the higher ECSA for the largest particles (60 nm). The ECSA measured for the synthesized particles was similar to the ECSA of 30 nm pure Pt nanoparticles but lower than the commercial Pt catalyst (Pt/C) used for comparison (formed with small nanoparticles, ≈ 5 nm).[66] After the stability test, a degradation of the performance was visible, excepted for the 45 NPs which possessed an ECSA significantly higher after 2000 cycles (Table 2.1). This increase may be attributed to modifications at the surface of the electrode during the electrochemical cycling with an "electrochemical cleaning", washing the CTAB surfactant still present at the surface of the particles. The degradation of the particles can be explained by the dissolution of Pt and the agglomeration of metals (Ostwald ripening) created by the electrochemical scanning with a potential higher than 1.2 V.[67] The results after the stability test (Table 2.1) showed a smaller decrease (19.5 %) for the small particles (30 nm), while the particles with a size of 60 nm lost 60 % of the ECSA under the same chemical conditions. Concerning the size effect, opposite results could be expected, considering a faster dissolution of Pt for the small nanoparticles.[68] However, also the formation of Pt oxide (PtO), Pt hydroxide (PtOH) and Pt dioxide (PtO₂) occurred and the accompanying passivation of the surface tended to be higher for the larger particles.

It is commonly admitted that the position of the peak corresponding to the reduction of the Pt-O has an influence on the ORR. When the peak is shifted to higher potentials, it signifies a weakening of the bonding between the catalyst and the oxygen species and, therefore, an increase of the ORR specific activity. Furthermore, an impact of the chemical composition (particularly at the surface) on the Pt dissolution was observed during the study. A correlation between a higher content of Pd for the 60 NPs (Pd:Pt = 67.5:32.5) and the faster degradation for the 60 NPs was indicated. This can be due to a faster electrochemical dissolution in the presence of Pd at the surface of the particles during the anodic part of the scan, at potentials lower than 0.8 V.[69]

The 45 NPs (Pt:Pd = 50:50) were not expected to be the most stable (Table 2.1). Their high stability could come from a restructuring at the surface of the catalyst upon polarization under acidic conditions (with a positive effect here) or the electrochemical reduction of the oxidized metal at the surface which was generated during the synthesis due to a long time at high temperature.[70] Furthermore, the passivation of the surface (and not the bulk), a reverse process confirmed by the highest initial mass activity for the 45 NPs, may be the reason. Moreover, the ECSA of the 45 NPs was also associated with the synthesis method, with a primary step to form a colloid constituted of Pd, forming nucleation centers for the Pt atoms in a second step. These conditions could also lead to the formation of Pt-Pd alloys at the surface of the particles stabilizing the clusters.[71] In addition to the highest stability, the fresh 45 NPs had also the best mass activity for the ORR. This indicates the presence of possible alloy, with a higher catalytic performance than pure Pt.[72] The enhancement of the mass activity in a Pt-Pd alloy comes from the *electronic effect*, associated to a different electronic distribution for the Pt and Pd atoms or by a geometric effect with different interatomic distances between the Pt and Pd atoms.[73] For a cluster constituted by an alloy, charges appear, with negatively charged Pt atoms in combination with positively charged Pd atoms. This is due to a shift of electrons from the Pd to the Pt, with a higher electronic density around the Pt atoms and, hence, an increasing vacancy of the Pt *d*-band orbital.[74, 75] Consequently, the adsorption and dissociation of the molecular oxygen is easier on the Pt surface leading to a faster oxygen reduction.[72] Taking into account the mass activity and the stability of the 45 NPs, a full protection of the Pd by the Pt atoms is indicated, blocking access to catalytic sites of the particles for the redox-active species. Recent theoretical calculations demonstrated that only two atomic layers of Pt on the surface of another metal are sufficient to prevent the electrochemical cleaning.[76]

Kinetic study

As demonstrated in Chapter 1, the ORR is a multi-electron process divided in elementary steps through different reaction intermediates.[3] Concerning the kinetic, we assumed that one single step is slower than the others, and controls the rate of the overall reaction. This rate determining step (RDS) is most likely a heterogeneous electron transfer which is strongly influenced by the surface of the particles. For potentials higher than 0.8 V, a mix of Pt and Pt oxide is formed while at lower potentials an oxide-free surface is present.

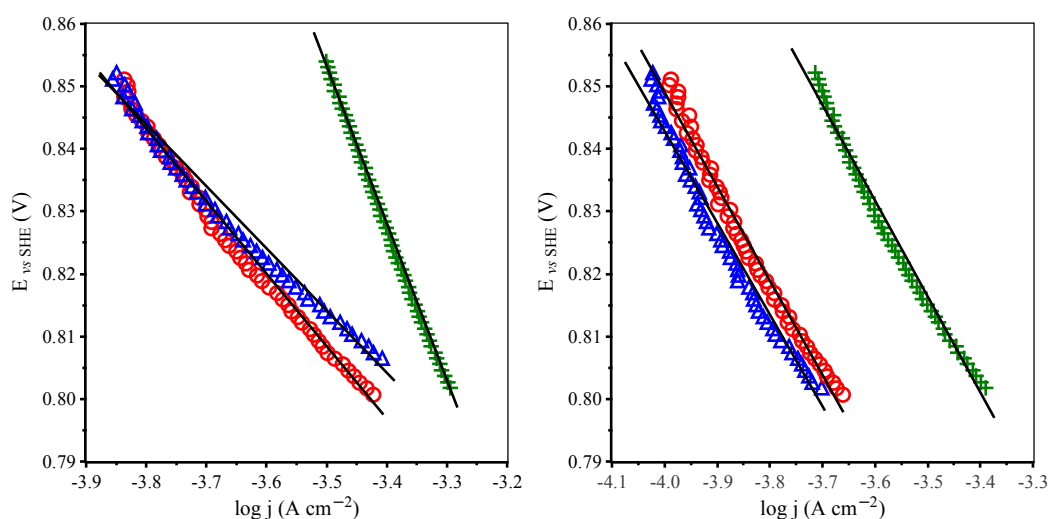


Figure 2.4 Tafel plots for the 30 NPs (red), 45 NPs (green) and 60 NPs (blue) as prepared (left) and after degradation (right).

So, the potential affects the kinetic of the reaction. The kinetic can be studied via the determination of the exchange current density on an electrode, which can be realized by monitoring the relation between the potential E , and the logarithm of the current density j , $E = f(\log|j|)$ using the simplified Tafel equation (Chapter 1):

$$E = a + b \times \log|j| \quad (2.4)$$

The exchange current density, j_0 , is determined with the experimental Tafel plot ($E = f(\log|j|)$) by extrapolation of the Tafel line to the equilibrium potential (Figure 2.4). There are two different current exchange densities one at low and the one at high potentials. The values of the exchange current densities on Pt reported in the literature show large variations and depend

2.2 Catalytic performances and stability of the particles

primarily on the structure of the clusters. On a surface constituted of Pt and Pt oxide, the RDS of the reaction is a pseudo two-electron transfer with a Tafel slope of 60 mV dec⁻¹. For the oxide free surface, only constituted of Pt, the RDS is the first electron transfer, with a Tafel slope of 120 mV dec⁻¹. With our bimetallic PdPt samples, the Tafel slope was close to 120 mV dec⁻¹ (Figure 2.4), suggesting a first transfer reaction as the RDS:



The initial higher value for the 45 NPs indicates a possible influence of the mass transport, maybe induced by changes and restructuring at the surface of the catalyst. However, this did not affect the mass activity. After the degradation test, the values of the Tafel slopes were similar, indicating no change of the ORR process. The highest values of the exchange current density for the 45 NPs, fresh and degraded, agreed with the best mass activity calculated at 0.85 V (Table 2.1). This allowed the hypothesis of a faster electron transfer rate, favored by a possible formation of an alloy for the 45 NPs.

Table 2.1 Electrochemical surface area and kinetic parameters: Mass activity, exchange current density and Tafel slope for 30 NPs, 45 NPs, 60 NPs samples together with the commercial Pt/C reference.

Sample	ECSA (m ² g ⁻¹)	ORR mass activity at 0.85 V (A g ⁻¹)	Tafel slope (mV dec ⁻¹)	j ₀ × 10 ⁻⁴ (A cm ⁻²)
Fresh samples				
30 NPs	16.22	3.18	116.30	3.81
45 NPs	7.57	4.14	252.60	5.21
60 NPs	10.70	3.24	93.70	4.71
commercial Pt/C	32.60	2.80	-	-
Degraded samples				
30 NPs	13.05	2.19	151.60	2.21
45 NPs	11.01	4.55	151.00	4.25
60 NPs	4.42	2.10	151.10	2.01
commercial Pt/C	26.30	2.30	-	-

2.3 Study of the mass transport phenomena by impedance spectroscopy

Electrochemical impedance spectroscopy (EIS) was carried out to study the mass transport at 0.5 V, in the region where the mass transport is predominant. The measurements were performed using a RDE (1600 rpm) to ensure a defined transport of the reactants to the surface of the electrode. In the resulting Nyquist diagrams, the shape of the curves suggested the theoretical shape corresponding to a Randles electric equivalent circuit.[77, 78] This circuit (Figure 2.5, left) is used to model the phenomena of transfer, accumulation, and diffusion of charges, in particular when the mass transport is predominant.

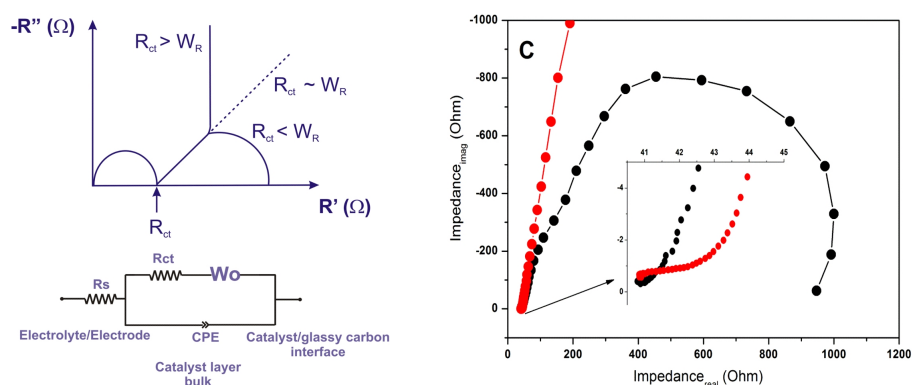


Figure 2.5 Theoretical Nyquist diagram with equivalent circuit (left) and experimental plot (right), (0.508 V, 1600 rpm), fresh (red) and after degradation (black).

For the theoretical Nyquist diagram, an arc at high frequencies is characteristic for the resistance of the electrolyte (R_s) in serie with the combination of the resistance (Faradic) to the charge transfer (R_{CT}), a Warburg element (W_0) representing the diffusion of the charges and a non ideal capacitor (CPE), to model the ionic accumulation at the electrolyte/electrode interface. A line starting at about 50 Ohms with an angle close to 45° , indicates the predominance of the mass transport phenomena.

Depending on the diffusion of charges, W_0 -R, a parameter of the Warburg element, is the electrical component used to represent the diffusion phenomena and the resistance of the diffusion. As represented in the Figure 2.5, when the resistance of the diffusion is smaller than the charge transfer, the straight vertical line at low frequencies represents an accumulation of charges

2.3 Study of the mass transport phenomena by impedance spectroscopy

(capacitor). In the opposite case, a semi-circle, appears at low frequencies, corresponding to a finite diffusion of the charges.

The experimental EIS spectra were fitted with the Randles circuit as equivalent circuit, providing the values of the electrical components for the different samples. The fitting was done assuming a homogeneous structure for the film of catalyst deposited at the surface of the electrode, with the key role of the interface electrolyte-film (macroscopic boundary). The ionic transport was modeled by diffusion along the bulk, without separation of the different fractions (Nafion, carbon, catalyst). In the Nyquist diagram, for all samples, the principal shape of the curves stay the same, either unchanged or modified at low frequencies, from capacitive loop (straight line at 90°) to finite-length diffusion (semi-circle) after the degradation. The plot of the admittance, Y , the inverse of the impedance ($Y = Z^{-1}$) is useful to graphically separate the kinetic and diffusion phenomena.

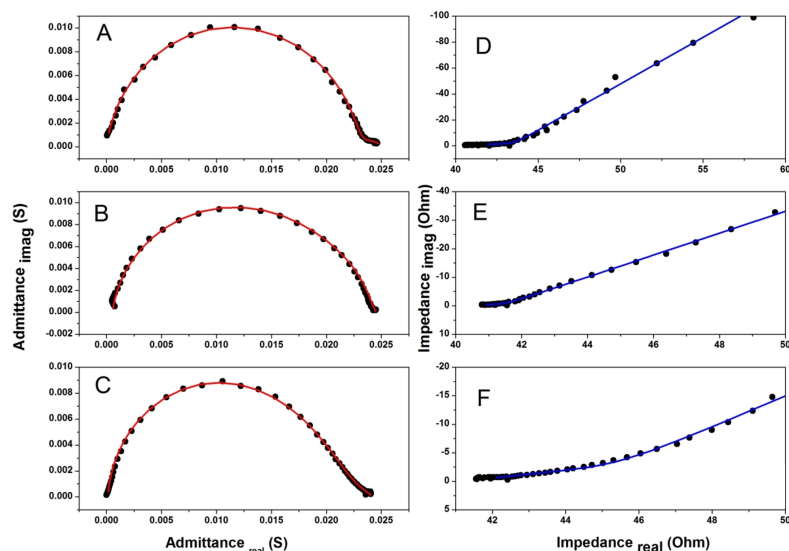


Figure 2.6 Admittance (a-c) and impedance (d-f) recorded at 0.5 V, 1600 rpm, with Warburg phenomena. Experimental scatter (black) and fitting (red and blue). 60 NPs: Plot (a) and (d), 30 NPs: Plot (b) and (e), 45 NPs: Plot (c) and (f).

In the first part of the Figure 2.6 (a, b and c), with the admittance of the samples (black points) and the fitting (red lines) an easy separation of the kinetic and diffusion was visible. The second part of the Figure 2.6 (d, e, f) shows the impedance for a restricted frequency range corresponding to the predominant role of the Warburg impedance.

The total impedance of the equivalent circuit, Z_t is defined by

$$Z_t = Z_{R_s} + Z_{(CPE, R_{CT}, W)} \quad (2.6)$$

where R_s is the resistance of the solution, R_{CT} the resistance of the charge transfer, W_0 is the Warburg element, and CPE the non ideal capacitor, representing the ionic accumulation at the interface electrode-electrolyte.

The resistance of the solution can be estimated from the Nyquist diagram at the intersection between the semi-circle and the abscissa (left part of the graph). It was the same for all the samples, without any changes after the degradation test. The charge transfer resistance was determined from the width of the semi-circle (Figure 2.5). The numerical values determined by fitting for all the components of the equivalent circuit are presented in Table 2.2. Before the degradation, the resistances for the charge transfer, linked to the rate of oxygen reduction, were similar for the 30 NPs and 45 NPs but higher for the 60 NPs. The chemical composition of the particles, with a higher content of Pt for the 30 and 45 NPs decreased the resistance for the charge transfer.

At 0.5 V, the diffusion was the rate determining step and the number of exchanged electrons (calculated by Levich equation) was close to one, indicating that the reactions 2.11 and 2.12 were dominant and the process fully depends of the rate of the oxygen at the surface of the electrode in the multi-step process controlled by the diffusion.[3]



The charge-transfer rate for each step (i), $R_{CT (i)}$ is defined as $R_{CT (i)} = n_i \cdot \nu_i$ where n_i is the number of electrons exchanged and ν_i the reaction rate for each step ($\text{mol cm}^{-2} \text{s}^{-1}$).

Based on this hypothesis, it can be established that for the smallest value of R_{CT} , the number of exchanged electrons should be close to one for the reaction 2.10.[79]

2.3 Study of the mass transport phenomena by impedance spectroscopy

The constant of the reaction rate was evaluated following the mathematical model defining the diffusion resistance, Z_{W_o} by:

$$Z_{W_o} = R_{W_o} \cdot \frac{\coth(j \cdot \tau \cdot \omega)}{(j \cdot \tau \cdot \omega)} \quad (2.13)$$

where P is a dimensionless factor, ω the angular frequency and τ the surface relaxation time, linked to the different steps of the oxygen reaction (Equation 2.9 to 2.12), dependent on the potential. τ depends on the diffusion coefficient D and the diffusion length L :

$$\tau = \frac{L^2}{D} \quad (2.14)$$

τ^{-1} , the inverse of the coverage relaxation time, is equivalent to the first order rate constant for the desorption of the ORR intermediates, depending on the potential.[80] The different values of the diffusion parameters are presented in Table 2.2.

Table 2.2 Values for the different electrical components of the equivalent circuit after the fitting to the experimental spectra and derived kinetic parameters (0.5 V, 1600 rpm).

Sample	R_{CT} (Ω)	T (F) $\times 10^{-3}$	R_{W_o} (Ω)	τ (s) $\times 10^{-3}$	W_o -P (l)	τ^{-1} (s^{-1})	L (cm) $\times 10^{-4}$
Fresh samples							
30 NPs	1.86	1.35	2.78	16.1	0.41	62.11	5.88
45 NPs	2.11	2.63	2.81	1.57	0.42	636.94	1.83
60 NPs	4.33	4.54	7.34	12.8	0.45	78.12	5.24
Degraded samples							
30 NPs	1765.00	1.48	3.99	28.00	0.42	35.71	7.75
45 NPs	23.32	3.22	5.22	1.72	0.43	581.39	1.92
60 NPs	2231	1.63	5.10	92.80	0.43	10.77	14.1

All the particles possessed similar and small values for the mass transport resistance, which are close the charge-transfer resistance. This demonstrates that the accessibility of the catalytic active sites was similar for all the samples, confirming that the morphology of the particles (size,

shape, and distribution on the carbon support) were not critical. In contrast, the relaxation time constant for the 45 NPs was almost one order of magnitude smaller than for the other samples, accompanied by a higher effective diffusion length. For the higher values of the reaction rate constant, the surface relaxation time was shorter, revealing that the surface recovery for the reaction intermediates was fast.

Comparing the structures of the particles, in particular the surface roughness (visible on TEM pictures, Figure 2.1), the sample 45 NPs was more compact, which most likely led to a lower ECSA compared to the other particles (Table 2.1). However, the reaction rate constant was the highest and the relaxation time the shortest for this sample. As a consequence, for the 45 NPs, a stronger electronic effect for the O₂ adsorption and dissociation is expected. [72, 81] As a result of the analysis of the diffusion parameters, we assumed that the mechanism of the mass transport was similar for all the samples but favored for the 45 NPs due to a possible Pd-Pt alloy on the nanoparticles.

The pseudo capacitance (T), is defined by

$$Z_{CPE} = T^{-1} \cdot (j \cdot \omega)^{-n} \quad (2.15)$$

where T is the pseudo capacitance, n is a dimensionless factor (between $0 < n < 1$, with 1 for the perfect capacitor, between 0.95 to 0.98 here). [82] The pseudo capacitance is directly linked to the ECSA and, therefore, to the size and structure of the particles. After the synthesis, like for R_{CT} , T evolves with the size of the particle, increasing with the size of the cluster. The size of the particles is not the main factor for the ECSA with the smaller value for the 45 NPs.

2.4 The degradation

Different mechanisms are proposed to explain the electrochemical instability of the particles (cf Table 2.1 and 2.2). Theoretical and experimental studies suggest the degradation of the particles is linked to the mechanisms of the dissolution of the Pt layer at the surface of the particles in solution. These mechanisms, governing the reduction of the ECSA, are the most accepted ones.[83] They are based on the formation of Pt oxide between 0.9 and 1.2 V, followed by the dissolution of the oxidized Pt.[84]

For the 45 NPs, in the Figure 2.3, for the degraded samples, the peak related to the reduction of the PtO was at a higher potential after the degradation, conducting to a stable mass activity and/or higher ECSA (Table 2.1). This was again indicating that a different electronic structure for these clusters (modification of the orbital d for the atoms of the bimetallic particles) controlled the adsorption of the oxygen species.[85] The introduction of Pd, leading to the formation of bimetallic particles, can diminish the oxidation of the Pt, thus reducing its dissolution and finally increase the stability of the clusters.[86] For the impedance parameters, significant changes for R_{CT} and the Warburg parameters (Table 2.1) occurred, with a really high increase of the R_{CT} for the 30 NPs and 60 NPs. No critical changes for the pseudo capacitance of the CPE appeared, revealing that the morphological changes for the particles are negligible, despite of the decrease of the ECSA for the 30 and 60 nm clusters. To sum up, the 45 NPs had the best electrochemical stability under the accelerated degradation tests, again a possible indication of a Pt-Pd alloying.

Briefly, for the electrochemical stability, the critical factor is apparently the chemical composition of the surface of the catalysts. There is a better stability when the quantity of Pt within the surface increases, protecting the Pd from leaching out (with a confirmation of the distribution of the Pt and Pd resolved by EDS mapping). Furthermore, the catalyst curvature and the degree of alloying have a significant influence.

2.5 Conclusion

Regarding the ECSA, the size of the particles, between 30 and 60 nm, had no influence while the curvature and the chemical composition of the particles (particularly at the surface of the catalyst) was an important factor. The 45 NPs with a nanoflower structure were the best catalysts for the ORR, possibly favored by a Pt-Pd alloy formation, permitting an enhancement of the O_2 adsorption and dissociation, explained by the *electronic effect*. The kinetic experiments confirmed these results with higher exchange current densities for these particles. The electrochemical impedance studies demonstrated that the 45 NPs possessed the shortest effective diffusion length and the highest reaction rate constant among all the morphologies, agreeing that the curvature of the catalyst supports the transfer of the reactant to the chemical active sites (for the fresh and degraded samples).

The charge transfer resistance, R_{CT} , of the 45 NPs remained small after the degradation test, showing a great stability of the clusters, due to its rigid and active structure with a surface rich in Pt. Regarding the other samples, a significant increase of the R_{CT} appeared after the stability test, revealing a degradation potentially explained by a smaller quantity of Pt at the surface of the clusters.

Chapter 3

Core-shell palladium-platinum nanoparticles synthesized by galvanic replacement

Parts of this Chapter have been published in:

S. Tymen, A. C. Scheinost, M. J. Lozano-Rodriguez, C. Friebe and U. S. Schubert, *J. Electrochem. Soc.* **2018**, 165 (3) H67-H77. DOI: 10.1149/2.0021803jes.

Besides PdPt nanoparticles with a structure of nanoflowers (Chapter 2), core-shell nanoparticles, are the most promising catalysts for fuel cells. With a method based on the galvanic replacement, we followed the evolution of the structure, size, nature of the chemical Pt-Pd bond, chemical composition and catalytic activity in function of the time of synthesis. Pure Pd nanocubes and PdPt clusters with an increasing time of synthesis are compared. X-ray diffraction spectroscopy (XRD) and extended X-ray adsorption fine structure (EXAFS) measurements permit to determine the crystalline structure and the chemical binding between the Pt and Pd atoms for the different particles.

3.1 The galvanic replacement: an innovative method for the synthesis of PdPt NPs

The galvanic replacement is particularly attractive for the synthesis of PdPt core-shell nanoparticles. Controllable by the capping agent and the presence of halides, different structures (core-shell, nanorods, nanocages ...) of PdPt nanoparticles can be prepared.[8, 12, 87] Inspired by the method of Zhang *et al.*, the Pt metallic precursor, the potassium tetrachloroplatinate (K_2PtCl_4) was used. After a first preparation of Pd nanocubes, PdPt core-shell nanoparticles were prepared using different times of synthesis. To control the chemical sites for the adsorption of Pt, KBr was present in the solution of sodium tetrachloropalladate (Na_2PdCl_4) used as Pd precursor and the polyvinylpyrrolidone (PVP) as capping agent. After the synthesis of the Pd cluster, the Pt precursor (K_2PtCl_4) was progressively added (1 mL min^{-1}) to the solution and the different synthesis times were selected (0.6 h, 2 h, 4 h, 6 h, 8 h and 17 h) to follow the evolution of the physical and chemical properties of the particles. After the synthesis, the particles, collected by centrifugation, were rinsed several times with water and ethanol and then coated on carbon (Chapter 2).

3.2 Evolution with the time of synthesis

Changes in morphology: TEM and EDS study

The particles were studied by TEM and the chemical composition was estimated with EDS (mapping and local) (Figure 3.1, Table 3.1). For all the samples, with a size around 20 nm, a pure Pd cubic core was visible. From this well-defined structure, the addition of Pt leads to the formation of a thin Pt-rich layer, confirmed by EDS, and the modification of the shape of the clusters. The layer was already visible after 0.6 h (Figure 3.1 and 3.2) with the formation of the shell on the corners of the Pd nanocubes to form a layer all over the core. For the particles with a synthesis time longer than 4 h, concavity appeared and increased, without significant change of the size. Homogeneous particles were prepared, excepted for the particles synthesized in 6 and 8 h, with octahedron-like agglomerates and core-shell flowers (Figure 3.2).

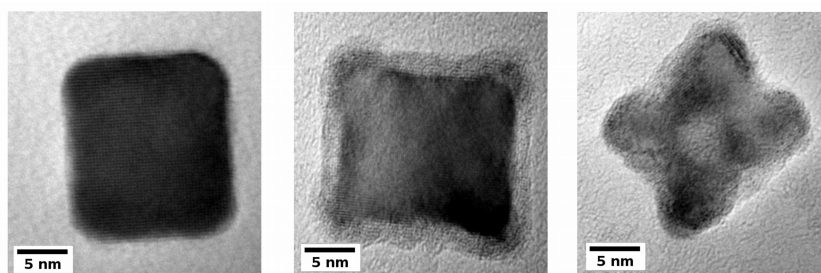


Figure 3.1 Principal steps for the evolution of the particles: Pd nanocubes (left), formation of a Pt thin shell in (particles prepared in 0.6 h, middle) and apparition of a concave structure (particles synthesized in 4 h, right).

The EDS measurements also revealed a local presence of bromide, in particular for the samples with a short time of synthesis, due to an incomplete galvanic replacement. The evolution of the chemical composition of the clusters was apparent (Table 3.1); the Pt:Pd ratio increased until 4 h of synthesis (35 wt % Pt) but decreased to 22 % and 9 % for the particles prepared in 6 and 8 h, respectively. Finally after 17 h, the PdPt clusters had a chemical composition equivalent to the PdPt nanoparticles fabricated in 4 h.

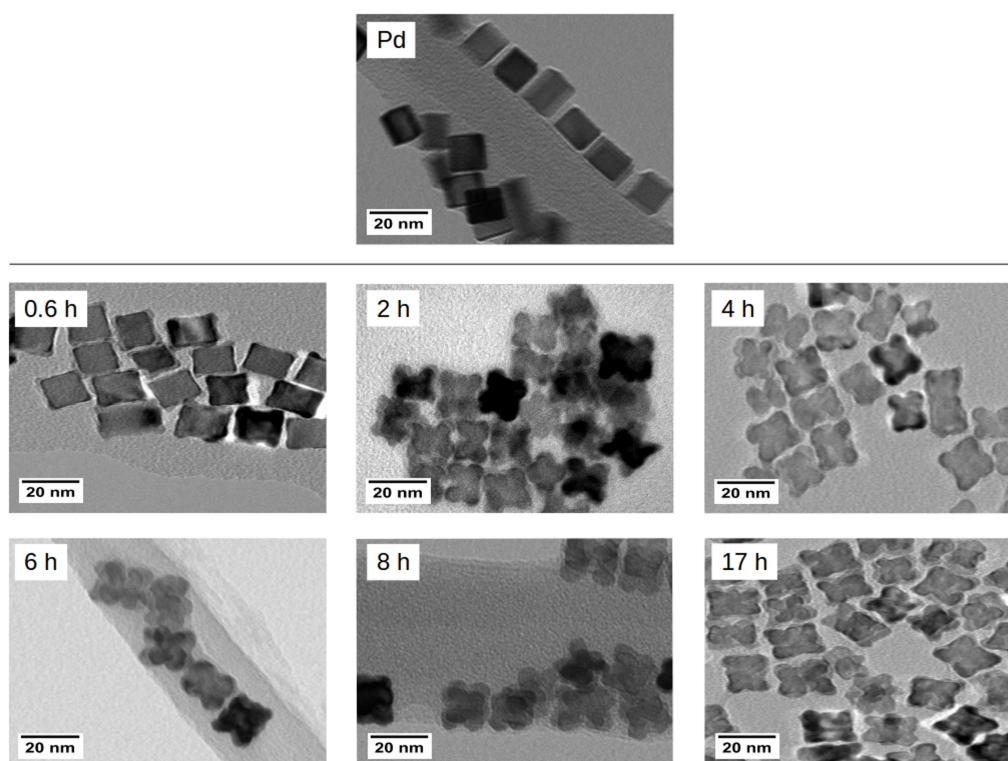


Figure 3.2 Evolution of the structure of the particles with the time of synthesis (TEM).

The crystalline structures of the particles followed with the X-ray diffraction spectroscopy

XRD measurements (from 30 to 90 °, 0.02 ° s⁻¹) allowed to determine the crystallographic structure of the particles and to calculate an estimation of the chemical composition. The face-centered cubic (*fcc*) structure was confirmed for all the particles, with the presence of the characteristic peaks corresponding to the planes (111), (200), (220), and (333) for the Pt and Pd crystals in the XRD spectra (Figure 3.3).

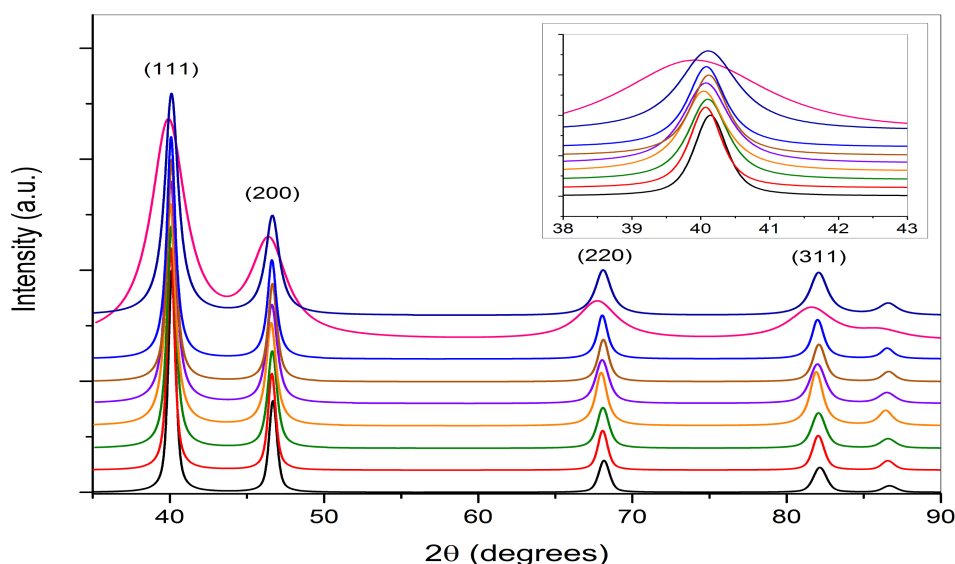


Figure 3.3 XRD spectra of the different catalyst (shift corrected and normalized). Insert: Magnification of the (111) peak. Pd nanocubes (black) and PdPt NPs: 0.6 h (red), 2 h (green), 4 h (orange), 6 h (violet), 8 h (brown), 17 h (blue); pure Pt (pink) and pure Pd (marine).

The form of the spectra revealed similarities for all the particles, expressing comparable bulk compositions. No peaks corresponding to Pt or Pd oxides were visible. After the normalization of the spectra, based on the intensity of the well-defined (111) peak, the interplanar distances d for all the particles were determined using Bragg's law:

$$2 \cdot d \cdot \sin(\theta) = n \cdot \lambda \quad (3.1)$$

where n is the integral factor, θ the Bragg's angle and λ the wavelength of the X-rays (Cu-K α_1 radiation, 1.54184 Å).

The size of the particles, S , was calculated from the widths of the (220) diffraction peaks using the Scherrer's equation, valid for the nanometer-scale:

$$S = \frac{K \cdot \lambda}{\beta \cdot \cos(\theta)} \quad (3.2)$$

K is the shape factor which is 0.94 here, regarding a *fcc* isotropic structure and β (radians) is the line broadening at half the maximum intensity (or full width at half maximum, FWHM).

To complete the analysis after the XRD measurements, an estimation of chemical composition of the different samples was realized according to Vegard's law, considering the system as a solid solution with a combination of two components, Pt and Pd, pure before their mixture, with the same crystalline structure (*fcc*) and at the same temperature.[88] It enables to obtain an approximation of the Pt:Pd ratio. Considering x the molar fraction of Pd,

$$a_{(Pt(1-x)Pd(x))} = (1-x) \cdot a_{Pt} + x \cdot a_{Pd} \quad (3.3)$$

The lattice parameters of the solid solution, the nanoparticles, $a_{(Pt.(1-x)Pd(x))}$ were measured by XRD and the lattice parameters of Pt a_{Pt} (3.923 Å) and Pd, a_{Pd} (3.891 Å) are theoretical values coming from the crystallographic open database (C.O.D).[89]

The analysis of the XRD spectra (Table 3.1) revealed changes for the structure and composition of the particles. The lattice parameters, 3.894 Å for the Pd and 3.913 Å for the Pt are close to the theoretical values, with deviations due to inhomogeneities in the crystals. For the particles, the lattice parameters and the inter-planar distances are between those of pure Pd and pure Pt. The lattice parameters and d-spacing values were larger for the Pt-rich particles, which is in accordance with the replacement of Pd atoms by Pt atoms, causing an expansion of the crystals. The different sizes of the particles, revealed by XRD, were comparable to the sizes estimated from the TEM images (with the software ImageJ). With an initial size of 19.2 nm for the Pd nanocubes and 20 nm for the PdPt nanoparticles synthesized in 0.6 h, the size decreased to 13.6 nm for the particles prepared in 6 h. For the longer synthesis times, the size increased again. The diminution of the size could lead to a faster dissolution of Pd and desorption of Br compared to the formation of the Pt shell until 6 h. After this, the increase of the size can be explained by a slowed or stopped dissolution of Pd, protected by the Pt deposited on the core. The chemical composition of the particles, determined by Vegard's law, varied following different steps.

Core-shell palladium-platinum nanoparticles synthesized
by galvanic replacement

The molar fraction of Pt increased in the particles, with 35 wt. % of Pt for the samples prepared in 4 h. Subsequently, while the XRD analysis showed a reduction of the quantity of Pt, with the molar fraction of Pt equal to 0.2 for the particles synthesized in 6 h and 0.1 for the particles prepared in 8 h, the EDS measurements indicated a constant quantity of Pt for both samples and the same Pt:Pd ratio for the catalysts prepared in 4 and 17 h.

Table 3.1 Summary of the results from the XRD measurements (error \approx 10%) and composition of the particles measured by EDS.

Sample	Lattice parameter (Å)	<i>d</i> -spacing (Å)	size (nm) (XRD)	Pd molar fraction (%) (XRD)	Pd molar fraction (%) (EDS)	size (nm) (TEM)	Pd weight (wt.%) (EDS)	Pt weight (wt. %) (EDS)
Pd nanocubes	3.891	2.2468	19.24	100	100	16.1	100	0
PdPt 0.6 h	3.892	2.2471	20.03	94	96	17.2	91	9
PdPt 2 h	3.894	2.2482	15.53	88	87	16.2	81	19
PdPt 4 h	3.900	2.2517	14.39	70	70	14.6	65	35
PdPt 6 h	3.897	2.2496	13.43	78	80	14.7	78	22
PdPt 8 h	3.893	2.2479	16.74	91	80	16.4	74	26
PdPt 17 h	3.896	2.2498	16.06	82	71	15.7	65	35

The deviation between the two experimental methods comes probably from the restrictive application of Vegard's law, already observed by researchers working on alloys, but also from chemical heterogeneities in the particles, which were not detected by EDS.[90, 91] The chemical composition and its evolution needs to be studied with high-precision instruments, like the mass-spectrometry (ICP-MS), to follow the changes in details.

Atomic study of the particles by extended X-rays absorption fine structure

The X-rays absorption fine structure, (XAFS) measurements represent a powerful technique to study the materials at the atomic scale. Based on the absorption of monochromatic X-rays by the atoms at energies near and above their core-level energy, important information about the physical and chemical properties of the material can be studied. The analysis of XAFS spectra provides the chemical state and the local atomic arrangement for the selected element and the surrounding atoms, with a high sensitivity to the oxidation state, the chemical and atomic coordination, and the inter-atomic distances. The XAFS spectra are divided in two parts: The X-rays near edge absorption fine structure (XANES) and the extended X-rays absorption fine structure (EXAFS). While the XANES region of the spectrum is more sensible to the oxidation state and the coordination chemistry of the absorbing atoms, the EXAFS region is better to learn more about inter-atomic distances, coordination number (CN), atomic arrangement and elements surrounding the absorbing atom. The configuration of the experimental system and the analysis of data are detailed in the article. Before data fitting, models with theoretical phase shifts and amplitude functions for the shell fit were developed with FEFF 8.2 based on pure Pt and Pd and PdPt metallic clusters with a *fcc* crystallographic structure.[92] After analysis and fitting of the EXAFS spectra at Pt-L_{III} edge, a comparison was possible between the pure Pt commercial and the different samples.

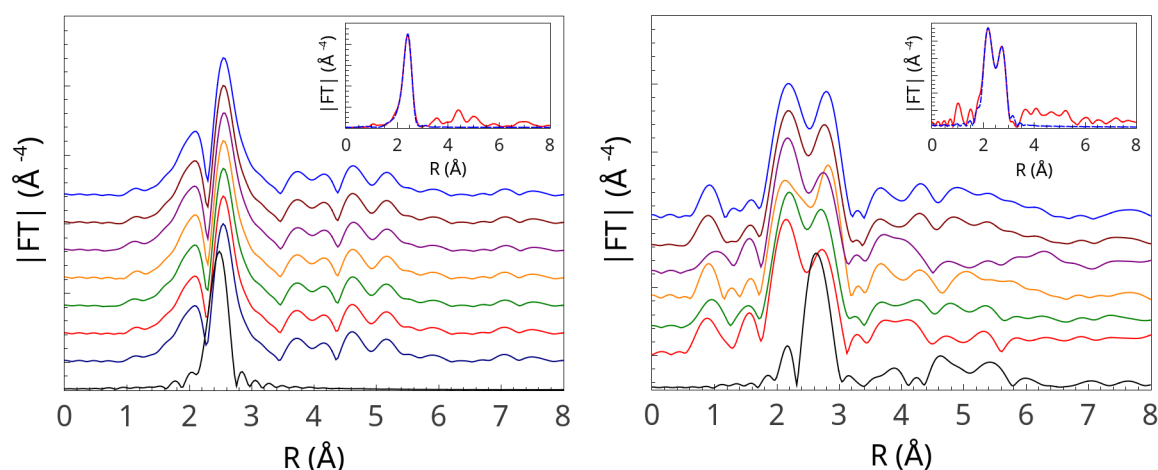


Figure 3.4 Fourier-transformed EXAFS spectra of the NPs at Pd-K (left) and Pt-L_{III} (right) edges. Pure Pt or Pd metal (black), Pd nanocubes (marine) and PtPd NPs: 0.6 h (red), 2 h (green), 4 h (orange), 6 h (violet), 8 h (brown), 17 h (blue). Insets: PtPd 2h NPs experimental (red line) and fitted (dotted blue line) Fourier- transformed EXAFS spectra (R range 1.7-3, k^3 weighted, $S_0^2 = 0.8$).

Core-shell palladium-platinum nanoparticles synthesized
by galvanic replacement

On the normalized and Fourier-transformed spectra, (Figure 3.4), at the Pd-K edge (left), the main peak at $R \approx 2.74 \text{ \AA}$ (Figure 3.4b) advocated the preponderance of one type of neighbors, expected to be Pd and confirmed by the shell-fill fit of the data (Table 3.2 and 3.3). At the Pt-L_{III} edge (right), a well-defined double peak was visible between 2 and 3 \AA for all the particles. The models confirmed that this double peak originates from the presence of both Pt and Pd neighbors in nearly equal proportions within the first shell. By contrast, only one peak was present in the spectra of the Pt commercial sample, as expected from the presence of only one type of neighbors. After analysis at Pt-L_{III}, the results demonstrated for all the particles a structure with Pt atoms surrounded by Pt and Pd atoms at distances of 2.72 to 2.74 \AA , in line with the crystallographic value of 2.74 \AA . [93]

Table 3.2 Coordination numbers (CN), interatomic distances R, Debye Waller factors (σ^2), and energy shifts (ΔE_0) at the Pt-L_{III} edge.

Sample	Pt-L _{III} edge						ΔE_0 [eV]	R_{factor}^2 res (%)
	Pt-Pt shell			Pt-Pd shell				
	CN	R (\AA)	σ^2 (\AA^2)	CN	R (\AA)	σ^2 (\AA^2)		
PdPt 0.6 h	6.7	2.72	0.0058	4.8	2.72	0.0058	5.9	5.4
PdPt 2 h	6.2	2.73	0.0057	5.1	2.73	0.0057	7.1	4.0
PdPt 4 h	8.7	2.75	0.0055	3.5	2.74	0.0055	8.3	2.3
PdPt 6 h	6.7	2.74	0.0061	4.8	2.74	0.0061	7.8	3.3
PdPt 8 h	7.3	2.74	0.0056	4.8	2.74	0.0056	7.7	2.2
PdPt 17 h	7.6	2.74	0.0056	4.3	2.74	0.0056	7.8	2.7

Based on the measurements realized at Pt-L_{III}, the small Debye-Waller factors indicated a small static and vibrational disorder. The sum of the coordination numbers (CN) for both Pt-Pt and Pt-Pd was close to 12, considering a relatively high error of 25 %, and the Pt:Pd ratio was close to 1. All these results, according to the analysis of the spectra at Pt-L_{III}, agreed with a *fcc* structure (also validated by XRD) composed of Pt and Pd with Pt atoms in a local environment, surrounded by Pt and Pd. Spectra at the Pd-K edge (Table 3.3) revealed a Pd-Pd distance of 2.74 \AA , as expected for a *fcc* structure. [61] The length of the Pt-Pd bond was slightly but significantly smaller than the length measured for the Pd-Pd pairs. Contrary to the values based on the measurements at Pt-L_{III}, the coordination numbers of the spectra at Pd-K edge

were between 9.5 to 11.2 and suggested that the Pd was mainly enclosed by Pd atoms and a smaller number of Pt atoms (CN between 0.6 and 1.8), with a statically insignificant variation among the different samples. The analysis of the EXAFS results suggested a well-structured Pd metallic core, where the majority of Pd atoms possess Pd neighbors surrounded by a thin Pt shell, where most of the Pt atoms have Pd neighbors. In accordance to TEM and EDS observations, the higher coordinations numbers for the Pt-Pt bond (Table 3.2) indicate an aggregation of Pt on the surface of the particles, with a small increase after 8 and 17 h of synthesis.

Table 3.3 Coordination numbers (CN), interatomic distances R, Debye Waller factors (σ^2), and energy shifts (ΔE_0) at the Pd-K edge.

Sample	Pd-K edge						ΔE_0 [eV]	R_{factor}^2 res (%)
	Pd-Pt shell			Pd-Pd shell				
	CN	R [Å]	σ^2 [Å ²]	CN	R [Å]	σ^2 [Å ²]		
PdPt 0.6 h	0.6	2.71	0.0051	11.2	2.74	0.0009	9.1	0.3
PdPt 2 h	1.4	2.71	0.0054	10.7	2.74	0.0054	5.4	1.6
PdPt 4 h	1.7	2.71	0.0053	10.5	2.74	0.0053	5.6	1.7
PdPt 6 h	1.7	2.72	0.0053	9.5	2.74	0.0056	8.7	4.2
PdPt 8 h	1.7	2.70	0.0053	10.2	2.74	0.0053	5.1	1.3
PdPt 17 h	1.8	2.71	0.0052	10.2	2.74	0.0052	5.3	1.5

3.3 Chemical properties and catalytic activity

Electrochemically active surface area and catalytic performances

As for the study of PdPt nanoflowers (Chapter 2), the electrochemically active surface area was calculated using the charge transfer during the adsorption/desorption of hydrogen on the surface of the catalyst, between 0.05 and 0.30 V. The charge transfer was calculated by integration of the experimental curves (Figure 3.5) and the resulting ECSA was based on a reference charge density of $2.4 \times 10^{-4} \text{ C cm}^{-2}$ for Pd and $2.1 \times 10^{-4} \text{ C cm}^{-2}$ for Pt for the oxidation of a monolayer of hydrogen.

Core-shell palladium-platinum nanoparticles synthesized by galvanic replacement

The geometric area, $A_{\text{geometric}}$, geometric area of the working electrode (0.1963 cm^2), was compared to the chemical active area, A_{real} , by introduction of the roughness factor, r_f (Eq 4.4)[66]:

$$r_f = \frac{A_{\text{real}}}{A_{\text{geometric}}} \text{ with } A_{\text{real}} = \frac{Q_H}{2.1 \times 10^{-4}} \quad (3.4)$$

The determination of the ECSA was based on measurements with three samples per particle batch and the total error was estimated higher than 10 %, including the experimental (reference electrode, potential shift and homogeneity of the deposition), the chemical (reference charge density) and the mathematical errors (integration of the curves).

All the values (Table 3.4) are in the same range as in the literature for PdPt nanoparticles coated on carbon.[86] In the experimental curves (Figure 3.5), three regions could be distinguished: Between 0.05 and 0.30 V, the chemical adsorption (from 0.05 to 0.075 V) and the desorption of hydrogen (until 0.30 V) was apparent.

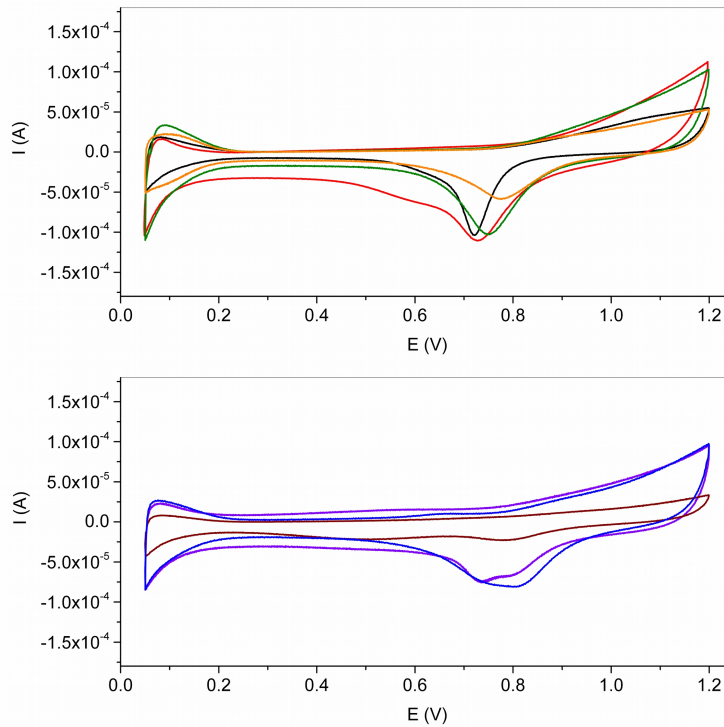


Figure 3.5 Voltammograms used for the determination of the ECSA: Pure Pd (black), PdPt NPs: 0.6 h (red), 2 h (green), 4 h (orange), 6 h (violet), 8 h (brown), 17 h (blue).

Afterward, the charging process of the double layer (0.30 to 0.65 V) was followed by the adsorption of hydroxide anions and oxygen on the catalyst as well as their reduction. The particles prepared in 4 h possessed the best ECSA ($100.6 \text{ m}^2 \text{ g}^{-1}$), higher than for the commercial Pt sample ($84.04 \text{ m}^2 \text{ g}^{-1}$) while the ECSA of the particles synthesized in 2 h was almost the same. A significant increase of the ECSA occurred for the PdPt core-shell NPs 0.6 h compared to the Pd nanocubes (Figure 3.6). Higher values of ECSA were observed for the particles with a concave shape and a thin layer of Pt on the surface (TEM images, Figure 3.1 and Figure 3.2). For the particles synthesized in 6 and 8 h, the ECSA decreased with values smaller than for the pure Pd nanocubes. The formation of agglomerates for these particles may contribute to the reduction of their chemical activity.

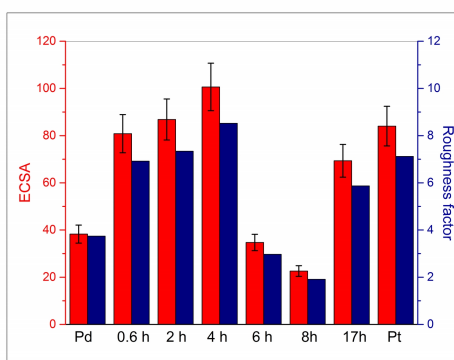


Figure 3.6 ECSA (red) with error (black) and roughness factor (blue) for the different particles.

The particles synthesized in 17 h showed an ECSA ($69.3 \text{ m}^2 \text{ g}^{-1}$) similar to the particles prepared in 0.6 and 2 h (80.8 and $86.6 \text{ m}^2 \text{ g}^{-1}$ respectively). Different factors explain the higher ECSA (Table 3.4) for the PdPt core-shell NPs (except for the particles synthesized in 6 and 8 h) compared to the pure Pd nanocubes. With the galvanic replacement, the formation of a thin layer of Pt or Pd-Pt alloy on a Pd core improved the chemical activity. The thickness of the shell is a main parameter for the catalytic activity of the core-shell nanoparticles.[94, 95] The shape and the electronic structure of the core have also an influence on the catalytic performance. Depending of the time of synthesis, major changes in the shape and the structure of the particles appear, with variation of the thickness of the Pt-rich shell and development of concave structures. During the galvanic replacement, with the deposition of Pt by replacement of Br atoms and the formation of a Pt and/or Pd-Pt alloy shell, the crystallographic and the atomic structure were modified as it was confirmed by XRD and EXAFS, leading to additional chemical active sites, which may contribute to a higher ECSA (Table 3.4).[96] Additionally, the ratio Pt:Pd has a high influence on the chemical activity of the particles.[97–99]

The catalytic activity

As for the study about PdPt nanodendrites (Chapter 2), the catalytic activity of the particles was determined in function of the mass of catalyst, applying the Koutecký-Levich equation. After the measurements, the voltammograms could be divided in three different regions (Figure 3.7). Until 0.60 V, the reaction on the surface of the electrode was controlled by chemical diffusion processes (the mass transport). From 0.60 to 0.85 V, the increasing potential induced diffusion and kinetic processes, with adsorption/desorption of the oxygen and hydroxide radical on the surface of the electrode as well as with a possible formation of H_2O_2 . Up to 0.85 V, the main processes were pure kinetic phenomena. In the voltammograms, the onset of the ORR, 0.75 V for the pure Pd nanocubes, increased gradually to 0.87 V for the PdPt nanoparticles and the commercial Pt catalyst.

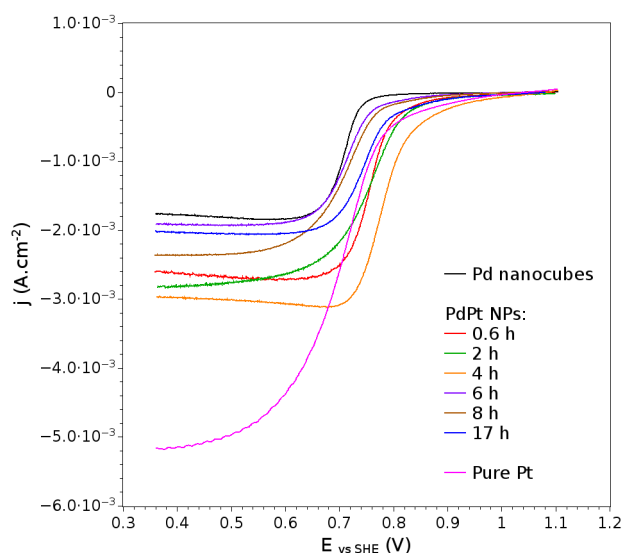


Figure 3.7 Characteristic voltammograms for the ORR of NPs and pure Pt coated on carbon in O_2 saturated $HClO_4$ aqueous solution (1.2 to 0.4 V, 5 mV s^{-1} , 1600 rpm)..

The rotation of the working electrode (1600 rpm) during the experiments guaranteed a fast transport of the chemical active species by convection. The catalytic activity was reported to the mass of catalyst and so defined as mass activity. A clear evolution of the mass activity for the different samples was observed (Table 3.4). The Pd nanocubes showed the lowest mass activity (4.8 A g^{-1}), confirming the importance of Pt to increase the performance of the catalysts.[100, 101] The addition of a second metal, with the modification of the electronic structure and a presence of more chemically active sites, improved the catalytic activity.[102, 103]

3.3 Chemical properties and catalytic activity

The mass activity of the PdPt clusters prepared in 0.6 h (17.6 A g^{-1}) was twice as high as the pure Pd and close to the commercial Pt catalyst (17.9 A g^{-1}). From 0.6 h to 4 h, the particles featured mass activities superior to the commercial Pt (24.7 A g^{-1} after 2 h and 33.4 A g^{-1} after 4 h).

Table 3.4 Evolution of the catalytic properties of the particles for the oxygen reduction reaction.

Sample	ECSA ($\text{m}^2 \text{ g}^{-1}$)	Roughness factor	n (e^-) exchanged	ORR (0.85 V) A g^{-1}		
				Fresh	Degraded	Change
Pd pure	33.3	3.7	1.95	4.8	4.7	2 %
PdPt 0.6 h	80.8	7.9	2.57	17.6	15.1	14 %
PdPt 2 h	86.8	8.4	1.58	24.7	19.1	22 %
PdPt 4 h	100.6	8.5	1.93	33.4	32.7	2 %
PdPt 6 h	34.7	3.4	1.45	6.7	5.5	18 %
PdPt 8 h	22.6	2.2	1.25	8.1	9	2 %
PdPt 17 h	69.3	6.7	1.78	16.8	16.5	2 %
commercial Pt	84.0	7.1	4.06	17.9	15.4	14 %

The galvanic replacement created more chemically active sites with the removal of Br atoms, replaced by Pt atoms and the formation of one thin Pt/PdPt alloy into the shell. The most promising particles were prepared in 4 h with a Pd molar fraction of 0.7.[104–106] The Pt:Pd ratio also influences the electronic structure of the shell of the particles, with an easier adsorption/desorption of the oxygen atoms at the surface of the particles and a reduced amount of H_2O_2 produced during the ORR for the particles with a higher Pt content (Chapter 1). In accordance with the ECSA, the mass activity of the particles synthesized in 6 and 8 hours was small, in the range of the pure Pd nanocubes. For the particles prepared in 17 h, the catalytic properties were better (17.9 A g^{-1}), close to pure commercial Pt catalyst. An evident correlation existed between the catalytic properties (ORR) and the chemical active sites (ECSA), confirming the mass activity of the particles was not only controlled by the Pt content but also by the shape, the structure (thickness of the shell), and the crystallographic properties of the particles.

Stability of the catalysts

For an application in fuel cells, stability of the particles is required, without degradation of their catalytic activity after a long time of use. The stability of the particles was tested by measurements of their electrochemical properties after 2000 CV (from 0.05 to 1.20 V). The comparison of the catalytic performance (Table 3.4) revealed different stabilities. Considering the experimental error ($\approx 10\%$), the mass activity for the pure Pd and the PdPt core-shell nanoparticles synthesized in 4, 8 and 17 h was stable. The remaining samples, prepared in 0.6 h (14%), 2 h (22%), 6 h (18%) and also the commercial Pt (14%) showed a decreasing of their catalytic performance. The number of electron exchanged during the ORR is also reduced after the stability test, confirming the reduction of the catalytic performances. The stability is strongly affected by the chemical composition and the structure of the particles. The main process leading to a degradation of the particles with a core-shell structure is the depletion of the atoms from the core to the shell of the cluster, with the formation of a thicker shell and a modification of the chemical composition. In combination to this process, a redeposition and aggregation of the metallic atoms on the surface of the particles is possible. Moreover, the formation of hollow nanoparticles by degradation of the core-shell structure and dissolution of Pt and Pd atoms can occur. For the particles studied here, the particles with a molar fraction of Pd of 0.7 were the most stable and revealed a high chemical activity.

Kinetic of the reaction with the catalyst

The oxygen reduction reaction in an acid environment is a multi-electronic process, divided in elementary steps, with different chemical intermediates with an associative mechanism or a dissociative one (Chapter 1 and 2).[7, 107]

The dissociative mechanism represents the break of the O-O bond by adsorption of O_2 molecules on chemically active site (M) in the surface of the catalysts and the formation of oxides (Pt or Pd oxide) (3.5). The reaction of the oxide with a proton and one electron creates a hydroxide (3.6) and the Pt (or Pd)-OH bond dissociates leading to the formation of water (3.7).



The associative mechanism includes the oxygen reduction via the formation of peroxide intermediates:



The formation of H_2O_2 is also possible in step (3.11) via the desorption of HO from the surface. The presence of hydrogen peroxide as a stable compound in the acidic solution indicates an incomplete electron transfer.

The kinetic of the ORR was studied assuming the presence of a rate determining step (RDS), controlling the global chemical reaction which can be the initial step or a heterogeneous electron transfer. Depending on the potential, rapid changes occur at the surface of the electrode, with adsorption/desorption of chemical intermediates, formation and dissolution of oxides etc.. At high potentials ($E > 0.8 \text{ V}$), the surface of the catalyst is a mixture of Pt and Pt oxide, whereas at low potentials, a free oxide surface is awaited. By Levich and Tafel analysis, the RDS of the reaction can be studied. The number of exchanged electrons (n) during the ORR can be estimated by the value of the diffusion current (or Levich current, i_L) measured at 0.5 V for different rotational speeds of the RDE (100, 400, 900, 1600, 2500 rpm). The Levich equation represents the relation between the Levich current, the rotational speed (ω , rad s^{-1}) and the number of electrons (n):

$$i_L = 0.602 \cdot n \cdot F \cdot A \cdot C_0 \cdot D^{\frac{2}{3}} \cdot \nu^{-\frac{1}{6}} \cdot \omega^{\frac{1}{2}} \quad (3.13)$$

where F is the Faraday constant (96485 C mol^{-1}), A the geometric area of the electrode (0.196 cm^2), C_0 the concentration of the molecular oxygen in saturated solution, ($1.26 \times 10^{-6} \text{ mol cm}^{-3}$), D the diffusion coefficient of the oxygen in the solution ($1.67 \times 10^{-5} \text{ mol cm}^{-2}$), ν the kinetic viscosity of the electrolyte ($1.009 \times 10^{-2} \text{ cm}^2 \text{ s}^{-1}$). The Levich current is proportional to the square roots of the rotational speed of the RDE and so, n can be determined by the slope of the linear plot of $i_L^{-1} = f(\omega^{\frac{1}{2}})$ in a Levich diagram (Figure 3.8).[12, 108]

Core-shell palladium-platinum nanoparticles synthesized by galvanic replacement

For all the samples, the number of electrons exchanged was close to 2 for the PdPt nanoparticles and close to 4 for the pure Pt (Table 3.4). The exchange of two electrons revealed the formation of H_2O_2 during the reaction, reducing the catalytic activity. The presence of bromide at the surface of the nanoparticles is poisoning the ORR, with a diminution of the number of chemical active sites (ECSA) and the catalytic properties of the clusters.

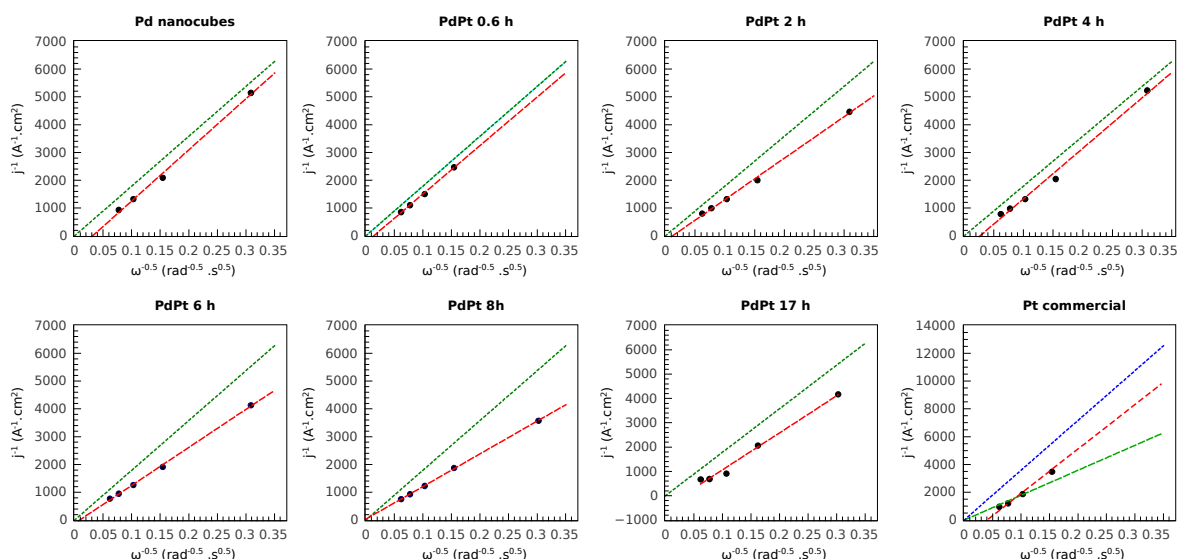


Figure 3.8 Levich diagrams for the different samples. Intensity measured at 0.4 V at different rotational speeds (black points), and red lines linearization following the Koutecky Levich equation. The green lines correspond to an exchange of two electrons and the blue lines to a transfer of 4 electrons during the ORR.

With the Tafel analysis, the exchange current density of the ORR (j_0) was estimated using the simplified Tafel equation (Chapter 1):

$$E = a + b \cdot \log |j| \quad (3.14)$$

Extrapolating the Tafel line to the value of the potential of the equilibrium for the ORR provides the value of the exchange current density.

Table 3.5 Evolution of the kinetic parameters determined by Tafel analysis.

Tafel analysis			
Sample	1 st Tafel slope (V dec ⁻¹)	2 nd Tafel slope (V dec ⁻¹)	j_0 (10 ⁻⁷ A cm ⁻²)
Fresh samples			
PdPt 0.6 h	0.058	0.110	4.35
PdPt 2 h	0.073	0.154	42.6
PdPt 4 h	0.058	0.122	31.6
PdPt 6 h	0.053	0.104	0.2
PdPt 8 h	0.053	0.106	0.4
PdPt 17 h	0.057	0.134	18.6
commercial Pt	0.052	0.133	4.9
Degraded samples			
PdPt 0.6 h	0.053	0.109	0.8
PdPt 2 h	0.060	0.148	13.2
PdPt 4 h	0.054	0.131	17.4
PdPt 6 h	0.050	0.096	0.2
PdPt 8 h	0.053	0.107	0.4
PdPt 17 h	0.061	0.127	6.3
commercial Pt	0.054	0.105	1.3

Previous theoretical and experimental studies established two different Tafel lines for the ORR on Pt and PdPt catalysts in acid conditions: Around 0.120 V dec⁻¹ at higher overpotential and 0.06 V dec⁻¹ at low overpotential.[105, 109, 110] The received Tafel plots of the particles revealed two pseudo-linear regions (Figure 3.9), namely between 0.75 and 0.9 V, with slopes between 0.052 and 0.073 V dec⁻¹, for the low current densities and between 0.104 and 0.154 V dec⁻¹ at high current densities, in line with literature data.[64, 111]

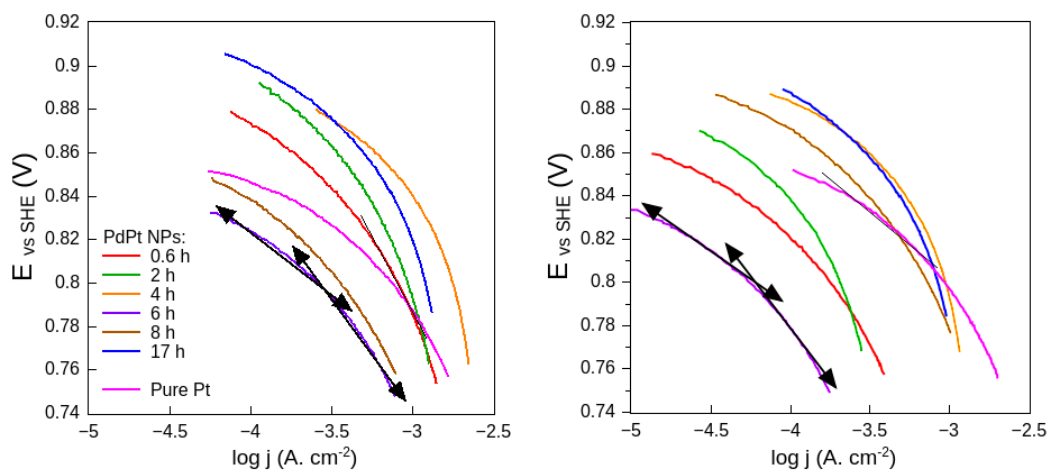


Figure 3.9 Tafel plots before (left) and after (right) stability test for commercial Pt and PdPt nanoparticles (NPs).

The Tafel slope close to 0.06 V dec^{-1} is attributed to a pseudo two electrons process on the surface covered by Pt and Pt oxide (Equation 3.8 or 3.11) while the higher Tafel slope indicates a first electron transfer as RDS on a pure Pt surface.[111, 112] The concurring values of the exchange current density and the catalytic activity was not totally verified, with a higher current density for the particles prepared in 17 h compared to the particles synthesized in 6 h and the commercial Pt with higher catalytic activity. The same phenomena is visible for the particles prepared in 2 h with an higher exchange current density than the PtPd 4 h NPs. After the stability test, the exchange current density decreased for the majority of the sample, indicating a slower reaction and degraded catalytic properties.

3.4 Studies via impedance spectroscopy

The electrochemical impedance spectroscopy (EIS) was done under a constant polarization, at 0.5 V, with the RDE at 1600 rpm in aqueous HClO_4 saturated with oxygen to guarantee negligible migration phenomena and a constant oxygen concentration at the surface of the electrode.[82] At this potential, the dominant chemical processes are related to the mass transport. The spectra were analyzed assuming no space between the support, the particles and the Nafion layer. The Nyquist diagrams revealed the typical shape of diffusion phenomena (Figure 3.10).

They can be separated in two areas at the frequency ω_D : at high frequencies (left part of the diagram), a straight line with an angle close to 45° is present for all the samples while two different cases appear at lower frequencies: the particles synthesized in 6 and 8 h show a degenerated arc whereas a quasi-vertical line emerges for the other samples.

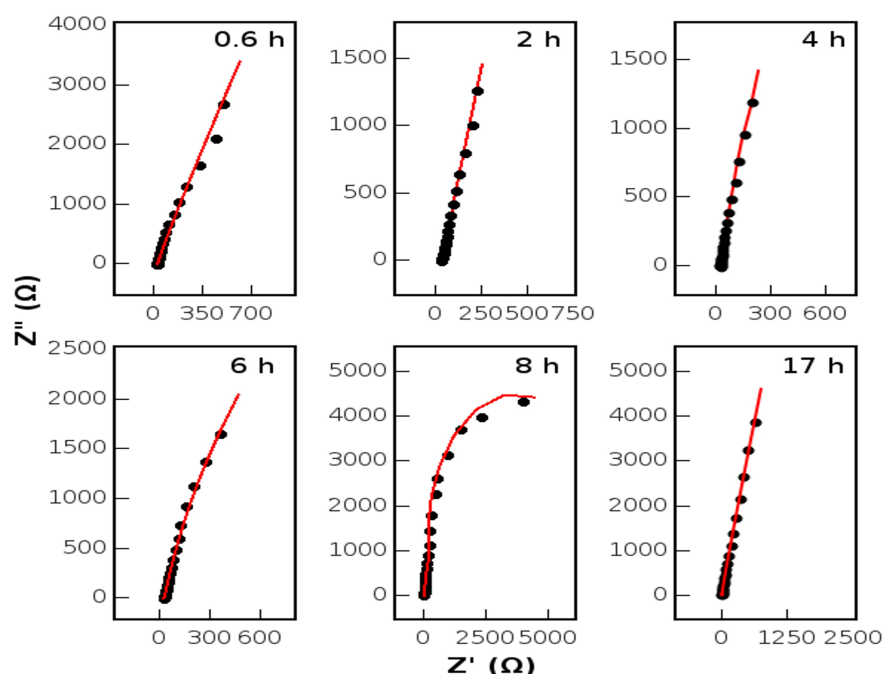


Figure 3.10 Experimental (black dots) and fitted (red lines) Nyquist diagrams.

These diagrams fit to the theoretical diagrams of the Randles circuit (Chapter 2, Figure 2.5) and can be interpreted as finite diffusion with transmissive or reflective boundaries. An inductor, L , was added to the classical Randles circuit (Figure 3.11) to represent the experimental noise (cable connection, instabilities in frequencies and potential, external electromagnetic noise, etc..).

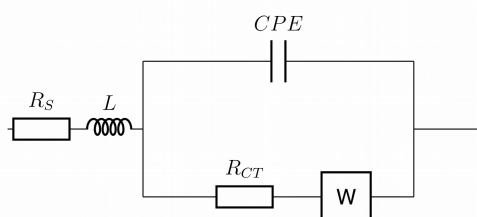


Figure 3.11 Electric schema of the Randles equivalent circuit.

Core-shell palladium-platinum nanoparticles synthesized
by galvanic replacement

With this electrical circuit, the fitting of the curves was done to determine the values of the components and to compare the different samples.

The total impedance of the system, combination of the individual impedances of the electrical components present in the equivalent circuit is defined as:

$$Z_{TOTAL} = Z_{R_s} + Z_L + Z_{(CPE,R_{CT},W)} \quad (3.15)$$

with the impedance of the resistors Z_{R_s} for the resistance of the electrolyte and $Z_{R_{CT}}$ for the charge-transfer resistance, the inductor $Z_L = j\omega L$ (with the inductance L), and the CPE, $Z_{CPE} = \frac{1}{Q(j\omega)^n}$ (with $0 \leq n \leq 1$).

The impedance of the Warburg element, Z_W can be described by:

$$Z_W = \sqrt{\frac{R_D}{j\omega\tau}} \cdot \tanh\left(\sqrt{j\omega\tau}\right) \text{ for a transmitting diffusion} \quad (3.16)$$

and

$$Z_W = \sqrt{\frac{R_D}{j\omega\tau}} \cdot \coth\left(\sqrt{j\omega\tau}\right) \text{ for a reflective diffusion} \quad (3.17)$$

R_D is the diffusion resistance, D is the diffusion coefficient, ω is the radial frequency ($\omega = 2\pi f$), τ the time constant for the diffusion layer of thickness L and diffusion coefficient D ($\tau = \frac{L^2}{D}$).

After fitting, small differences appeared among the samples (Table 3.6). The values for the resistances of the electrolyte ($\approx 30 \Omega$) and the charge transfer (between 0.2 and 1 Ω) confirmed an easy migration of the charges for all the samples. With a dimensionless factor (n) close to 1, the CPE was considered as capacitor, with a capacitance Q, indicating an accumulation of charges at the interface electrode/electrolyte.[113] The capacitance, influenced by different parameters, varied from 4×10^{-6} (PdPt 4 h) to 1.4×10^{-3} (pure commercial Pt). According to these values, a restricted ionic and charge accumulation was present at the interface, in particular for the PdPt NPs prepared in 4 and 6 h.

The finite diffusion with transmitting boundary observed in the Nyquist diagrams for the particles synthesized in 6 and 8 h (Figure 3.11) may indicate a low adsorption of chemical active species in the diffusion layer and at the surface of the particles, confirming the low catalytic performance of these samples. The high Warburg diffusion resistance, reflecting a slower diffusion of the charged species for the particles prepared in 8 h, also validate the low catalytic activity.

For the other samples, the reflective diffusion apparent in the Nyquist diagrams, can be attributed to the adsorption of the chemically active species on the particles and explain the better catalytic properties but without clear relation between these values and the catalytic performance of the particles.

Table 3.6 Characteristics of the equivalent circuit after fitting of the impedance spectra for the different NPs.

Sample	R_s (Ω)	R_{CT} (Ω)	L (H) $\times 10^{-5}$	Q (F) $\times 10^{-4}$	n	R_w (Ω)	τ (s) $\times 10^{-3}$	W_N	L (μm)
commercial Pt	24.6	0.16	1.4	13.9	0.85	17.9	37.8	0.47	7.95
Pt-Pd 0.6 h	30.3	1.01	1.6	1.13	0.94	11.4	7.6	0.47	3.56
Pt-Pd 2 h	30.5	0.78	1.6	5.60	0.84	49.6	42.1	0.47	8.38
Pt-Pd 4 h	28.0	0.53	1.7	0.04	0.90	11.3	12.7	0.47	4.61
Pt-Pd 6 h	23.7	0.48	1.4	0.30	0.80	14.2	13.7	0.46	4.78
Pt-Pd 8 h	34.8	0.88	1.9	3.86	0.94	73.8	10.2	0.47	4.13
Pt-Pd 17 h	31.4	0.52	1.7	1.88	0.93	18.7	4.9	0.48	2.86

Furthermore, the thickness and the time constant of the diffusion layer were determined to characterize the catalyst. For the ORR, the diffusion constant can be assigned to the different chemical steps of the reaction (adsorption of O_2 , dissociation of the O-O bond, reduction), depending on the applied potential. The inverse of the diffusion time constant, τ^{-1} , can be associated with the desorption rate constant of the different chemical intermediates of the ORR.

At 0.5 V, the particles synthesized in 17 h possess the highest desorption rate, followed by the particles synthesized in 0.6, 8, 4, 6 h, the pure commercial Pt and the particles prepared in 2 h. These last two samples had also a thick diffusion layer. The values obtained by analysis of the EIS spectra using the Randles circuit as equivalent circuit, especially the small Warburg diffusion and charge transfer resistances, indicated nanostructured PdPt particles with a high number of chemically active sites with a composition improving the charge transfer and the mass transport. However, the comparison of the results for the different samples revealed no clear relations among the catalytic activity, the physico-chemical properties, and the values of the electrical components of the equivalent circuit. New EIS measurements with a higher frequency range and an electromagnetic protection may support the characterization.

3.5 Conclusion

The core-shell Pt-Pd nanoparticles prepared by galvanic replacement with different times of synthesis revealed an evolution of their structure, size, and physico-chemical properties. A clear relation between the properties of the particles and their catalytic performances, with an evolution with the time of synthesis, appeared. The TEM experiments allowed the monitoring of the evolution of the size and the structure of the particles, from pure cubic nanocubes to core-shell cubic concave PdPt nanoparticles. A variation of the chemical composition, with an increasing concentration of Pt from the PdPt NPs prepared in 0.6 h to the NPs synthesized in 4 h (Pt molar fraction 0.3), and a subsequent decrease until 8 h, followed by a final raise for the particles synthesized in 17 h was observed. Nevertheless, complementary experiments are required: A high-precision quantification of the Pt and Pd forming the particles by ICP-MS could help to investigate the influence of the chemical composition. The formation of a Pd-Pt alloy present in the shell of the particles with modification of the structure of the particles was revealed by EXAFS and XRD measurements. XPS spectroscopy, as a surface sensitive and semi-quantitative technique would be useful to finish the characterization of the particles. The electrochemically active surface area and the oxygen reduction reaction, were studied by CV and LSV to compare the catalytic performances as well as the stability of the particles. As expected, the addition of Pt, with variation of the molar fraction and the formation of a Pd-Pt alloy in the shell of the particles clearly influence the catalytic performances and the stability of the particles. After 0.6 h of synthesis, PdPt particles, mainly constituted of Pd (95% Pd, 5% Pt) with catalytic activity and stability close to the pure Pt powder were produced. With longer synthesis times, the catalytic activities of the particles improved and were superior to the pure Pt, with the best performances after 4 h of synthesis. These stable particles present a catalytic activity two times higher than pure Pt, with a lower amount of the expensive Pt metal (Pt molar fraction of 0.7).

Chapter 4

Characterization and comparison of the particles via *in-situ* XAFS

Part of this chapter have been published in: S. Tymen, A. C. Scheinost, C. Friebe and U. S. Schubert, *Adv. Nanoparticles*, **2017**, 6, 75-91. DOI: 10.4236/anp.2017.62007.

After the synthesis, the characterization via XRD, TEM, EXAFS and the determination of the catalytic activity of the different particles as already described in Chapter 3, complementary studies were realized to follow the oxygen reduction reaction for different particles and to explain the catalytic performances. The particles with three different times of synthesis were studied: Particles with a high Pd molar fraction (0.95) prepared in 0.6 h, and particles with less palladium prepared in 2 h (Pd molar fraction 0.87) and 8 h (Pd molar fraction of 0.8). The aim was to follow the evolution of the surface of the particles, with the formation and dissolution of oxides at the different steps of the oxygen reduction reaction through the observation of the Pt-Pd and Pt-O bonds. The use of *in-situ* XAFS allowed the investigation of the surface of the particles and the evolution when the characteristic potentials of the ORR are applied between the electrodes (Figure 4.2).[114–116] The analysis of XANES and EXAFS spectra measured at the Pt-L_{III}-edge in fluorescence mode enabled to investigate the transformations occurring at the surface of the particles.

However, to separate the species present in the system and compare the particles via their spectra and catalytic properties at different potentials (Figure 4.2), the iterative transformation factor analysis (ITFA) was used to analyze the results.[117]

4.1 Structure of nanoparticles after different times of synthesis

The evolution of the structure, previously studied by TEM (Chapter 3), indicated a progressive transformation of the shape of the PdPt nanoparticles with the time of synthesis. For the particles prepared in 0.6 h, the TEM observations revealed a cubic shape and the formation of a very thin layer covering the core of the cubes with clearer edges visible in the TEM images (Figure 4.1).

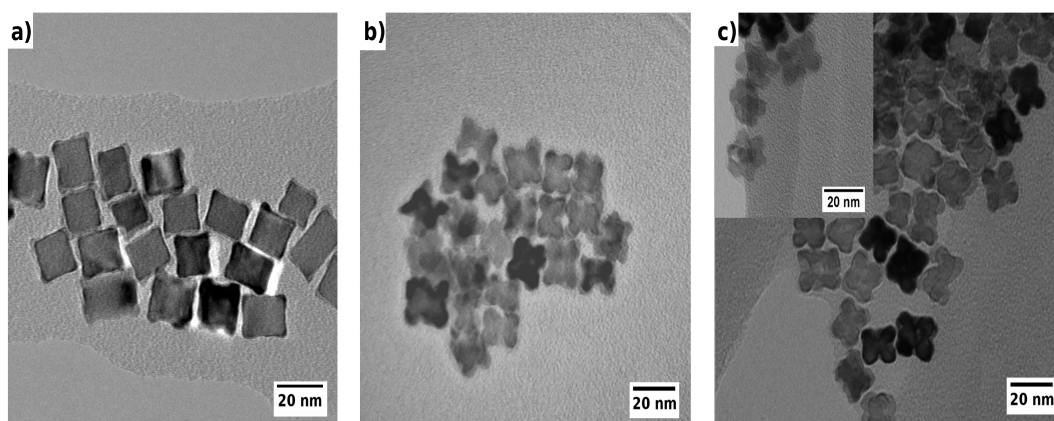


Figure 4.1 TEM images revealing the evolution of the particles with the time of synthesis: a) 0.6 h, b) 2 h and c) 8 h.

The composition of the particles, with a core of Pd and a shell mainly constituted of Pt, was validated by EDS. The measurements revealed particles mainly composed of Pd with an augmentation of the Pt content from 9 to 26 % in with the increasing time of synthesis (Table 4.1). After 2 h, the development of concave particles was accompanied with a higher content of Pt, reducing the contrast between the core and the thicker shell. For the longest time of synthesis, 8 h, the particles were richer in Pt, without significant evolution of the shape, similar to the clusters prepared in 2 h. Nevertheless, additional larger particles, with a cubic dark core covered by a lighter layer were observed.

Table 4.1 Evolution of the amount of Pt and Pd in function of the time of synthesis (measured by EDS).

Sample	Pt (wt.%)	Pd (wt. %)	Pt/Pd error (%)
0.6 h	8.6	91.4	9.9/2.8
2 h	19.1	81.0	5.9/8.3
8 h	26.4	73.6	8.1/7.6

4.2 EXAFS measurements

For all the particles, the *ex-situ* EXAFS measurements were realized under the same experimental conditions as the EXAFS studies in Chapter 3. The particles coated on carbon powder and stabilized by BN were characterized at the Pt-L_{II} and Pd-K edges. The *in-situ* experiments were realized in a home-made electrochemical cell filled with aqueous HClO₄ ($1 \times 10^{-1} \text{ mol L}^{-1}$) with a Pt wire as counter electrode and a Ag/AgCl reference electrode. The *in-situ* measurements were performed at different key potentials for the ORR: 0.65 and 0.85 V to follow the oxidation, 1.20 V the vertex point, 1.00, 0.85 and 0.35 V the re-reduction (Figure 4.2).

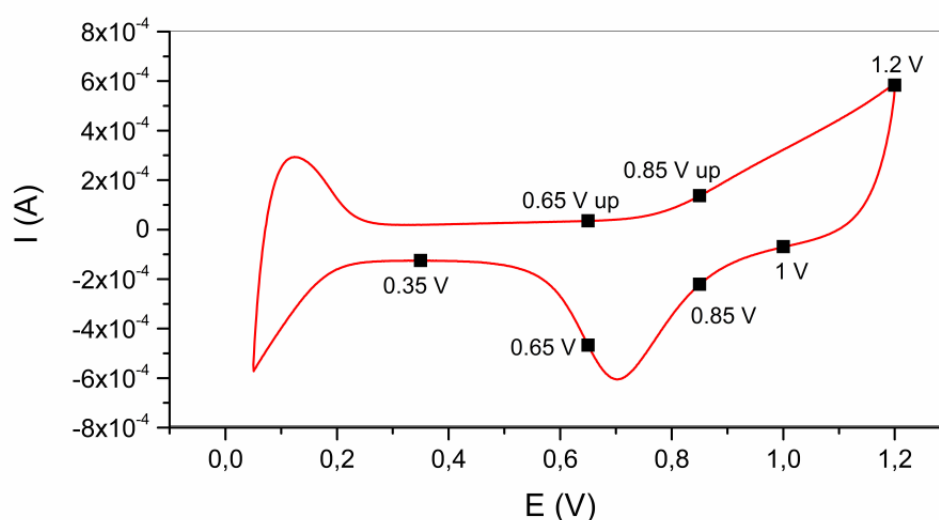


Figure 4.2 Cyclic Voltammogram of the ORR and the different potentials used for the EXAFS *in-situ* measurements.

The analysis of the EXAFS spectra at Pt-L_{III} (Table 4.2) allowed to gain information about the Pt-Pt and Pd-Pt bonds in the particles, while the spectra taken at the Pd-K edge provided details about the Pt-Pd and Pd-Pd bonds (Table 4.3).

Table 4.2 Coordination numbers (CN), interatomic distances (R), Debye Waller factors (σ^2), and energy shifts (ΔE_0) at the Pt-L_{III} edge.

Pt-L _{III} edge								
Sample	Pt-Pt shell			Pt-Pd shell			ΔE_0 (eV)	R_{factor}^2
	CN	R (Å)	σ^2 (Å ²)	CN	R (Å)	σ^2 (Å ²)		
0.6 h	6.7	2.72	0.0058	4.8	2.72	0.0058	5.9	5.4
2 h	6.2	2.73	0.0057	5.1	2.73	0.0057	7.1	4.0
8 h	7.3	2.74	0.0056	4.8	2.74	0.0056	7.7	2.2

Using different processes (already described in Chapter 3), Fourier-transformed EXAFS spectra were obtained and used to investigate and to compare the different particles. With an equal distance between the Pt atoms and their neighbors (of 2.72 to 2.74 Å) in line with the crystallographic data, a Pt:Pd ratio close to 1, and a sum of the coordination numbers (CN) close to 12 (with an estimation of a 25 % error), a structure with Pt atoms surrounded by Pt and Pd atoms was apparent.[89]

Table 4.3 Coordination numbers (CN), interatomic distances R, Debye Waller factors (σ^2), and energy shifts (ΔE_0) at the Pd-K edge.

Pd-K edge								
Sample	Pd-Pt shell			Pd-Pd shell			ΔE_0 (eV)	R_{factor}^2
	CN	R (Å)	σ^2 (Å ²)	CN	R (Å)	σ^2 (Å ²)		
0.6 h	0.6	2.71	0.0051	11.2	2.74	0.0009	9.1	0.3
2 h	1.4	2.71	0.0054	10.7	2.74	0.0054	5.4	1.6
8 h	1.7	2.70	0.0053	10.2	2.74	0.0053	5.1	1.3

This information combined to the small Debye-Waller factors, indicating a small static and vibrational disorder, confirmed PdPt core-shell nanoparticles with a shell possessing a *fcc* structure constituted by Pt atoms that are surrounded by Pt and Pd atoms.

In contrast to the Pt atoms, the high coordination numbers of the Pd-Pd bonds, between 10.2 and 11.2, indicate the predominance of Pd atoms surrounded by other Pd atoms with a minor presence of Pt atoms (CN between 0.6 and 1.7). Finally, the combination of the results of the EXAFS spectra at the Pd-K and Pt-L_{III} edges revealed the structure of the particles as a well-structured metallic core, where most of the Pd atoms have Pd neighbors, covered by a thin shell of Pt atoms where the majority of Pt atoms still possesses Pd neighbors.

4.3 *In-situ* measurements

The dependence of the chemical processes of the ORR on the potential creates changes at the surface of the electrode, with creation and degradation of oxides, inducing a modification of the structure of the catalysts.[118] The Pt-L_{III} XAFS measurements at different potentials (cf Figure 4.2), allowed the characterization of the particles providing information about the Pt-Pt and Pt-Pd chemical bonds and the monitoring of the creation or degradation of oxides at the surface of the catalyst by comparison with standard EXAFS spectra. The iterative transformation factor analysis, with Varimax and iterative target test (ITT), was employed to study the evolution of the XAFS spectra with the potential. The analysis was performed on normalized k^3 -weighted spectra after dead-time correction (Chapter 3) using a program developed by A. Rossberg, A. C. Scheinost *et al.*[119, 120] The first step of the ITFA, the Principal Component Analysis (PCA) aims to identify the number of independent components required to reconstruct the experimental spectrum and does not require any structural model.[121] To achieve this purpose, the eigenvectors (equivalent to abstract spectra) and the factor loadings (abstract concentrations of the components) have to be set to represent the data in a n-dimensional space factors with an orthogonal basis formed by the eigenvectors. The eigenvectors and factor loadings are abstract objects not physically interpretable. The PCA works with the theoretical root mean square functions: Real error (RE), embedded error (IE), and semi-empirical indicator functions (IND) developed by Malinowski.[122] For each sample, with measurements at seven different potentials (cf Figure 4.2), the PCA started with a factor loading of seven, the maximum number of components to reconstruct the experimental spectra. Subsequently, the reduction of the dimensional factors was performed by PCA using the program: After the elimination of factors corresponding to the noise and the experimental error, the number of dimensional factor was reduced and differences between the spectra (reconstructed and the experimental) corresponding to the different components appeared.

After the analysis of the EXAFS spectra, a final dimensional factor of two was revealed: Two main spectra, corresponding to the two different components, were sufficient to reconstruct the experimental spectrum of a sample. In a second step, comparing the standard EXAFS spectra with the *in-situ* XAFS and theoretical spectra of different structures (composed of Pt, Pd, and Pt oxide; modeled with FEFF 8.2), the two components were assigned to a component based on a Pt-O bond and to a component based on a Pt-Pt or Pt-Pd bond (these two bonds possess quasi-similar values).[123]

Table 4.4 Coordination numbers (CN), interatomic distances (R), Debye-Waller factors (σ^2) and energy shift ΔE_0 from the Pt-L_{III}-edge spectra at 0.35 V determined by curve fitting.

Sample	Pt-Pt shell			Pt-Pd shell			ΔE_0 (eV)	R_{factor}^2 res (%)
	CN	R (Å)	σ^2 (Å ²)	CN	R (Å)	σ^2 (Å ²)		
0.6 h	6.9 Pt-Pt	2.70	0.0021	5.1 Pt-Pd	2.70	0.0030	5.0	1.4
2 h	7.4 Pt-Pt	2.72	0.0019	4.6 Pt-Pd	2.71	0.0022	6.4	2.3
8 h	7.6 Pt-Pt	2.72	0.0015	4.4 Pt-Pd	2.71	0.0030	6.3	2.1
Commercial Pt	12 Pt-Pt	2.74	0.0080				7.2	4.6

Applying the IFTA, the experimental spectra were reconstructed by a linear combination of the two components using a FEFF model, with a higher weight for the first component, suggesting a combination of Pt-O and Pt-Pd bonds within the samples. The experimental spectra of the particles prepared in 8 h could be reconstructed with one component and a negligible amount of the second one, which is assigned to the Pt-O bond. The small residuals after the fitting of the experimental spectra confirmed the FEFF model was appropriate for the analysis. The values were similar to *ex-situ* EXAFS spectra, and the small Debye-Waller factors confirmed a well-organized structure (Table 4.2 and 4.4). For both *ex-situ* and *in-situ* EXAFS at 0.35 V spectra, the peak corresponding to the Pt-O bond ($R \approx 1.8 \text{ \AA}$) was not visible and the spectra could be fitted only with Pt-Pt and Pt-Pd metallic bonds in cluster with a *fcc* crystalline structure. Therefore, the oxide was not present when the applied potential is 0.35 V.

4.4 Evolution of the structure in function of the potential

After the PCA analysis revealed the experimental EXAFS spectra can be reconstructed by a combination of two components, the evolution of the structure of the particles at different potentials was investigated (Figure 4.3).

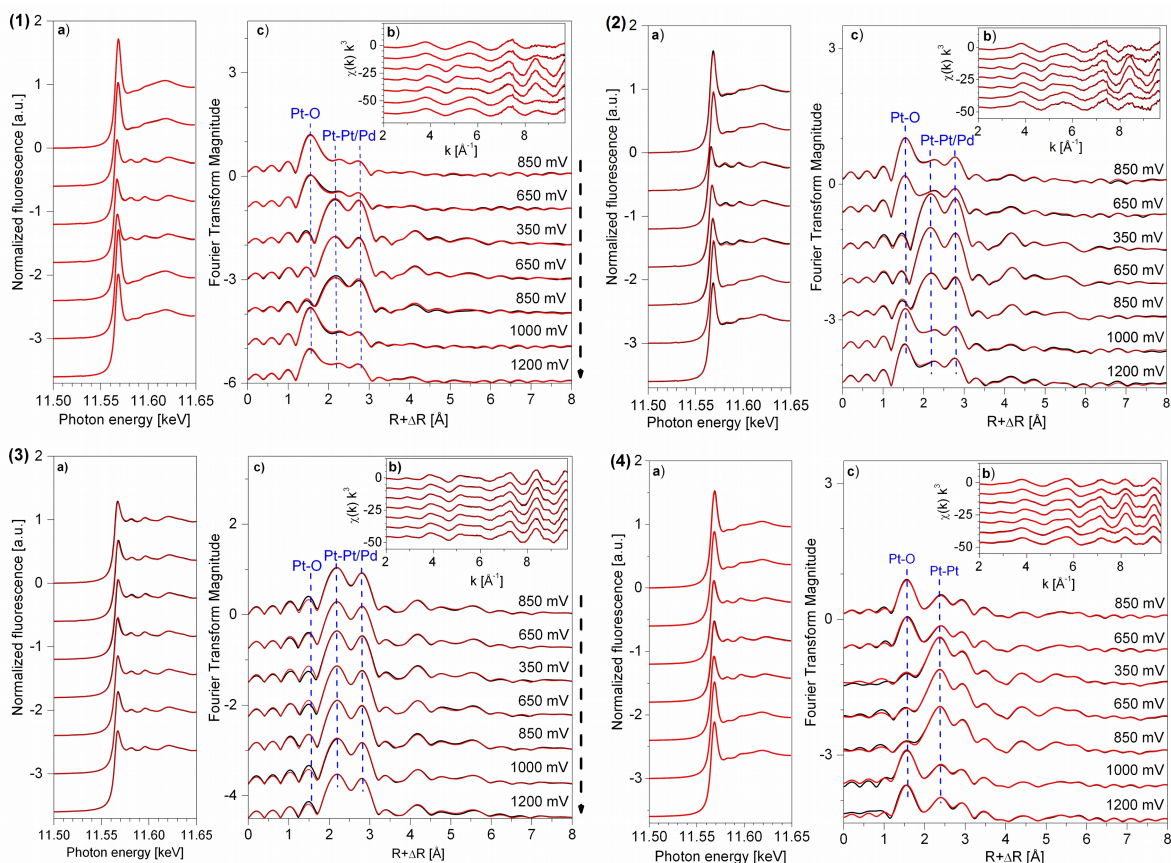


Figure 4.3 Experimental (red) and reconstructed (black) XANES (left), EXAFS (insert) and Fourier-transformed EXAFS spectra for the nanoparticles: (1) 0.6 h, (2) 2 h, (3) 8 h and (4) the commercial Pt.

With the FEFF-based model including a Pt-oxide cluster, a characteristic peak at $\approx 2 \text{ \AA}$, corresponding to the theoretical length of the Pt-O bond was visible. For all the samples (except for the particles synthesized in 8 h), a peak appeared and disappeared at $\approx 1.8 \text{ \AA}$ on the Fourier-transformed EXAFS spectra at different potentials while the opposite phenomena occurred for the double peak between 2 and 3 \AA , which was attributed to the Pt-Pt and Pt-Pd bonds (only Pt-Pt for the commercial Pt). When the potential decreased, from 0.85 to 0.35 V, the peak at $\approx 1.8 \text{ \AA}$ vanished while it reappeared when the potential attained 0.85 V again.

With this results and the Pt oxide model based on the FEFF and EXAFS database, this peak was attributed to the Pt-O bond. It permitted the proposition of the formation of a thin layer of Pt oxide, with the adsorption of oxygen atoms at the surface of the particles at potentials higher than 0.85 V, confirmed by a clear peak at 1.0 and 1.2 V, except for the particles prepared in 8 h. These results were validated by analysis of the experimental spectra made with a FEFF model based on Pt-Pt, Pt-Pd and Pt-O clusters (Table 4.5).

 Table 4.5 Structural parameters of the particles and the commercial Pt (Pt_{com}) at 1 V, Pt_{II}-edge.

Sample	Pt-Pt shell			Pt-O shell			Pt-Pd shell			ΔE_0 (eV)	R_{factor}^2 res (%)
	CN	R (Å)	σ^2 (Å ²)	CN	R (Å)	σ^2 (Å ²)	CN	R (Å)	σ^2 (Å ²)		
Pt_{com} path 1	6 Pt-Pt	2.74	0.0091	0 Pt-O	0.00	0.0000	0.0	0.00	0.0000	9.49	5.43
Pt_{com} path 2	7 Pt-Pt	3.08	0.0275	2.2 Pt-O	1.99	0.0046	0.0	0.00	0.0000	9.49	5.43
0.6 h	7.4 Pt-Pt	2.66	0.0129	3.6 Pt-O	1.98	0.0065	1.7 Pd-Pt	2.70	0.0065	6.26	4.43
2 h	9.7 Pt-Pt	2.69	0.0178	2.4 Pt-O	1.99	0.0022	2.7 Pd-Pt	2.75	0.0092	6.64	3.76
8 h	7.6 Pt-Pt	2.74	0.0040	0.0 Pt-O	0.00	0.0000	4.0 Pd-Pt	2.74	0.0041	6.92	0.23

For the commercial Pt catalyst, two Pt-Pt bonds were assumed: One for the pure Pt nanoparticles and the second one for the Pt particles containing Pt oxide. At 1.00 V like at 0.35 V, the small Debye-Waller factors of the EXAFS spectra indicated well-structured particles. The increasing of the factors value at 1.00 V for the Pt-Pt shell (except for the particles synthesized in 8 h) can be explained by the presence of oxide, inducing disorder for the structure of the shell. Taking in account the experimental error, the lengths of the Pt-Pd and Pt-Pt bonds are in line with the theoretical values (2.807 Å) and to the values found by analysis of the EXAFS spectra at 0.35 V. A slight asymmetry is visible in the Fourier-transformed EXAFS spectra for the particles prepared in 0.6 and 2 h, with a higher peak height at 2.2 Å at small potential, decreasing progressively when the potential increases. This was also observed by other researchers working on PdPt nanoparticles.[124]

With no significant changes and a possible reproduction with one component for the particles synthesized in 8 h, the formation of an oxide layer is not plausible for these particles.

4.5 The relative concentrations and their changes followed by the ITFA

The last step of the ITFA procedure was the determination of the relative concentrations of the components and their evolution with the potential. This was done considering a system based on two components (assigned to the metal and the oxide), using the Varimax and the ITT methods.[117, 125] The Varimax method permitted to identify the spectra with the highest or lowest amount of a component, and, via the ITT, the relative concentrations of the components were calculated. They were normalized using the data of the commercial Pt sample, assuming the presence of a unique metallic component, with a surface composed of pure Pt metal at 0.35 V and fully covered with oxide when the applied potential is 1.00 V, as reported in literature.[3, 107, 110]

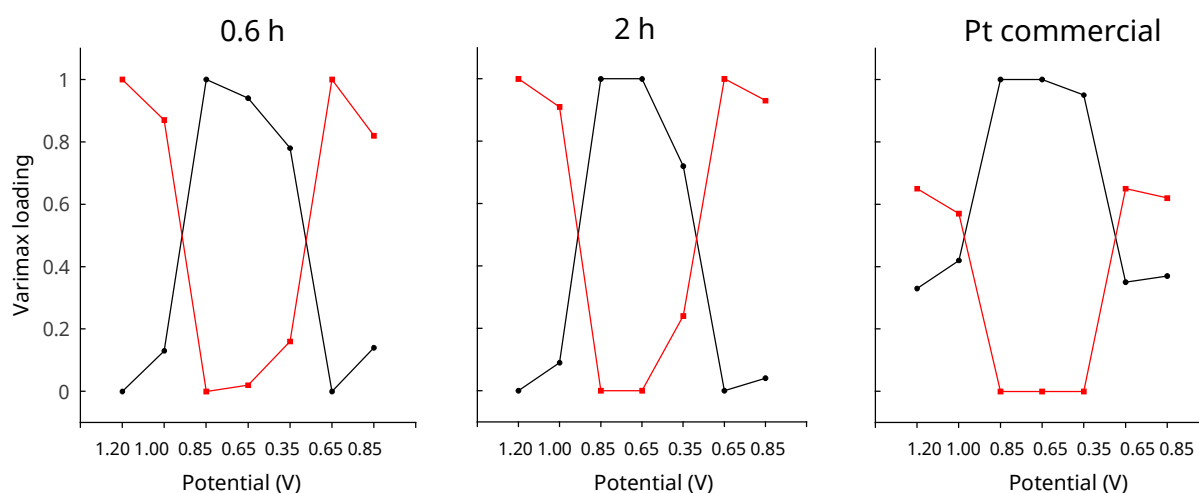


Figure 4.4 Evolution of the relative concentrations of metal (black) and oxide (red) with the potential.

As apparent in the curves (Figure 4.4), the concentration of metal increased when the potential decreased. The reverse phenomenon was visible for the oxide with a quasi symmetry for the relative concentrations. This confirmed the previous results of Nagamatsu *et al.*[124]

Transformation of the particles with the potential and ORR

Two main mechanisms are suggested for the ORR: An associative and a dissociative one as presented in Chapter 3.[3, 7, 107]

In case of the associative mechanism, the O-O bond is not broken before the adsorption at the surface of the particle. After the adsorption and when the potential increases, the different steps of the reaction are the same for both mechanisms. The results of the *in-situ* measurements demonstrated the presence of Pt-O bonds for the potentials higher than 0.85 V. Up to 1.00 V, according to the ITFA analysis, the relative concentration of the oxide was close to 1 when it was 0 for the metal. This could be due to an increasing of the quantity of oxide and a high degree of oxidation for potentials up to 1.00 V.[126]

The last steps of both mechanisms (Chapter 3, equations 3.2, 3.3, 3.7 and 3.8) are equal and, at higher potentials, both mechanisms can occur. As already stated, above 0.85 V the XAFS *in-situ* measurements suggested the presence of Pt-O bonds. Up to 1.00 V, the amount of oxide increased, accompanied by a high degree of surface oxidation [126], the relative concentration of the oxide determined using the Varimax method for our experimental data analysis was close to 1 while it is 0 for the metal.

4.6 Catalytic performances of the particles

As already described in Chapter 3, the catalytic performances of the particles are different, depending on the time of synthesis, as well as on their shape, structure, and chemical composition. After the measurement and calculation of the activity of the particles (Table 4.6), the different mass activities were similar to reported values in literature.[72, 127] The particles synthesized in 2 h were the best for the ORR with a mass activity higher than the commercial Pt. The performances of the particles prepared in 0.6 h were close to the pure Pt, while for the particles made in 8 h, the electrochemical measurements revealed a low catalytic activity (Chapter 3). This was confirmed by *in-situ* XAFS measurements, where no significant changes and no Pt-O bonds were visible in the spectra when the potential increased. Without Pt-O bonds, there was no adsorbed of the oxygen (or not detected) at the surface of the particles causing a really bad oxygen reduction reaction.

Table 4.6 Catalytic activity for the different samples.

Sample	0.6 h	2 h	8 h	Commercial Pt
Mass activity (A g ⁻¹)	17.4	25.9	8.8	18.7

As previously discussed in Chapter 3, the mass activity is highly influenced by the morphology and the chemical composition of the particles. The composition of the PdPt alloy composing the shell of the particles and the cubic shape may explain the high chemically active surface and catalytic performances of the particles. The influence of the composition of the alloy on the catalytic performances of the particles was already described by other researchers.[12, 109]

4.7 Conclusion

The investigation of the evolution of the structure of the of core-shell PdPt nanoparticles depending of the applied potential was realized by *in-situ* XAFS measurements and the results were compared to their catalytic activity. The application of different potentials, related to the different steps of the ORR, revealed differences in the XAFS spectra. The analysis of the experimental data was carried out by the ITFA. After the first step of the analysis, the PCA, two main components, Pt or PdPt in metallic and in oxide form were indicated, allowing to reproduce the experimental spectra. In a second step, applying the Varimax method and the ITT, the evolution of the relative concentrations of the two components, metal and oxide, was monitored. The oxide appeared for the potential higher than 0.65 V and was the main form at 1.00 V. The relative concentration of the metallic species increased with the decreasing of potential and was predominant at 0.35 V. The structural parameters of the particles (CN, σ^2 , R), were determined by analysis of the experimental curves using WinXAS software and models with PdPt and α -PtO developed through the FEFF code. After analysis of the data, an accordance of the results with the ITFA was visible. New *in-situ* measurements to characterize all the particles synthesized by galvanic replacement (Chapter 3) at Pt-L_{III} and Pd-K edge would be useful to have more information about the formation of oxide (Pt and Pd oxide) during the ORR. After the measurement of the catalytic activity, new characterization of the particles by XPS and ICP-MS could help to link the structure and the chemical composition of the particles to their catalytic performances.

Abstract

The high price of platinum currently employed as catalyst for the oxygen reduction reaction in fuel cells represents an obstacle for a widespread usage of these cells. The development of bimetallic particles, reducing the quantity of platinum is a promising solution to increase the viability of the cells and to reduce their price. In this doctoral thesis, palladium was used as a second metal to synthesize bimetallic particles with easy methods. The role of bromide on the properties and performances of the palladium-platinum clusters with a nanoflowers structure was investigated (Chapter 2) and the effect of the time of synthesis on particles prepared by galvanic replacement was analyzed (Chapters 3 and 4). In the end, the formation/dissolution of oxide at the surface of core-shell palladium-platinum nanoparticles was examined (Chapter 4).

First of all, the particles were prepared with or without bromide, using a one step method or via a two steps method with bromide. Different structure and shape were revealed: Without bromide, rough cubic-like shape clusters with a size of 30 nm were formed. With the addition of bromide, larger particles (60 nm) appeared. The particles synthesized in two steps possessed a more spherical shape and a dense corona of platinum became visible. All these particles are composed of a palladium rich core and a surface constituted by interconnected platinum grains, with an higher density of platinum for the 45 nm clusters. After measuring the electrochemical surface area (inferior to pure platinum nanoparticles) and the mass activity, no apparent influence of the size was detected. The chemical composition, in particular the density of platinum at the surface of the catalysts and the curvature of the particles were important regarding their performances. The particles synthesized in two steps (45 nm) revealed the best catalytic activity and stability. These catalytic properties, combined with a high current exchange density for these clusters, suggested the formation of a palladium-platinum alloy at the surface of the particles. The alloying enhances the adsorption and dissociation of O_2 at the surface of the catalyst and conduct to better performances.

Additionally, the impedance study demonstrated that the 45 nm nanoparticles have the shortest diffusion length and the highest reaction rate. For all the particles, a low resistance for the charge transfer indicated an easy transport of the reactant to the chemically active sites, in particular for the 45 nm nanoparticles. All these results confirmed the influence of the curvature and the chemical composition on the catalytic properties of the particles. The alloying effect

was also verified with the highest performance for the 45 nm clusters, with a platinum rich surface and a compact porous structure.

Beside nanoflowers, core-shell nanoparticles were synthesized using the galvanic replacement method and the influence of the time of synthesis studied. From pure palladium nanocubes to core-shell palladium-platinum nanoparticles, an evolution of the physico-chemical properties of the particles got visible. Different times of synthesis were used: 0.6 h, 2 h, 4 h, 6 h, 8 h and 17h. A formation of a platinum-rich shell and concave nanoparticles appeared with the increasing times of synthesis. Until 4 h, the molar fraction of platinum and the size of the particles increased, while after 6 and 8 h it decreased. Finally, after 17 h, the size and the platinum molar fraction of the particles were similar to the particles synthesized in 4 h. An evolution of the *fcc* structure of the particle was visible with the variation of the platinum molar fraction. The EXAFS measurements confirmed well-structured particles with a shell composed of a platinum rich alloy. The electronic effect induced by the formation of the platinum-palladium alloy enhanced the catalytic performances, as well as the stability of the particles. For the clusters prepared in 6 and 8 h, with a lower quantity of platinum, a reduction of the catalytic activity was observed. The impedance measurements confirmed the accessibility of the reactants to the chemical active sites. The transmissive diffusion profile revealed by this measurements for the particles synthesized in 6 and 8 h is in accordance with their low catalytic performances. All these results confirmed that the galvanic replacement is a viable method to synthesize high performances low platinum content core-shell nanoparticles.

Furthermore, the formation/dissolution of oxide at the surface of the catalyst during the oxygen reaction was studied using *in-situ* XAFS measurements. Three platinum-palladium core-shell nanoparticles synthesized in 0.6 h, 2 h and 6 h were used and seven characteristic potentials of the oxygen reduction reaction were applied. The EXAFS spectra were analyzed to characterize the particles and the IFTA allowed the comparison of the particles at different potentials. A two components FEFF model, based on palladium-platinum in metallic form and the related oxide, was created. The reconstruction of the experimental spectra with this model permitted to follow the evolution of the formation/dissolution of oxide at the surface of the particles. The presence of oxide was also visible on the EXAFS experimental spectra with the apparition of a peak at $\approx 2 \text{ \AA}$, theoretically attributed to the Pt-O bond. Afterward, the change of the relative concentrations of the two components, metal and oxide was monitored. Their evolution was in accordance with literature reports, with an increasing concentration of oxide with an increasing potential and, an increasing concentration of metal when the potential decrease.

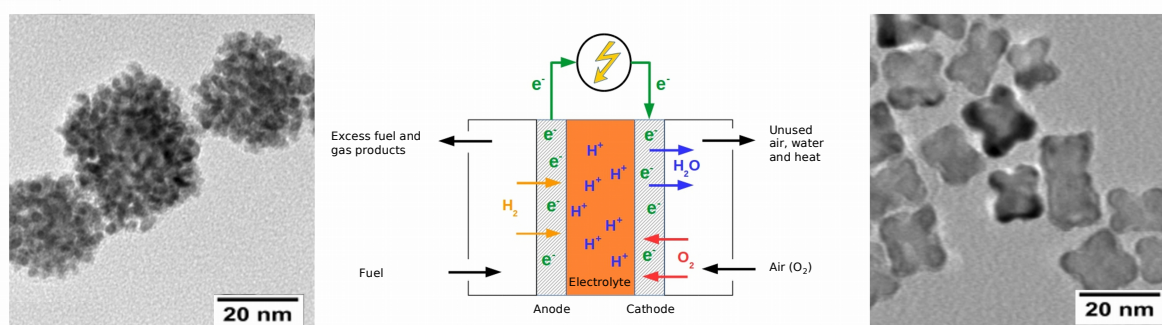


Figure 5.1: Bimetallic catalysts for the ORR: PdPt nanoflowers (left), PEM fuel cell, PdPt core-shell nanoparticles.

To conclude, palladium-platinum bimetallic nanoparticles with high catalytic performances were synthesized. The simple method used to prepare the clusters and the reduction of the quantity of platinum represent an advantage for a possible application as efficient and less expensive catalysts. Further experiments and utilization in a real fuel cell will be useful to measure the performance of these materials in real conditions (Figure 5.1). The coating of the catalyst on structured carbon (nanocubes) could also enhance the oxygen reduction reaction. A new project aiming the replacement of palladium by a cheaper metal (iron, nickel or copper) with catalytic properties with the established methods, could also contribute to the development of new material with a potential application in fuel cells.

Zusammenfassung

Die hohen Kosten des Platins, das als Katalysatormaterial für die Sauerstoffreduktionsreaktion (ORR) in den gegenwärtigen PEM-Brennstoffzellen verwendet wird, stellen ein Hindernis für deren breiten Einsatz dar. Bimetallische Nanopartikel sind hierbei eine vielversprechende Alternative, um die Wirksamkeit der Zellen zu verbessern und ihren Preis zu senken. Im Rahmen dieser Promotion wurde Palladium, als zweites Metall neben Platin, für die Katalysatorsynthese verwendet. Dabei wurde der Einfluss von Bromid auf die Form der synthetisierten Palladium-Platin-Nanoteilchen untersucht (Kapitel 2). Zudem wurde die erforderliche Zeit für die Synthese der Partikel erforscht, die über das Verfahren des galvanischen Austausches hergestellt wurden (Kapiteln 3 und 4). Des Weiteren wurden *in-situ*-XAFS Messungen durchgeführt (Kapitel 4), um die Bildung und Zersetzung der Oxide auf der Oberfläche der Partikel mit sich änderndem angelegtem Potential zu studieren.

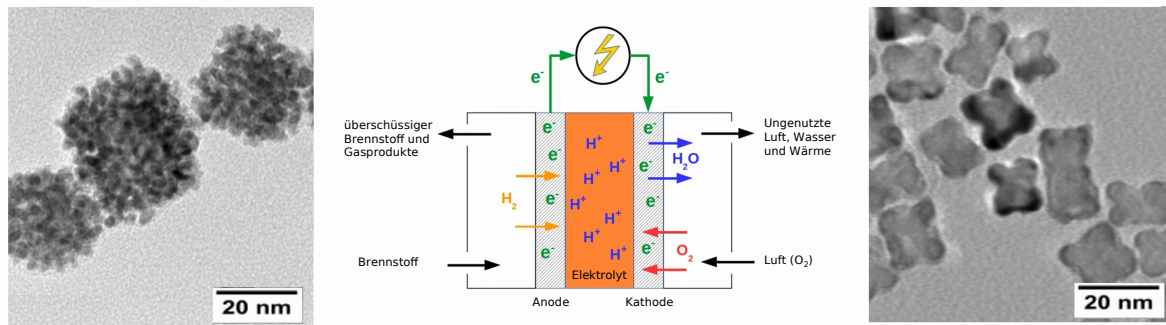
Im ersten Teil der Promotion wurden Partikel mit und ohne Kaliumbromid, welches die Form der Teilchen beeinflusst, hergestellt. Namentlich wurden verschiedene Partikeltypen durch eine Ein-Schritt-Methode mit und ohne Bromid, sowie durch eine Zweischnitt-Synthese mit Bromid hergestellt. Ohne Bromid bildeten sich raue Partikel mit einer quasi-kubischen Struktur und einer Größe von 30 nm aus. Durch Zugabe von Bromid entstanden größere Partikel (60 nm) mit einer größeren, platinreicheren Oberfläche. Diese Partikelform war sphärischer als der Partikel von einer Größe von 30 nm und wies eine kompakte "Korona" auf. Mit Ausnahme der Größe (etwa 45 nm) zeigten die in zwei Schritten mit Bromid hergestellten Partikeln keine signifikanten Unterschiede in der chemischen Zusammensetzung. Alle Partikel hatten eine an Platin reiche Oberfläche, insbesondere jene mit einer Größe von 45 nm. Die durch CV bestimmte ECSA war für alle Partikel niedriger, verglichen mit kommerziellen Pt/C-Katalysatoren. Jedoch wurde eine höhere Katalysatoraktivität festgestellt. Die chemische Zusammensetzung und die Krümmung der Oberfläche im Vergleich zu kommerziellen Katalysatoren war ähnlich. Die in zwei Schritten synthetisierten Partikel besaßen die größte katalytische Aktivität und Stabilität. In Kombination mit dem hohen Wert der Austauschstromdichte lässt dies auf eine mögliche Platin-Palladium-Metallegierung schließen. Diese verbessert die Adsorption/Desorption des Sauerstoffs an der Oberfläche des Katalysators und damit die katalytische Aktivität für die ORR. Impedanzexperimente zeigten außerdem, dass diese Partikel die kürzesten effektivsten Diffusionswege und die größten Reaktionsratenkonstanten aufwiesen. Niedrige und stabile

Widerstandswerte zeigten einen einfachen und schnellen Ladungstransfer und Transport der Reaktanten auf die chemisch aktiveren Stellen. Dies gilt insbesondere für die 45 nm Cluster. Die mögliche Platin-Palladium-Metalllegierung auf der Oberfläche der Partikel könnte die hohe Stabilität der Cluster erklären.

In Kapitel 3 wurde der Einfluss der Syntheszeit auf die physikalischen und chemischen Eigenschaften der platin- und palladiumhaltigen Partikel studiert. Nach der Präparation von reinen Palladiumkuben wurden Partikel mit Palladiumkern und Platinschale durch die Zugabe von Platinsalzen in die Lösung der Palladiumcluster hergestellt. Dabei wurden unterschiedliche Reaktionszeiten angewendet, um so die Entwicklung der Partikel bezüglich ihrer Struktur und chemischen Eigenschaften verfolgen zu können. Mit steigender Synthesedauer findet eine Entwicklung von Palladiumwürfeln zu konkav-kubischen Nanopartikel mit Palladiumkern und Platinschale statt, wobei längere Präparationszeiten zu konkaveren Partikeln mit dickeren Platinschalen um dem Palladiumkern führten. Zeiten von 0.6 bis 4 h resultierten in einen steigenden Platinanteil. Für Partikel, die in 6 und 8 h hergestellt wurden, sank der Platinanteil wieder. Die Cluster mit einer Syntheszeit von 17 h hatten den selben Platingehalt wie die Partikel mit einer Syntheszeit von 4 h. Die Kristallstruktur der Partikel besteht aus Platin- und Palladiumatomen in einem kubisch-flächenzentrierten (*fcc*) Gitter. Diese änderte sich ebenfalls mit der Synthesedauer, genauer mit dem sich ändernden Platingehalt der Teilchen. Die Analyse der EXAFS-Spektren bestätigte die Kern-Schale-Struktur und das Vorliegen eines *fcc*-Kristallgitters. Außerdem zeigte sich, dass ein definierter metallischer Palladiumkern vorhanden ist, der von einer Platinschale umgeben ist, in der der Großteils der Platinatome Palladiumnachbarn besitzt. Wie schon für die Palladium-Platin-Nanoblüten, verbessern sich sowohl die ORR als auch die ECSA durch Einführung des Platins. Die Stabilität der Palladiumwürfel und der Palladium-Platin-Nanopartikel legt nahe, dass es sich um definierte Cluster mit einer stabilen Palladium-Platin-Schale handelt. Impedanzmessungen bestätigten die hohe katalytische Aktivität. Die Analyse der EIS-Spektren zeigte kleine Ladungstransferwiderstände, die auf eine gute Zugänglichkeit der chemisch aktiven Plätze auf der Katalysatoroberfläche hinweisen. Lediglich die Partikel mit 6 und 8 h Synthesedauer zeigten eine geringere katalytische Aktivität, die mit den entsprechenden experimentellen Ergebnissen übereinstimmt.

Um die Bildung und Zersetzung der Oxide auf der Oberfläche der Partikel mit sich änderndem angelegten Potential zu studieren, wurden *in-situ*-XAFS-Messungen durchgeführt (Kapitel 4). Dabei konnte herausgefunden werden, dass alle experimentellen XAFS-Spektren mit nur zwei simulierten Spektren reproduziert werden können. Die beiden Spektren repräsentierten dabei zum Einen die Pt-Pt und Pt-Pd Metallbindungen, zum Anderen die Pt-O-Oxidbindungen,

mit einem größeren Anteil der Metallkomponenten. Wie für die *ex-situ*-EXAFS-Messungen zeigte die Analyse der Spektren die Existenz definiert strukturierter Partikel. Außerdem konnte gezeigt werden, dass die Spektren bei einem Potential von 0.35 V den *ex-situ*-Spektren gleichen. Dies bestätigt die Abwesenheit von Oxiden bei 0.35 V und zeigt, dass es in Abhängigkeit des angelegten Potentials zur Bildung und Auflösung einer Oxidschicht auf der Partikeloberfläche kommt.



Figur 5.1: Bimetallische Katalysatoren für die ORR. PdPt „Nanoflowers“ Partikel (links), PEM-Brennstoffzelle (Mitte), Kern-Schale-Palladium-Platin-Nanopartikel (rechts).

Zusammenfassend konnte gezeigt werden, dass erfolgreich nanoblütenartige und Kern-Schale-Palladium-Platin-Nanopartikel synthetisiert wurden, die eine ausgezeichnete katalytische Aktivität hinsichtlich der Sauerstoffreduktionsreaktion aufweisen. Diese neuartigen, bimetallicen Partikel können mit einfachen Methoden preisgünstig präpariert werden und übertreffen die Katalyseleistung von reinem Platin. In weiteren Studien sollte der Einsatz dieser Katalysatoren in Brennstoffzellen untersucht werden (Figur 5.1). Auch könnte das verwendete Kohlenstoffpulver durch nanostrukturierte Kohlenstoffspezies (z.B. Nanoröhren) ersetzt werden, um die chemische Aktivität noch weiter zu verbessern. Des Weiteren wäre es sinnvoll in der beschriebenen Syntheseprozedur Platin und/oder Palladium durch alternative, preiswertere Metalle (z.B. Eisen, Nickel, Kupfer) zu ersetzen, um kostengünstige, leistungsfähige Katalysatoren für kommerzielle Brennstoffzellen zu entwickeln.

List of Abbreviations

AFC	Alkaline Fuel Cell
AFM	Atomic Force Microscopy
COD	Crystallographic Open Database
CN	Coordination Number
CTAB	Hexadecyltrimethylammonium Bromide
CV	Cyclic Voltammetry
DMFC	Direct Methanol Fuel Cell
DFT	Density Functional Theory
DLS	Dynamic Light Scattering
ECSA	Electro Chemically active Surface Area
EDS	Electron Diffraction Spectroscopy
EIS	Electrochemical Impedance Spectroscopy
EXAFS	Extended X-ray Absorption Fine Structure
<i>fcc</i>	face-centered cubic
FWMH	Full Width Half Maximum
ICP-MS	Inductively Coupled Plasma Mass Spectrometry
ITFA	Iterative Transformation Factor Analysis
ITT	Iterative Target Test
LSV	Linear Sweep Voltammetry
MCFC	Molten Carbonate Fuel Cell
MEA	Membrane Electrode Assembly
NP	NanoParticle
PAFC	Phosphoric Acid Fuel Cell
PCA	Principal Component Analysis
PEM	Proton-Exchange Membrane
PEFMC	Proton-Exchange Membrane Fuel Cell
PVP	PolyVinylPyrrolidone

List of Abbreviations

ORR	Oxygen Reduction Reaction
RDE	Rotational Disk Electrode
RDS	Rate-Determining Step
rpm	rotation per minute
SHE	Standard Hydrogen Electrode
SOFC	Solid Oxide Fuel Cell
TEM	Transmission Electron Microscope
XAFS	X-ray Absorption Fine Structure
XANES	X-ray Absorption Near Edge Structure
XPS	X-ray Photoelectron Spectroscopy
XRD	X-Ray Diffraction

References

- (1) Grove, W. *Philos. Mag. Ser. 3* **1842**, *21*, 417–420.
- (2) Cleveland, C. J.; Morris, C. G., *Fuel Cells*; Elsevier: 2014, pp 323–332; 968 pp.
- (3) Song, C.; Zhang, J. In *PEM Fuel Cell Electrocatalysts and Catalyst Layers*, Zhang, J., Ed.; Springer London: London, 2008, pp 89–134.
- (4) Oldham, K. B.; Myland, J. C.; Bond, A. M. In *Electrochemical Science and Technology*; John Wiley & Sons, Ltd: 2011, pp 55–70.
- (5) Bacon, F. T.; Fry, T. M. *Proc. R. Soc. Lond. Math. Phys. Eng. Sci* **1973**, *334*, 427–452.
- (6) Wang, Y.; Chen, K. S.; Mishler, J.; Cho, S. C.; Adroher, X. C. *Appl. Energy* **2011**, *88*, 981–1007.
- (7) Nørskov, J. K.; Rossmeisl, J.; Logadottir, A.; Lindqvist, L.; Kitchin, J. R.; Bligaard, T.; Jónsson, H. *J. Phys. Chem. B* **2004**, *108*, 17886–17892.
- (8) Lu, Y.; Jiang, Y.; Chen, W. *Nano Energy* **2013**, *2*, 836–844.
- (9) Marković, N. M.; Gasteiger, H. A.; Grgur, B. N.; Ross, P. N. *J. Electroanal. Chem.* **1999**, *467*, 157–163.
- (10) Cai, Z.-x.; Liu, C.-c.; Wu, G.-h.; Chen, X.-m.; Chen, X. *Electrochim. Acta* **2014**, *127*, 377–383.
- (11) Anderson, R. M.; Zhang, L.; Loussaert, J. A.; Frenkel, A. I.; Henkelman, G.; Crooks, R. M. *ACS Nano* **2013**, *7*, 9345–9353.
- (12) Hong, J. W.; Kang, S. W.; Choi, B.-S.; Kim, D.; Lee, S. B.; Han, S. W. *ACS Nano* **2012**, *6*, 2410–2419.
- (13) Higashihara, T.; Matsumoto, K.; Ueda, M. *Polymer* **2009**, *50*, 5341–5357.
- (14) Peighambardoust, S.; Rowshanzamir, S.; Amjadi, M. *Int. J. Hydrog. Energy* **2010**, *35*, 9349–9384.
- (15) Zhang, T.; Anderson, A. B. *Electrochim. Acta* **2007**, *53*, 982–989.
- (16) Yu, W.; Porosoff, M. D.; Chen, J. G. *Chem. Rev.* **2012**, *112*, 5780–5817.
- (17) Viswanathan, V.; Hansen, H. A.; Rossmeisl, J.; Nørskov, J. K. *J. Phys. Chem. Lett.* **2012**, *3*, 2948–2951.

References

- (18) Stephens, I. E. L.; Bondarenko, A. S.; Perez-Alonso, F. J.; Calle-Vallejo, F.; Bech, L.; Johansson, T. P.; Jepsen, A. K.; Frydendal, R.; Knudsen, B. P.; Rossmeisl, J.; Chorkendorff, I. *J. Am. Chem. Soc.* **2011**, *133*, 5485–5491.
- (19) Perez, J.; Villullas, H. M.; Gonzalez, E. R. *J. Electroanal. Chem.* **1997**, *435*, 179–187.
- (20) Markovic, N. M. P. N. R.; Ross, P. N. *CATTECH* **2000**, *4*, 110–126.
- (21) Rhee, C. K.; Kim, B.-J.; Ham, C.; Kim, Y.-J.; Song, K.; Kwon, K. *Langmuir* **2009**, *25*, 7140–7147.
- (22) Porter, N. S.; Wu, H.; Quan, Z.; Fang, J. *Acc. Chem. Res.* **2013**, *46*, 1867–1877.
- (23) Long, N. V.; Yang, Y.; Minh Thi, C.; Minh, N. V.; Cao, Y.; Nogami, M. *Nano Energy* **2013**, *2*, 636–676.
- (24) Kloke, A.; von Stetten, F.; Zengerle, R.; Kerzenmacher, S. *Adv. Mater.* **2011**, *23*, 4976–5008.
- (25) Narayanan, R.; El-Sayed, M. A. *J. Phys. Chem. B* **2003**, *107*, 12416–12424.
- (26) Keith, J. A.; Jerkiewicz, G.; Jacob, T. *ChemPhysChem* **2010**, *11*, 2779–2794.
- (27) Fang, B.; Wanjala, B. N.; Yin, J.; Loukrakpam, R.; Luo, J.; Hu, X.; Last, J.; Zhong, C.J. *Int. J. Hydrogen Energy* **2012**, *37*, 4627–4632.
- (28) Green, C. L.; Kucernak, A. *J. Phys. Chem. B* **2002**, *106*, 1036–1047.
- (29) Liu, A.; Yuan, M.; Zhao, M.; Lu, C.; Zhao, T.; Li, P.; Tang, W. *J. Alloys Comp* **2014**, *586*, 99–104.
- (30) Mu, R.; Guo, X.; Fu, Q.; Bao, X. *J. Phys. Chem. C* **2011**, *115*, 20590–20595.
- (31) Li, J.; Wang, G.; Wang, J.; Miao, S.; Wei, M.; Yang, F.; Yu, L.; Bao, X. *Nano Res* **2014**, *7*, 1519–1527.
- (32) Liu, L.; Samjeské, G.; Takao, S.; Nagasawa, K.; Iwasawa, Y. *J. Power Source* **2014**, *253*, 1–8.
- (33) Marković, N. M.; Schmidt, T. J.; Stamenković, V.; Ross, P. N. *Fuel Cells* **2001**, *1*, 105–116.
- (34) Mendivil Palma, M. I.; Krishnan, B.; Rodriguez, G. A. C.; Das Roy, T. K.; Avellaneda, D. A.; Shaji, S. *J. Nanomater.* **2016**, *2016*, e9651637.
- (35) Wu, S.; Liu, J.; Tian, Z.; Cai, Y.; Ye, Y.; Yuan, Q.; Liang, C. *ACS Appl. Mater. Interfaces* **2015**, *7*, 22935–22940.

- (36) Rousset, J. L.; Stievano, L.; Aires, F. J. C. S.; Geantet, C.; Renouprez, A. J.; Pellarin, M. *J. Catal.* **2001**, *197*, 335–343.
- (37) Liu, Z.; Yu, C.; Rusakova, I. A.; Huang, D.; Strasser, P. *Top. Catal.* **2008**, *49*, 241–250.
- (38) Huang, X.; Li, Y.; Li, Y.; Zhou, H.; Duan, X.; Huang, Y. *Nano Lett.* **2012**, *12*, 4265–4270.
- (39) Liu, J.; Cao, L.; Huang, W.; Li, Z. *J. Electroanal. Chem.* **2012**, *686*, 38–45.
- (40) Ott, A.; Bhargava, S. K.; O’Mullane, A. P. *Surf. Sci.* **2012**, *606*, L5–L9.
- (41) Chu, Y.-Y.; Wang, Z.-B.; Jiang, Z.-Z.; Gu, D.-M.; Yin, G.-P. *J. Power Sources* **2012**, *203*, 17–25.
- (42) Lim, B.; Jiang, M.; Camargo, P. H. C.; Cho, E. C.; Tao, J.; Lu, X.; Zhu, Y.; Xia, Y. *Science* **2009**, *324*, 1302–1305.
- (43) Hui Zhang, M. J. *J. Am. Chem. Soc.* **2011**, *133*, 10422–5.
- (44) Kaito, T.; Mitsumoto, H.; Sugawara, S.; Shinohara, K.; Uehara, H.; Ariga, H.; Takakusagi, S.; Hatakeyama, Y.; Nishikawa, K.; Asakura, K. *J. Phys. Chem. C* **2014**, *118*, 8481–8490.
- (45) Alayoglu, S.; Eichhorn, B. *J. Am. Chem. Soc.* **2008**, *130*, 17479–17486.
- (46) Ocampo, A. L.; Miranda-Hernández, M.; Morgado, J.; Montoya, J. A.; Sebastian, P. J. *J. Power Sources* **2006**, *160*, 915–924.
- (47) Zheng, J.-N.; He, L.-L.; Chen, F.-Y.; Wang, A.-J.; Xue, M.-W.; Feng, J.-J. *Electrochim. Acta* **2014**, *137*, 431–438.
- (48) Wu, Y.-N.; Liao, S.-J.; Guo, H.-F.; Hao, X.-Y. *J. Power Sources* **2013**, *235*, 135–141.
- (49) Geboes, B.; Mintsouli, I.; Wouters, B.; Georgieva, J.; Kakaroglou, A.; Sotiropoulos, S.; Valova, E.; Arnyanov, S.; Hubin, A.; Breugelmans, T. *Appl. Catal. B* **2014**, *150–151*, 249–256.
- (50) Chatenet, M.; Aurousseau, M.; Durand, R.; Andolfatto, F. *J. Electrochem. Soc.* **2003**, *150*, D47–D55.
- (51) Park, K.-W.; Choi, J.-H.; Sung, Y.-E. *J. Phys. Chem. B* **2003**, *107*, 5851–5856.
- (52) Jia, Y.; Su, J.; Chen, Z.; Tan, K.; Chen, Q.; Cao, Z.; Jiang, Y.; Xie, Z.; Zheng, L. *RSC Adv.* **2015**, *5*, 18153–18158.
- (53) Lin, R.; Zhang, H.; Zhao, T.; Cao, C.; Yang, D.; Ma, J. *Electrochim. Acta* **2012**, *62*, 263–268.

References

- (54) Si, F.; Ge, J.; Li, C.; Liang, L.; Liu, C.; Xing, W. *Int. J. Hydrogen Energy* **2014**, *39*, 2489–2496.
- (55) Podlovchenko, B. I.; Krivchenko, V. A.; Maksimov, Y. M.; Gladysheva, T. D.; Yashina, L. V.; Evlashin, S. A.; Pilevsky, A. A. *Electrochim. Acta* **2012**, *76*, 137–144.
- (56) Zhang, H.; Jin, M.; Xia, Y. *Angew. Chem. Int. Ed.* **2012**, *51*, 7656–7673.
- (57) Shiraishi, Y.; Sakamoto, H.; Sugano, Y.; Ichikawa, S.; Hirai, T. *ACS Nano* **2013**, *7*, 9287–9297.
- (58) Paulus, U. A.; Wokaun, A.; Scherer, G. G.; Schmidt, T. J.; Stamenkovic, V.; Markovic, N. M.; Ross, P. N. *Electrochim. Acta* **2002**, *47*, 3787–3798.
- (59) Xu, Y.; Hou, S.; Liu, Y.; Zhang, Y.; Wang, H.; Zhang, B. *Chem. Commun* **2012**, *48*, 2665–2667.
- (60) Li, Y.; Qi, W.; Huang, B.; Ji, W.; Wang, M. *J. Phys. Chem. C* **2013**, *117*, 15394–15401.
- (61) Zhang, H.; Jin, M.; Liu, H.; Wang, J.; Kim, M. J.; Yang, D.; Xie, Z.; Liu, J.; Xia, Y. *ACS Nano* **2011**, *5*, 8212–8222.
- (62) Choi, B.-S.; Lee, Y. W.; Kang, S. W.; Hong, J. W.; Kim, J.; Park, I.; Han, S. W. *ACS Nano* **2012**, *6*, 5659–5667.
- (63) Thanasilp, S.; Hunsom, M. *Electrochim. Acta* **2011**, *56*, 1164–1171.
- (64) Fu, G.; Wu, K.; Lin, J.; Tang, Y.; Chen, Y.; Zhou, Y.; Lu, T. *J. Phys. Chem. C* **2013**, *117*, 9826–9834.
- (65) Doña Rodríguez, J. M.; Herrera Melián, J. A.; Pérez Peña, J. *J. Chem. Educ.* **2000**, *77*, 1195.
- (66) Mayrhofer, K. J. J.; Strmcnik, D.; Blizanac, B. B.; Stamenkovic, V.; Arenz, M.; Markovic, N. M. *Electrochim. Acta* **2008**, *53*, 3181–3188.
- (67) Vengrenovich, R. D.; Ivanskii, B. V.; Panko, I. I.; Yarema, S. V.; Kryvetskyi, V. I.; Stasyk, M. O. *J. Nanomater.* **2014**, *2014*, e821584.
- (68) Ahluwalia, R. K.; Arisetty, S.; Peng, J.-K.; Subbaraman, R.; Wang, X.; Kariuki, N.; Myers, D. J.; Mukundan, R.; Borup, R.; Plevaya, O. *J. Electrochem. Soc.* **2014**, *161*, F291–F304.
- (69) Ye, X.; Yang, Q.; Wang, Y.; Li, N. *Talanta* **1998**, *47*, 1099–1106.

- (70) Li, D.; Wang, C.; Strmcnik, D. S.; Tripkovic, D. V.; Sun, X.; Kang, Y.; Chi, M.; Snyder, J. D.; van der Vliet, D.; Tsai, Y.; Stamenkovic, V. R.; Sun, S.; Markovic, N. M. *Energy Environ. Sci.* **2014**, *7*, 4061–4069.
- (71) Peng, Z.; Yang, H. *Nano Today* **2009**, *4*, 143–164.
- (72) Li, H.; Sun, G.; Li, N.; Sun, S.; Su, D.; Xin, Q. *J. Phys. Chem. C* **2007**, *111*, 5605–5617.
- (73) Yang, H.; Vogel, W.; Lamy, C.; Alonso-Vante, N. *J. Phys. Chem. B* **2004**, *108*, 11024–11034.
- (74) Hwang, B. J.; Kumar, S. M. S.; Chen, C. -H.; Monalisa; Cheng, M. -Y.; Liu, D.-G.; Lee, J.-F. *J. Phys. Chem. C* **2007**, *111*, 15267–15276.
- (75) Chen, C.-Y.; Chen, C.-C.; Hsu, S.-W.; Lai, M.-P.; Lai, W.-H.; Yang, W.-M. *Energy Procedia* **2012**, *29*, 64–71.
- (76) Escaño, M. C. S.; Kasai, H. *J. Power Sources* **2014**, *247*, 562–571.
- (77) Randles, J. E. B. *Discuss. Faraday Soc.* **1947**, *1*, 11–19.
- (78) Harrington, D. A.; van den Driessche, P. *Electrochim. Acta* **2011**, *56*, 8005–8013.
- (79) Otomo, J.; Li, X.; Kobayashi, T.; Wen, G.; Nagamoto, H.; Takahashi, H. *J. Electroanal. Chem.* **2004**, *573*, 99–109.
- (80) Gabrielli, C.; Keddam, M.; Portail, N.; Rousseau, P.; Takenouti, H.; Vivier, V. *J. Phys. Chem. B* **2006**, *110*, 20478–20485.
- (81) Mayrhofer, K. J. J.; Blizanac, B. B.; Arenz, M.; Stamenkovic, V. R.; Ross, P. N.; Markovic, N. M. *J. Phys. Chem. B* **2005**, *109*, 14433–14440.
- (82) Macdonald, D. D.; Sikora, E.; Engelhardt, G. *Electrochim. Acta* **1998**, *43*, 87–107.
- (83) Shao-Horn, Y.; Sheng, W. C.; Chen, S.; Ferreira, P. J.; Holby, E. F.; Morgan, D. *Top. Catal.* **2007**, *46*, 285–305.
- (84) Gasteiger, H. A.; Kocha, S. S.; Sompalli, B.; Wagner, F. T. *Appl. Catal., B* **2005**, *56*, 9–35.
- (85) Shao, M.; Liu, P.; Zhang, J.; Adzic, R. *J. Phys. Chem. B* **2007**, *111*, 6772–6775.
- (86) Zhou, Z.-M.; Shao, Z.-G.; Qin, X.-P.; Chen, X.-G.; Wei, Z.-D.; Yi, B.-L. *Int. J. Hydrogen Energy* **2010**, *35*, 1719–1726.
- (87) Yang, J.; Lee, J. Y.; Zhang, Q.; Zhou, W.; Liu, Z. *J. Electrochem. Soc.* **2008**, *155*, B776–B781.

References

- (88) Dutta, A.; Datta, J. *Int. J. Hydrogen Energy* **2013**, *38*, 7789–7800.
- (89) Gražulis, S.; Daškevič, A.; Merkys, A.; Chateigner, D.; Lutterotti, L.; Quirós, M.; Serebryanaya, N. R.; Moeck, P.; Downs, R. T.; Bail, A. L. *Nucl. Acids Res.* **2012**, *40*, D420–D427.
- (90) Kuo, Y.-K.; Liou, B.-T.; Yen, S.-H.; Chu, H.-Y. *Opt. Commun.* **2004**, *237*, 363–369.
- (91) Lubarda, V. A. *Mech. Mater.* **2003**, *35*, 53–68.
- (92) Ankudinov, A. L.; Rehr, J. J. *Phys. Rev. B* **1997**, *56*, R1712–R1716.
- (93) Toshima, N.; Yonezawa, T. *New J. Chem.* **1998**, *22*, 1179–1201.
- (94) Long, N. V.; Duy Hien, T.; Asaka, T.; Ohtaki, M.; Nogami, M. *Int. J. Hydrogen Energy* **2011**, *36*, 8478–8491.
- (95) Kim, C.; Kim, J.; Yang, S.; Lee, H. *RSC Adv.* **2014**, *4*, 63677–63680.
- (96) Jebaraj, A. J. J.; Georgescu, N. S.; Scherson, D. A. *J. Phys. Chem. C* **2016**, *120*, 16090–16099.
- (97) Zhang, G.; Shao, Z.-G.; Lu, W.; Xiao, H.; Xie, F.; Qin, X.; Li, J.; Liu, F.; Yi, B. *J. Phys. Chem. C* **2013**, *117*, 13413–13423.
- (98) Thanasilp, S.; Hunsom, M. *Renewable Energy* **2011**, *36*, 1795–1801.
- (99) Lee, C.-L.; Chiou, H.-P.; Wu, S.-C.; Wu, C.-C. *Electrochim. Acta* **2010**, *56*, 687–692.
- (100) Gupta, V. K.; Yola, M. L.; Atar, N.; Üstündağ, Z.; Solak, A. O. *J. Mol. Liq.* **2014**, *191*, 172–176.
- (101) Golikand, A. N.; Asgari, M.; Lohrasbi, E. *Int. J. Hydrogen Energy* **2011**, *36*, 13317–13324.
- (102) Bele, M.; Jovanovič, P.; Pavlišč, A.; Jozinovič, B.; Zorko, M.; Rčnik, A.; Chernyshova, E.; Hočevar, S.; Hodnik, N.; Gabersček, M. *Chem. Commun.* **2014**, *50*, 13124–13126.
- (103) Cochell, T.; Manthiram, A. *Langmuir* **2012**, *28*, 1579–1587.
- (104) Oezaslan, M.; Hasché, F.; Strasser, P. *J. Phys. Chem. Lett.* **2013**, *4*, 3273–3291.
- (105) Savadogo, O.; Lee, K.; Oishi, K.; Mitsushima, S.; Kamiya, N.; Ota, K.-I. *Electrochem. Commun.* **2004**, *6*, 105–109.
- (106) Zhang, H.; Yin, Y.; Hu, Y.; Li, C.; Wu, P.; Wei, S.; Cai, C. *J. Phys. Chem. C* **2010**, *114*, 11861–11867.
- (107) Gómez-Marín, A. M.; Rizo, R.; Feliu, J. M. *Beilstein J. Nanotechnol.* **2013**, *4*, 956–967.

- (108) Zhou, R.; Zheng, Y.; Jaroniec, M.; Qiao, S.-Z. *ACS Catalysis* **2016**, *6*, 4720–4728.
- (109) Liu, L.; Samjeske, G.; Nagamatsu, S.-i.; Sekizawa, O.; Nagasawa, K.; Takao, S.; Imaizumi, Y.; Yamamoto, T.; Uruga, T.; Iwasawa, Y. *J. Phys. Chem. C* **2012**, *116*, 23453–23464.
- (110) Antoine, O.; Bultel, Y.; Durand, R. *J. Electroanal. Chem.* **2001**, *499*, 85–94.
- (111) Eberle, D.; Horstmann, B. *Electrochim. Acta* **2014**, *137*, 714–720.
- (112) Holewinski, A.; Linic, S. *J. Electrochem. Soc.* **2012**, *159*, H864–H870.
- (113) Wu, S.-L.; Orazem, M. E.; Tribollet, B.; Vivier, V. *J. Electroanal. Chem.* **2015**, *737*, 11–22.
- (114) Nogami, M.; Koike, R.; Jalem, R.; Kawamura, G.; Yang, Y.; Sasaki, Y. *J. Phys. Chem. Lett.* **2010**, *1*, 568–571.
- (115) Wiltshire, R. J. K.; King, C. R.; Rose, A.; Wells, P. P.; Hogarth, M. P.; Thompsett, D.; Russell, A. E. *Electrochim. Acta* **2005**, *50*, 5208–5217.
- (116) Halder, A.; Jia, Q.; Trahan, M.; Mukerjee, S. *Electrochim. Acta* **2013**, *108*, 288–295.
- (117) Carvalho, A. R.; Wattoom, J.; Zhu, L.; Brereton, R. G. *Analyst* **2006**, *131*, 90–97.
- (118) Björling, A.; Ahlberg, E.; Feliu, J. M. *Electrochem. Commun.* **2010**, *12*, 359–361.
- (119) Rossberg, A.; Scheinost, A. C. *Anal. Bioanal. Chem.* **2005**, *383*, 56.
- (120) Rossberg, A.; Ulrich, K.-U.; Weiss, S.; Tsushima, S.; Hiemstra, T.; Scheinost, A. C. *Environ. Sci. Technol.* **2009**, *43*, 1400–1406.
- (121) Abdi, H.; Williams, L. J. *Wiley Interdiscip. Rev. Comput. Stat.* **2010**, *2*, 433–459.
- (122) Malinowski, E. L.; Howery, D. G., *Factor analysis in chemistry*; John Wiley New York, Brisbane: 1980, 251p.
- (123) Rehr, J. J.; Albers, R. C. *Rev. Mod. Phys.* **2000**, *72*, 621–654.
- (124) Nagamatsu, S.-i.; Arai, T.; Yamamoto, M.; Ohkura, T.; Oyanagi, H.; Ishizaka, T.; Kawanami, H.; Uruga, T.; Tada, M.; Iwasawa, Y. *J. Phys. Chem. C* **2013**, *117*, 13094–13107.
- (125) Kaiser, H. F. *Psychometrika* **1958**, *23*, 187–200.
- (126) Jacob, T. *J. Electroanal. Chem.* **2007**, *607*, 158–166.
- (127) Park, J. H.; Sohn, Y.; Jung, D. H.; Kim, P.; Joo, J. B. *J. Ind. Eng. Chem.* **2016**, *36*, 109–115.

Acknowledgements

Working on a really interesting research project, the development of new catalyst for the oxygen reduction reaction, could not be possible without the support of several people. Thanks to Dr. Anna Ignaszak who offered me the opportunity to work on the PtPd nanoparticles, with different techniques of synthesis and characterization. A warm thank to Prof. Dr. Ulrich S. Schubert and Dr. Christian Friebe for their support to finish my thesis after the departure of Anna Ignaszak. Without them, it would not be possible to end it.

I also would like thank Dr. Andreas C. Scheinost, Dr. Marisol J. Lozano-Rodriguez and all the research group of the Rossendorf beamline in the ESRF for their warm welcome and their help to realize the XAFS measurement and the data analysis. The work in cooperation with Dr. Scheinost was really interesting, permitted me to study the catalysts using a Synchrotron beamline and to present the result of our study in publications. The XAFS study would not be possible without Dr. Wolfram Calvet and Dr. Artur Braun who permit me to discover and realize previous XAFS study in the Helmholtz Zentrum in Berlin and who recommended me to Dr. Andreas C. Scheinost. I am grateful to the technicians of the workshop of the university for their help to fabricate the experimental cells. I am thankful to Dr. Andreas Undisz and Dr. Stefanie Höppener for their cooperation to characterize the particles with TEM and EDS measurements. I appreciated the assistance of Dr. Igor Perevyazko for the access to a high speed centrifugation machine and Dr. Sindy Fuhrmann for the XRD measurements and her help for the Rietveld Analysis.

I would like to thank Christofer and Heike for the nice atmosphere in our office and all the members of the ITUC for the friendly ambiance in the institute and their help during all my thesis. I am also grateful to the graduate academy and the Sprachenzentrum of the Friedrich Schiller University with the opportunity to do workshops and learn German.

Thank to all my friends, french and german who support me, with them it is never boring. And really warm thanks my girlfriend Anja who always support and help me to work but also to discover Germany make sport and travel, to share a nice life together. A little thought for my parents, my brother and all my family for their constant support during my life.

Peer-reviewed publications

- **S. Tymen**, A. C. Scheinost, M. J. Lozano-Rodriguez, C. Friebe, U. S. Schubert, "From cubic palladium to concave core-shell platinum palladium nanoparticles: Evolution of their structure and the electrochemical properties", *Journal of the Electrochemical Society*, *accepted 2017*.
- **S. Tymen**, A. C. Scheinost, C. Friebe, U. S. Schubert, "*In-situ* XAFS characterization of PtPd nanoparticles synthesized by galvanic replacement", *Adv. Nanoparticles*, **2017**, 6, 75–91.
- **S. Tymen**, A. Undisz, M. Rettenmayr, A. Ignaszak, "Pt-Pd catalytic nanoflowers: Synthesis, characterization and the activity toward electrochemical oxygen reduction", *J. Mater. Res.*, **2015**, 30, 2327–2339.

Poster presentation

- **S. Tymen**, Andreas C. Scheinost "In-situ XAFS characterization of PtPd nanoparticles synthesized by galvanic replacement" Ninth Joint BER II and BESSY II User Meeting 2017, December 13-15, **2017**, Helmholtz Zentrum Berlin, Berlin, Germany.
- **S. Tymen** "From Pd to PdPt nanoparticles : an interesting evolution from structure to electrochemical properties" (updated poster), Heat & Electricity Storage, 3rd Symposium "Storing Renewable Energy for Future Mobility", Oktober 26, **2015**, Villigen, Switzerland.
- **S. Tymen** "From Pd to PdPt nanoparticles: An interesting evolution from structure to electrochemical properties", 22 August, **2015**, Rügen, Germany.

Summer school

- RACIRI summer school: "Time-resolved and *in-situ* studies of materials: Basics and applications", 22 - 29 August **2015**, Rügen, Germany.;

Declaration of Authorship / Selbstständigkeitserklärung

Ich erkläre, dass ich die vorliegende Arbeit selbstständig und unter Verwendung der angegebenen Hilfsmittel, persönlichen Mitteilungen und Quellen angefertigt habe.

I certify that the work presented here is, to the best of my knowledge and belief, original and the result of my own investigations, except as acknowledged, and has not been submitted, either in part or whole, for a degree at this or any other university.

Jena,

.....

Simon Tymen

Publication 1

Pt-Pd catalytic nanoflowers: Synthesis, characterization, and the activity
toward electrochemical oxygen reduction

S. Tymen, A. Undisz, M. Rettenmayr, A. Ignaszak

J. Mater. Res. **2015**, *30 (15)*, 2327. DOI:10.1557/jmr.2015.212

Reproduced by the permission of the Cambridge University Press.

Pt-Pd catalytic nanoflowers: Synthesis, characterization and the activity toward electrochemical oxygen reduction

Simon Tymen

Department of Chemical and Earth Sciences, Institute of Organic and Macromolecular Chemistry (IOMC), Friedrich-Schiller University, 07743 Jena, Germany

Andreas Undisz and Markus Rettenmayr

Department of Physics, Institute of Metallic Materials, Friedrich-Schiller University, 07743 Jena, Germany

Anna Ignaszak^a

Institute of Organic and Macromolecular Chemistry (IOMC), Friedrich-Schiller University, 07743 Jena, Germany

(Received 22 April 2015; accepted 23 June 2015)

This work aims to synthesize PtPd catalytic clusters and to study the effect of the particle size, curvature and possible alloying on the catalytic activity for oxygen reduction reaction, chemical stability, the mass-transfer of redox active species toward catalytic sites and the electro-kinetic of the oxygen reduction reaction (ORR) process. The particle size, the chemical composition of the catalyst surface significantly influence the electrochemically active surface area and catalytic activity toward oxygen reduction, regardless the particle size. The best catalytic activity was accomplished for 45 nm clusters due to possible alloying that enhance the O₂ adsorption and dissociation. The complementary impedance studies demonstrated that 45 nm cluster has also the shortest effective diffusion length and the highest reaction rate constant for all morphologies, indicating on superior reactant transport to the catalytic sites. The 45 nm clusters showed improved electrochemical stability that is believed to be the combined effect of alloying and the compactness of the structure.

I. INTRODUCTION

Among various noble metal catalysts, platinum materials are of special importance owing to their catalytic activity toward processes like hydrogenation, electrode reactions in many types of fuel cells, air batteries, water electrolysis or sensor applications. The activity of Pt can be improved by modifications of its electronic, physical and geometrical structures in presence of other elements. One of the most important in tuning the catalytic activity of Pt-based clusters is their size, shape and the composition. For bimetallic nanoparticles, three categories can be defined depending on the distribution of individual atoms, which are a core-shell, alloy, and intermetallic structures. Concerning the application of Pt-based catalysts, one of the most serious barriers for large-scale production remains the prohibitive cost of highly expensive Pt. This will be critical for scaling-up electrodes for fuel cells and metal-air batteries. Generally, there are three ways to reduce the Pt content, which are (i) Pt electrodes with an expanded electrochemically active surface (Pt particles of nanosize), (ii) a partial substitution of Pt atoms with cheaper metals as transition metals

(M = Fe, Co, Ni, Cr, etc.) in alloy catalysts^{15,17} or (iii) designing so called the Pt-skin core-shell morphology (Pt-based monolayer (Pt₁M_L) deposited onto the surface of cheaper metal (e.g. transition metal).^{18,20} Regardless of lowering the cost, such PtM clusters bring improved activity for electrochemical oxygen reduction in comparison to a pure Pt.^{21–24} Although, the activity enhancement is accomplished, these types of bimetallic catalysts suffer from poor durability under high positive potential and at low or cathodic conditions in proton exchange membrane (PEM) fuel cells. The dissolution of transition metals at operating cathode conditions significantly reduces the durability of the catalyst. To minimize this effect, one of the most promising (although the cheapest) will be the Pt-based alloy, e.g., PtPd. Palladium possesses similar electronic configuration and crystallographic features to Pt,²⁶ more importantly, the stability of Pd in acidic media is comparable to Pt.^{27,28} The cost of palladium is about two times less than that of Pt since the Pd resources are more abundant. With respect to the activity of PtPd cluster, enhancement of oxygen reduction process catalyzed by PtPd alloy has been reported and demonstrated as so-called synergistic effect and related to the shifting of negative electronic effect (electrons from Pd orbitals) toward the negatively charged Pt atoms in PtPd cluster facilitate the dissociation of molecular oxygen on the Pt surface, resulting in faster electrochemical reduction of oxygen atoms.^{29,30}

Contributing Editor: Xiaobo Chen

^aAddress all correspondence to this author.

e-mail: anna.ignaszak@uni-jena.de

DOI: 10.1557/jmr.2015.212

The most critical in tuning the PtPd particle size and shape are the preparation conditions. This work aims to study PtPd clusters of bigger size and specific shape ("nanoflowers") synthesized using chemical approaches were proposed including the co-precipitation, impregnation, microemulsion, polyol, microwave-assisted, and c-irradiation. The proposed synthesis is less toxic and is easy to scale up while generating significantly less organic waste in comparison to some methods discussed above. In our approach, we change the sequence of mixing of metal precursors to influence the particle size/shape/surface composition. The transmission electron microscopy (TEM) morphology observations will be correlated with electrochemical activity and long term stability toward oxygen reduction. The cyclic voltammetry (CV) will be used to calculate the electrochemically active surface area (ECSA) using hydrogen under potential deposition method and the linear sweep voltammetry applied to Koutecky-Levich analysis provide the necessary kinetic parameters, such as the exchange current density, activity, and Tafel parameters. Furthermore, the impedance spectroscopy will complement the degradation studies with interplay of the size, surface composition, and curvature to search for the morphology with desired electrochemical stability.

II. EXPERIMENTAL

A. Materials

Sodium tetrachloropalladate (PdCl_4 , 98%), potassium tetrachloroplatinate (PtCl_4 , 98%), ascorbic acid (AA, 98%), potassium bromide (KBr, 99%) and Nafion[®] perfluorinated resin solution (5 wt%) and perchloric acid (HClO_4 , 67% analytical grade) were purchased from Sigma Aldrich, isopropyl alcohol (IPA, 99.5%) from Merck and cetyl-trimethylammonium bromide (CTAB, 98%) from Alfa Aesar. The commercial carbon black Vulcan XC-72R was supplied from Cabot Inc. All the solutions for the synthesis were prepared using ultrapure water (18 M Ohms). High purity nitrogen and oxygen (both 99.999%) were used for purging the electrolyte.

B. Characterization

TEM-energy-dispersive x-ray (EDX) observation were carried out using a high resolution transmission electron microscope JEOL JEM-3010 operating at 300 kV coupled with a x-ray analyzer Oxford. Electrochemical experiments were carried out on a Princeton Applied Research VersaSTAT MC potentiostat in an electrochemical cell containing a Pt counter electrode ($1\text{g}/\text{Pt}$, 654 mV in saturated K_2SO_4) as a reference electrode and PtPd/C ink casted onto glassy carbon rotating disk electrode (Princeton Applied Research, RDE 0008) with a geometric area of 1.9635 cm^2 as a working electrode. Electrochemical measurements were carried out in 0.1 M HClO_4 purged with N_2 or O_2 .

for 30 min prior to experiment. Before casting the glassy carbon disk of 0.5 cm diameter (PINE Instrument Company) was mechanically polished with 0.05 μm Al_2O_3 slurry (Cypress Systems, Inc.), then rinsed in deionized water, cleaned ultrasonically in ultrapure water for 5 min followed by rinsing in ultrapure isopropanol and acetone. A standard ink containing PtPd/C catalyst powder (9 mg), 0.25 mL of water and 2.25 mL of isopropyl alcohol was sonicated for 15 min and 1 μL of ink was deposited on RDE glassy carbon. 7 mL of Nafion[®] solution (volumetric ratio of Nafion[®] methanol was 1:100) was casted onto the catalyst and dried in ambient conditions. The electrochemical electrode conditioning was conducted by scanning potential from 50 to 1200 mV (versus standard hydrogen electrode) at the scan rate of 200 mV s⁻¹. The CV was applied to estimate the electrochemical area of the metallic fraction by applying the hydrogen under-potential position method in a purged 0.1 M HClO₄ electrolyte in the potential range from 50 to 1200 mV and a scan rate of 50 mV s⁻¹. The catalytic activity for oxygen reduction was investigated using linear scan voltammetry (LSV) applied to the rotating disk electrode in a potential range from 250 to 1200 mV with the scan rate of 5 mV s⁻¹ and the rotation speed of 1600 rpm in a saturated electrolyte. A long-term stability test was performed by scanning potential from 50 to 1200 mV at 200 mV s⁻¹ using electrolyte with an N₂ blanket (typically 2000 CV scans without rotation of the electrode). The CV and LSV voltammograms were recorded after each degradation test and compared to the same scans for the fresh electrode. The degradation studies were carried out using the electrochemical impedance spectroscopy that frequency range from 0.01 Hz to 100 kHz by applying the potential amplitude of 10 mV at the constant polarization of 508 mV. The fresh and degraded samples impedance modeling was carried out using ZView software (Scribner Associates Inc.) All experiments were done at ambient temperature (20 °C).

C. Synthesis of PtPd catalytic clusters

In a typical synthesis route, 1 mL of PtCl₄ aqueous solution ($5 \cdot 10^{-2}$ mol L⁻¹) and 1 mL of Na₂PdCl₄ ($5 \cdot 10^{-2}$ mol L⁻¹) were mixed with 10 mL of aqueous solution CTAB surfactant ($8 \cdot 10^{-2}$ mol L⁻¹) and homogenized under sonication for 2 min. 10 mL of 0.1 mol L⁻¹ ascorbic acid (reducing agent) was introduced and the solution heated at 90 °C for 3.5 h under magnetic stirring (dark brown color of the reaction mixture indicated the colloidal metal formation). The reaction time was adjusted experimentally to generate particles with desired size in an extended time of reaction leads to a significant metal agglomeration. The PtPd cluster fabricated using this recipe is denoted as 30NP and is the control sample. Following the method proposed in literature we studied the effect of KBr as a shape controlling agent and introduced 0.833 g of ultrapure mixture of Pt and Pd precursors (before adding ascorbic acid reducing agent) following the same steps for the control sample. The product generated in the presence of KBr was denoted as 60NP. In addition, we fabricated PtPd clusters in the presence of KBr shape controlling agent in two-step synthesis according to Ref. 47 where Pd seeds were fabricated following the same procedures as 30NP and the Pt precursor (K₂PtCl₄) was introduced allowing to generate second potential fraction (shell) over the Pd (the sample is denoted as 45NP). For the samples 45NP and 60NP, the synthesis was carried out for 17 h. This will give some indication with respect to the preference of the particle shape and composition (alloying/core-shell structure) on the catalytic activity and electrochemical stability. To generate a high surface area catalytic bimetallic clusters were decorated on a commercial carbon black Vulcan XC72R. To accomplish PtPd-C with the 20 wt% of a total metal content, the stoichiometric amount of Pt and Pd was mixed with a suspension of PtPd clusters pH 1 and adjusted by 2 M HCl and left under magnetic stirring for 20 h. Afterward, the mixture was washed in ultrapure water under vacuum filtration and dried overnight.

III. RESULTS AND DISCUSSION

A. Materials characterization

Figure 1 represents TEM images of nanoflowers supported on a high surface area carbon Vulcan XC72R (lower magnification image) and without carbon (higher magnification inserts). Figure 1(a) shows catalyst synthesized with KBr and with simultaneous reduction of Pd and Pt metals (precursors mixed before the reduction is initiated 30NP), Fig. 1(b) represents the sample generated in subsequent of Pd and Pt the presence of KBr (45NP) and in Fig. 1(c) nanoflowers were fabricated by simultaneous mixing of Pd and Pt KBr (60NP). An average size of metallic clusters decorated on carbon was estimated using ImageJ software giving the particle size distribution file as at least 200 counts from the corresponding TEM image. Regarding the 30NP sample [Fig. 1(a)], the average particle size is 30 nm and the majority of particles have a square-like shape while other morphologies are rather spherical [Figs. 1(b) and 1(c) inserts]. We can easily recognize a difference in surface roughness for all structures. For instance, the sample 30NP in Fig. 1(a) shows a porous surface consisting of interconnected smaller Pt grains (< 3 nm size) decorated onto Pd core. The interesting is a compactness of the Pt "corona" t

for 30NPs are less dense when comparing to other Fig. 1(c), small individual particles of 5 nm size are structures, especially sample 45NP [Fig. 1(b)]. Although composed of pure Pt. The distribution of Pt and Pd KBr was introduced for the synthesis of 45NPs, we predict that the extended synthesis time results in a larger grain size for 45NPs. The density of corona" will be then also affected by the annealing time leading to 30NP, 45NP, and 60 NP.

interconnected Pt structure for 45NP. A similar compact-

ness is observed for the 60NP sample concerning the effect of KBr, we do not observe any significant

structural differences except that both KBr-assisted syn-

theses deliver more dense (compact) nanoflowers.

Comparable morphologies were recently reported by other group.⁴⁸

EDX elemental mapping of individual particles revealed the following composition for the sample

30NP [Fig.1(a)] it is 60 wt% of Pd and to 40 wt% of Pd, for sample 45NP [Fig.(b)] it is 55 wt% Pd and

45 wt% Pt and for sample 60NP [Fig. 1(c)] it is 67.5 wt% Pd and 32.5 wt% of Pt. With respect to theoretically

assumed composition of Pt to Pd (1:1 weight ratio), the sample 45NP is the closest to the stoichiometric

formulation. The difference in chemical composition for 30NPs and 60NPs is a result of the Pt precipitation as

confirmed by a spot-resolved EDX mapping [e.g., the scan rate (in this study 20 mV s

B. Electrochemical studies

1. ECSA and mass activity for oxygen reduction

The ECSA of the catalysts was determined using

hydrogen underpotential deposition method.⁴⁹ The charge of hydrogen monolayer adsorption/desorption on

the metal surface was determined by the integration of relevant peaks identified in the potential range from 0.

to 0.4 V in cyclic voltammograms (Fig. 2). The charge of hydrogen activity on PtPd is further calculated according to the Eq.(1):⁴⁹

$$Q_H = \frac{1}{4} \frac{R_{id} E}{m} ; \quad \delta 1P$$

where i is the current (A), E is the potential (V) and m is

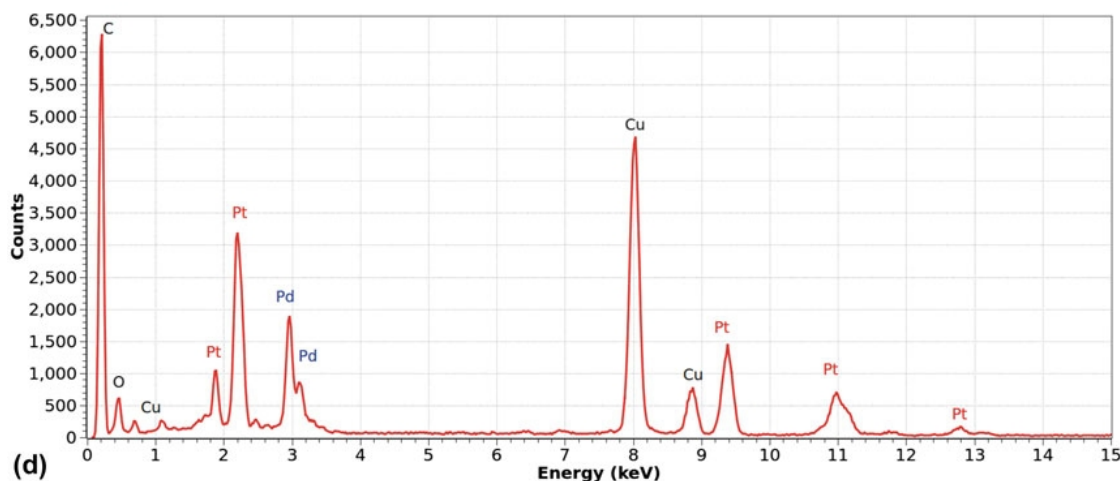
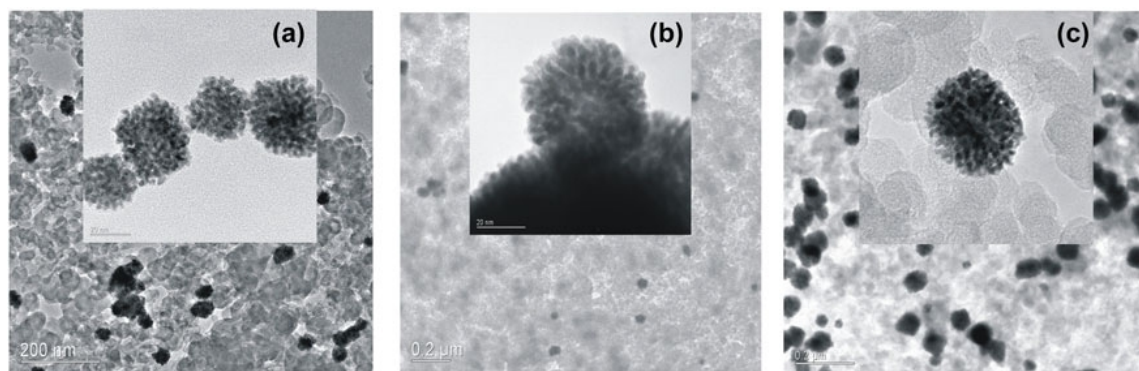


FIG. 1. TEM image of (a) 30NP, (b) 45NP, 60NP supported on carbon (low magnification) and without carbon (inserts) together with spectrum [(d); an example for 45NP].

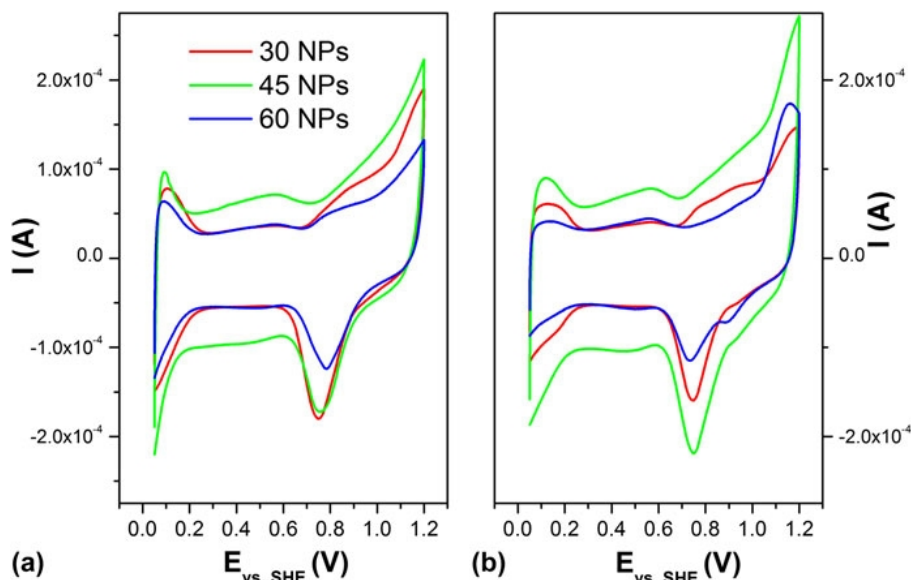


FIG. 2. Cyclic voltammograms (a) for fresh catalyst and (b) after degradation.

Furthermore, the surface area ($A_{\text{H}}^{\text{ads}}$) was calculated at 0.5 V and is the kinetic current density. Furthermore, by comparing the charge of hydrogen evolution (Q_{H}) to the theoretical charge of hydrogen adsorption on polycrystalline Pt (2.1 · 10⁴ C cm²)⁴⁹ and normalized to the total metal loading per geometric area of the working electrode:

$$ECSA \approx \frac{1}{2.1 \cdot 10^4} \frac{Q_{\text{H}}}{m_{\text{PtPd}}} \quad (2)$$

where m (g) is the mass of PtPd on glassy carbon electrode and 2.1 · 10⁴ C cm² is the reference. Figure 2 represents voltammograms of samples as prepared (a) and after the degradation tests (b).

The mass activity for electrocatalytic hydrogen evolution was analyzed using linear sweep voltammograms and corresponding mathematical models applied to rotating disk electrode (in our study the electrode rotation speed is 1600 rpm) in the range of 0.35–0.7 V, where the process is controlled by mass transport and it can be well resolved from a mixed mass-kinetic control (between 0.3 and 0.85 V) and pure kinetic region above 0.85 V (Fig. 3 and 4). The electrode rotation ensures fast transport of redox species from bulk electrolyte to the electrode surface. Due to the complexity of morphologies, the mass activity kinetic current normalized to the metal load, A g⁻¹, will be corrected as follows:⁵⁰

$$\frac{1}{i} \approx \frac{1}{i_d} + \frac{1}{i_k} \quad (3)$$

where i is a total current density recorded in LSV (diffusion), i_d is the diffusion (mass-transport) limited current density (diffusion) for the commercial product. Although there are

$$i_k \approx \frac{i_{0.85}}{i_{0.85} - i} \quad (4)$$

where $i_{0.85}$ is the current density at 0.85 V, the mass-normalized (m) ORR activity will be:

$$i_{\text{mass}} \approx \frac{i_k}{m_{\text{PtPd}}} \quad (5)$$

The calculated surface area and activities are summarized in Table 1. In the potential range from 0.05 to 0.3 V, we observe weakly-resolved features of hydrogen adsorption on polycrystalline Pt (and Pd). The intensity of these broad waves depends on the particle size with general trend for bigger particles and smaller are peaks of hydrogen evolution (blue curve is assigned to 60 NP sample with the biggest particles of 60 nm). Surprisingly, although the 45 NP has an average particle size smaller than 60 NP, the calculated surface area is lower for the fresh 45 NP sample and significantly higher after degradation. This increase of ECSA for 45 NPs after electrochemical cycling is an effect of the surface cleaning from CTAB surfactant (i.e., leached during the electrochemical cycling). The ECSA for all in-house made nanoflowers is similar to the reported pure Pt catalyst with 30 nm particle size of 1.30 m² g⁻¹ and, as expected, lower than ECSA of the baseline (commercial Pt/C catalyst, Table I) due to a significant difference in metal particle size (Pt particle of 3–5 nm typically for the commercial product). Although there are

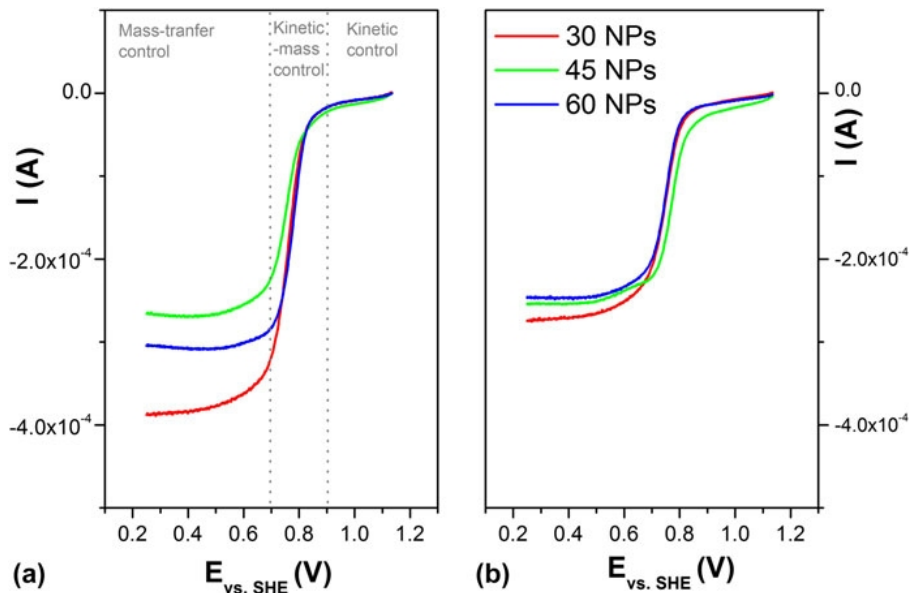


FIG. 3. Linear sweep voltammograms at a scan rate of 10 mV s⁻¹ and a rotation speed of 1600 rpm for electrocatalytic reduction of oxidized methanol for (a) fresh and (b) degraded catalysts.

minordifferences in the surface area for fresh samples (45 NPs (Pd:Pt 50:50), surprisingly these nano-significant variations are observed during an accelerated degradation test. In this respect, the surface area lost (ECSA (Table I). This can be due to the surface restructuring caused by Pt dissolution or metal agglomeration (also of the catalyst upon polarization at low pH (in our called Ostwald ripening) after long-term potential scans this might be the positive effect) the electro-ening up to 1.2 V. The ECSA results of degraded catalysts are summarized in Table I. The ECSA of degraded catalysts (Table I) revealed that the sample with the smallest particle size (30NP) has 19.5% of ECSA while the catalyst with 60 nm clusters (60NP) shows over 60% of ECSA lost under the same conditions. Regarding 45NP size, the highest ECSA, we could expect the opposite since the electrochemical activation is faster for smaller particles. Also, it is important to consider that the process is determined by net competition between Pt dissolution and the surface passivation (in this case protection by PtO) as nucleation centers for the Pt atom (in other words with the generated PtO). The stability of PtO is higher for larger particles. PtO is generated on metallic surface (also PtOH, PtO) and the stability of PtO is higher for larger particles. Therefore, the stability of 30NP and 60NP contradicts with the corresponding mechanism of Pt dissolution. Considering the nanoflower curvature, Pt-Pd alloying process in 45NPs (and were not generated could also expect that less "dense" 30NP structure for 30NP and 60NP). X-ray diffraction (XRD) studies and dissolve faster than 60NPs, which is not observed here. The lattice constant calculation (included into supporting This again indicates that the degradation of in-house generated morphologies should be affected by other parameters, e.g. their chemical composition (in particular surface composition). Overall for clusters synthesized in this work the morphology is not the critical factor, but surface composition is the same for all samples, leading to the conclusion that faster degradation of 60NPs is associated with higher Pd content (in this case Pd:Pt 67.5:32.5). That means the electrochemical dissolution proceeds faster due to the surface Pd anodic stripping at potentials as low as 0.8 V⁵³ (the most likely when comparing Pd content in 30NP and 60NP). Regarding catalytic activity in comparison to 45NP, addition,

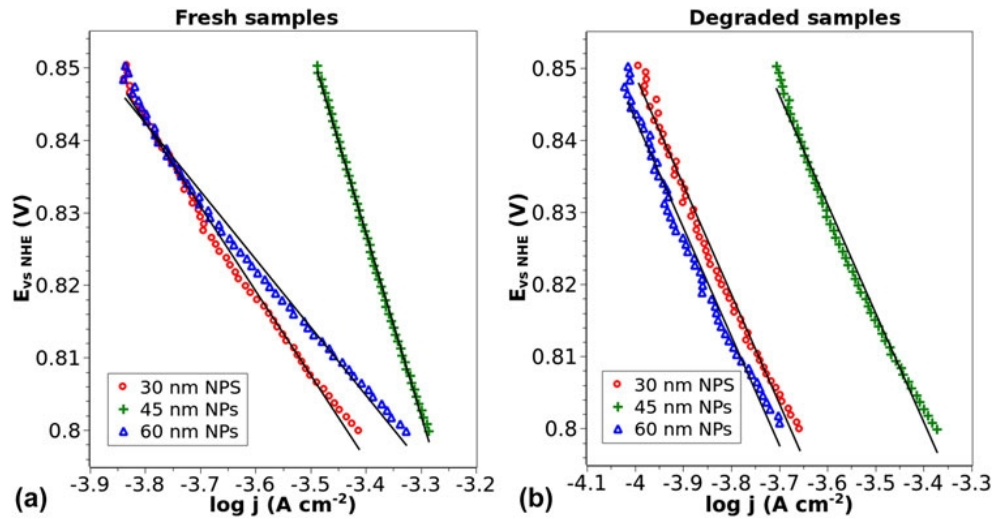
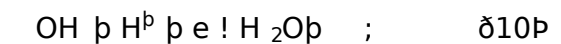
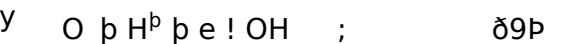
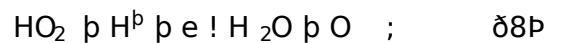
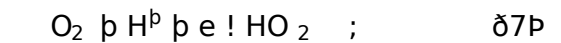
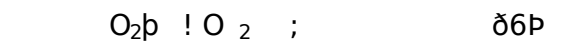


FIG. 4. Tafel plots for 30NP (red), 45NP (green) and 60NP (blue) (a) as-prepared and (b) after degradation.

45NP has the highest initial activity for oxygen reduction, which also indicates on PtPd alloy formation resulting in better ORR kinetics in comparison to pure Pt. This catalytic activity improvement originates from so called an electronic effect and is associated with an electron distribution: Pt atom bears a negative charge while Pd is positively charged in PtPd clusters (electron shift from Pd orbitals to Pt orbitals). As the consequence, the negatively charged Pt atoms in PtPd facilitate the adsorption and dissociation of molecular oxygen on the Pt surface, resulting in faster reduction of atomic oxygen. With respect to the mass activity and the stability achievement for 45NP case, we predict that Pd is fully protected by Pt atoms that block an access of oxidizing species to the catalytic sites of PtPd cluster (as proven by recent theoretical calculation—only two atomic layers on the surface of other metals are necessary to prevent electrochemical leaching out). By selecting a proper atomic-scale particle design, such Pt skin-type cluster will result in an improved oxygen reduction process (due to the Pt-Pd electronic interaction) and better electrochemical stability (from the protective skin). This is presumably the atomic-level structure of 45NPs. This electronic effect due to Pt-Pd alloying in our cluster is particularly noticeable when comparing to the Pt 30 nm particle sizes supported on carbon. This reference system showed slightly higher mass activity at 85 V (i.e., $8.9 \text{ A g}^{-1} \text{ Pt}$)³⁰ however smaller exchange current density ($5.137 \cdot 10^{-4} \text{ A cm}^{-2}$)³⁰ in comparison to PtPd nano-objects generated in this work.

C. Electro-kinetic studies

The electrochemical oxygen reduction is a multi-electron process with a number of elementary steps, involving different reaction intermediates [Eqs. (6)–(10)]. Tafel slope of 120 mV dec⁻¹ in our case, the Tafel



where δ represents the active site on Pt surface. In the study of ORR kinetics, we define and assume that one single step is more sluggish than others, so that controls the rate of overall reaction. In case of ORR, the rate-determining step (RDS) can be a heterogeneous electron transfer. The electrode potential plays a significant role in changing the Pt surface structure in the presence of O_2 at higher potentials ($> 0.8 \text{ V}$); the electrode surface is a mixture of Pt and PtO, while at lower potentials the oxide-free surface is expected. Therefore, the kinetics of O₂ reduction on Pt will not be the same at different potentials.

The ORR exchange current density on a Pt electrode can be obtained by extrapolating the $E \text{ vs } \ln(i)$ plot along the Tafel line to the thermodynamic potential. Tafel slopes give two exchange current densities, the range of high potentials and second at low potentials. The values of the ORR exchange current densities are reported in literature significantly depending primarily on the morphology of the catalyst Pt/PtO surface, the RDS is a pseudo 2-electron process,

gives a Tafel slope of 60 mV dec⁻¹. However, on a pure Pt surface, the first electron transfer is the RDS, resulting in a Tafel slope of 120 mV dec⁻¹.

slope is close to 120 mV dec⁻¹ indicating a rate-limiting interface (represented by straight capacitor) as primary one electron transfer (1e⁻). An initial higher Tafel slope (71.4) for the 45NP suggests some mass transport influence, perhaps due to the surface cleaning/restoration, although this did not affect the observed high mass activity of the fresh catalyst. The Tafel slopes for all samples remain on similar level after the degradation revealing that the mechanism ORR process did not change upon the degradation. More important is the kinetic parameter called exchange current density (j^0) (Table I):

$$E = \frac{1}{4} a + b \log \dot{P} \quad ; \quad \delta_{11P}$$

Regardless the particle size, fresh and degraded 45NP shows the highest value and is also consistent with best mass activity calculated that kinetic regime (at 0.85 V; Table I). This suggests faster electron transfer due to possible alloying in PtPd clusters for 45NP. The activity enhancement that occurs for Pt-based catalysts is explained by the change in electronic structure (increased d-band vacancy) or as the geometric effect (Pt-Pt interatomic distances as it is in PtCu). The populations of d-band vacancies can increase after alloying, generating a strong metal-oxygen interaction, which, in consequence, weakens the O-O bonds. The corresponding kinetic studies of PtFe alloy catalyst show similar trends, although the reported Tafel slopes (120 mV dec⁻¹) were close for both the Pt and PtFe, the exchange current density was much higher for alloyed PtFe system (several orders of magnitude higher).

D. Mass-transport studies by impedance spectroscopy

Electrochemical impedance spectroscopy was extensively applied at the potential where mass transport is predominant (onset potential of ORR peak) and at a rotation speed of 1600 rpm (this ensures the most effective transport of reactant to the electrode surface). Figure 5 represents the theoretical Nyquist diagram where the imaginary component of impedance ($Z_{i\omega}$) is plotted as function of real impedance ($Z_{r\omega}$) together with an electrical equivalent circuit (Lit) and examples of experimental data for the fresh and degraded catalysts (c). The impedance plot composed of high frequency semicircle (beginning of impedance spectrum) corresponding to series of solution resistance for a charge transfer resistance in parallel with nonideal capacitors (CPE element). This arc defines the interfacial resistance of ORR. The linear part of spectrum with a slope of 45° starting at about 50 Ohms indicates mass-transport predominant process at this potential, and, depending on the interplay between diffusion resistance (R_D) values at low frequencies, it will generate the charge accumulation at the electrode-electrolyte

the resemble semicircle associated with the finite diffusion, as shown in Fig. 5. The electrical equivalent circuit presented in Fig. 5(b) was used for the fitting of experimental data (ZView software) and to calculate the numerical values of circuit elements. The model assumes that the electro-active film is a homogeneous structure which the macroscopic boundary between the film and electrolyte plays a central role. In this view, ionic transport is modeled by means of diffusion along the composite bulk (with differentiation of metal and Nafion fractions). The important generalization is that the shape of Nyquist plots of all samples remains either unchanged or is modified at lowest frequency from capacitive loop (straight line at 90°) to finite-length diffusion after degradation test (arc). This simplifies the subtraction of important numerical values of circuit elements for clarity. Figs. 6(a)-6(c) represents admittance spectra of all samples together with fitting plots of admittance configuration kinetics and diffusion processes are graphically separated in comparison with the shape of admittance with modified accordingly). The second part of Figs. 6(d)-6(f) represents a narrow frequency range corresponding to Warburg impedance analyzed to subtract important diffusion parameters. The total impedance defined by Eq.

$$Z_t = \frac{1}{j\omega CPE_{dl}} + R_s + R_{ct} + W_0 \quad ; \quad \delta_{12P}$$

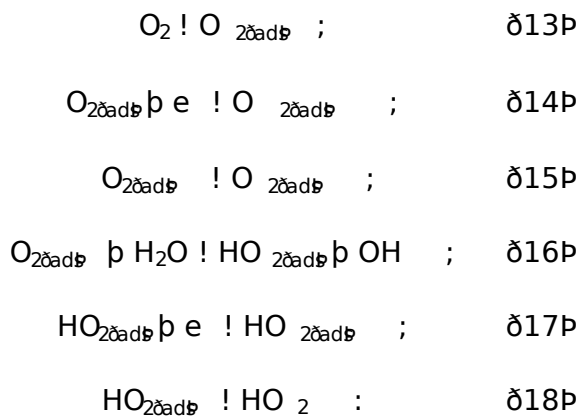
where Z_s is a total impedance, R_s is the solution resistance and can be also estimated graphically as (the left frequency) intercept of semicircle (remains similar for all samples and unchanged after the degradation test), R_{ct} is the charge transfer resistance and corresponds to the radius of semicircle presented in Fig. 6, W_0 is the diffusion (Warburg) resistor, j is the imaginary number, ω is the angular frequency and (CPE) is a nonideal capacitor.

TABLE I. Electrochemical surface area and kinetic parameters: mass activity, exchange current density, and the Tafel slope for 30NP, 45NP, 60NP samples together with the commercial Pt/C baseline.

Sample	ECSA (m ² g ⁻¹)	ORR mass activity at 0.85 V (A ¹ g)	Tafel slope ⁰ (mV dec ⁻¹)	$j^0 \cdot 10^4$ (A cm ²)
Fresh sample				
30NP	16.22	3.18	116.30	3.81
45NP	7.57	4.14	252.60	5.21
60NP	10.70	3.24	93.70	4.71
Pt/C commercial	32.60	2.8
Degraded sample				
30NP	13.05	2.19	151.60	2.21
45NP	11.01	4.55	151.00	4.25
60NP	4.42	2.10	151.10	2.01
Pt/C commercial	26.30	2.30

capacitor of ion accumulation at the electrolyte-electrode interface in total. The numerical values of circuit elements are presented in Table II.

With respect to the catalyst before degradation associated with a rate of oxygen reduction is similar for 30NP and 45NP and bigger for 60NP (this is related to the chemical composition of the metallic clusters). R_{ct} is expected to be smaller for the Pt-rich surface. At measured potential, the diffusion is a RDS and the number of electrons exchanged calculated by Levich equation is close to one [Eq. 1]; calculation provided in support information indicating that reactions 15 and 16 are predominant and the process is fully controlled by the rate of oxygen supply to the electrode surface in a multistep diffusion controlled process:



Accordingly, for the electro-reduction of oxygen expressed as a multistep process using parallel reaction steps (1, 2, ..., 3), the charge transfer rate at each step ($R_{ct,i}$), where i is the number of electrons exchanged and the reaction rate at each step ($\text{mol cm}^{-2} \text{s}^{-1}$).

Based on this assumption, it can be concluded that for the smallest value the number of electrons exchanged (n) should be close to one for the reaction 14 (Table S1, supporting information) the following section the reaction rate constant will be evaluated from the mathematical models of diffusion resistance defined by:

$$W_0^{1/4} R_{ct} \frac{\cot(\delta) \sqrt{s} P}{\delta \sqrt{s} P} ; \quad \delta 19$$

where P is the dimensionless factor representing the time constant associated with the potential-dependent evaluation of intermediates on Pt (in reactions 13-18) the function of the effective diffusion thickness, L , and the effective diffusion coefficient, D , according to:

$$s^{1/4} \frac{L^2}{D} ; \quad \delta 20$$

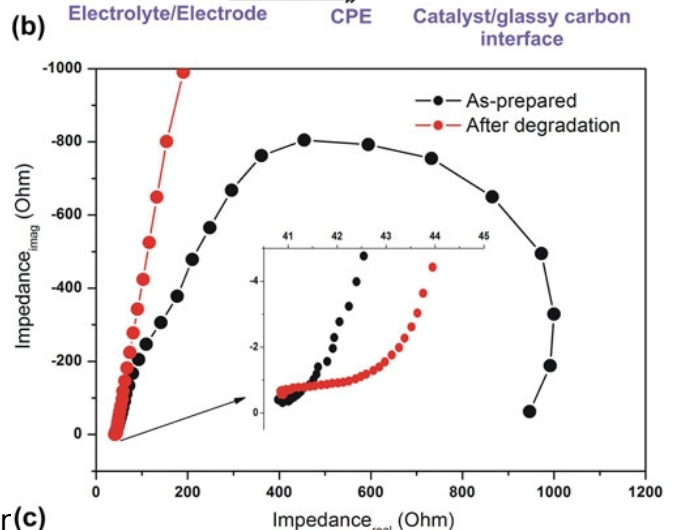
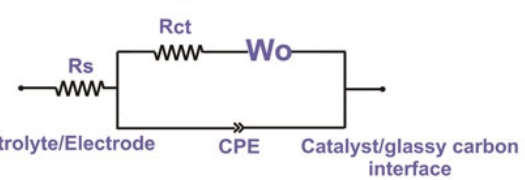
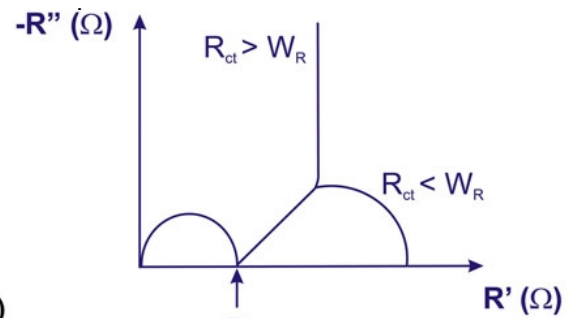


FIG. 5. (a) Theoretical Nyquist plot, (b) electrical equivalent circuit and (c) impedance spectra of fresh (black) and degraded (red) samples recorded at 1600 rpm at 0.508 V.

Thus, τ (inverse coverage relaxation time) is equivalent to the first-order rate constant for the potential-dependent desorption of ORR intermediate. The relevant numerical values of all diffusion parameters are presented in Table S1. With respect to the diffusion resistance W_0-R , all samples showed very similar and small value of the mass transport which are close to the charge transfer resistance, indicating that an accessibility of the reactant to/from the catalytic sites are comparable to other words, the morphological effects such as particle size, shape, and catalysts distribution on carbon support are not critical in this respect. Regarding the relaxation time constant an interesting observation was that for the 45NP the τ was almost one order of magnitude smaller than for other samples (also an effective diffusion thickness). The corresponding rate of surface recovery (τ_s , Table II) changes as follows: higher value of reaction rate constants accomplished for shorter surface relaxation time, indicating that the surface recovery from reaction intermediates is faster.

With correlation to the catalyst morphology, PtPd alloy clusters (although discriminating with the surface roughness (Fig. 1), we observe that respect to ECSA).

45NP is rather compact—this apparently delivers low R_{ct} and τ (regarding the pseudo-capacitance defined as:

ECSA (Table I) in comparison to other catalysts. However even with that the average diffusion thickness for the 45NPs is the smallest, thus the reaction rate

constants the highest and the relaxation time is the shortest. Thus, for 45NPs a stronger electronic effect dimensionless factor, P , 1, in this study in the

on the O_2 adsorption and dissociation from Pt-Pd range of 0.95–0.98, the values are very similar since alloying is expected. In summary from the analysis of diffusion parameters we conclude that the

pseudo-capacitance is directly related to the active surface area (ECSA) and thus to the size of metallic particles. This confirms previous observations that benefits for the 45NPs due to the presence of possible particle size is a critical factor in our study and

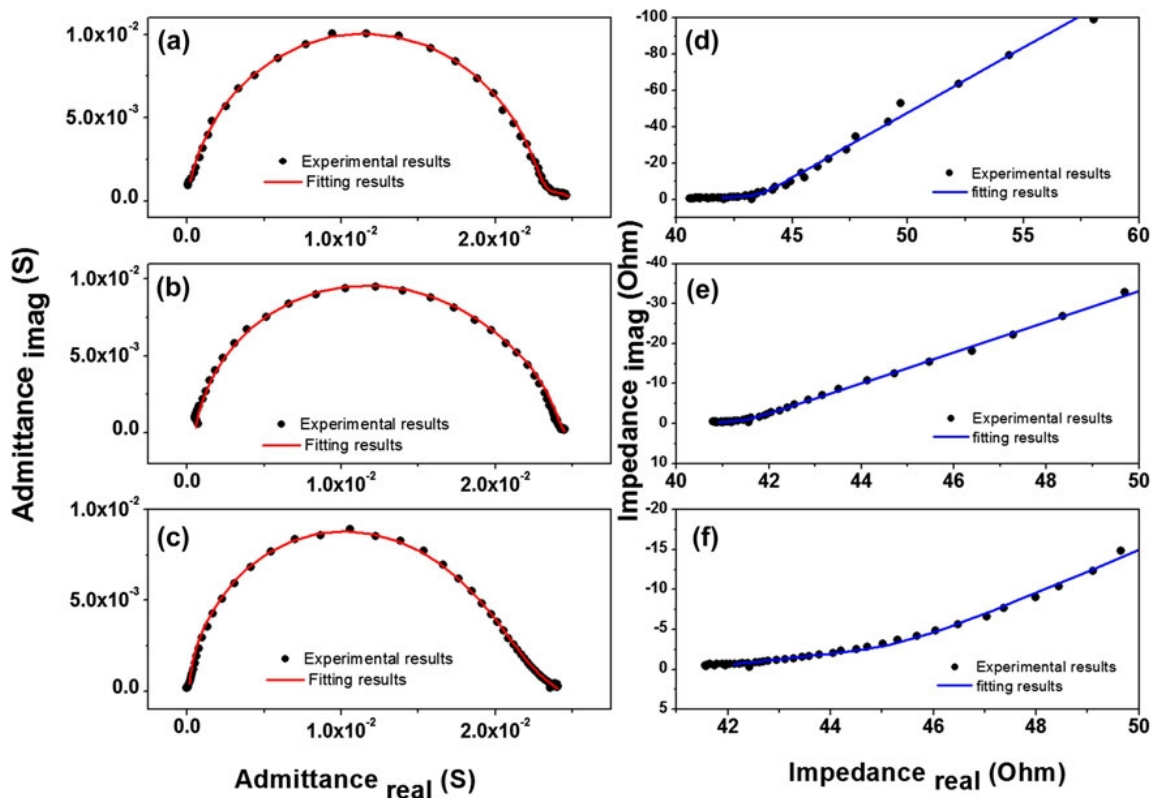


FIG. 6. Admittance spectra (a)–(c) and impedance with Warburg phenomena (d)–(f) recorded at 0.508 V. An experimental data (black scatter) are projected with fitting result (red and blue lines). The 60NP is represented in plots (a) and (d), 30NP (b) and (e) and 45NP (c) and (f).

TABLE II. Electrical equivalent circuit elements obtained from the fitting of spectra in Figs.

Sample	R_{ct} (X)	CPE1-T (/) 10^3	W_0 -R (X)	W_0 -s (s) 10^3	W_0 -P (/)	s^1 (s^1)	L (cm) 10^4
Fresh sample (1600 rpm at 0.508 V)							
30NP	1.86	1.35	2.78	16.1	0.41	62.11	5.88
45NP	2.11	2.63	2.81	1.57	0.42	636.94	1.83
60NP	4.33	4.54	7.34	12.8	0.45	78.12	5.24
Degraded sample (1600 rpm at 0.508 V)							
30NP	1765	1.48	3.99	28.0	0.42	35.71	7.75
45NP	23.32	3.22	5.22	1.72	0.43	581.39	1.92
60NP	2231	1.63	5.10	92.8	0.43	10.77	14.1

complement the analysis of ECSA, which otherwise should be the smallest for sample of 60NPs size (Table I). As the conclusion we observe that regardless the difference in particle size (thus in ECSA), the layer capacitance associated with nonfaradic processes during the electrode polarization is discriminating parameter.

E. Electrochemical degradation

Concerning the degradation processes, several mechanisms are suggested to explain the instability of Pt-based electrocatalysts. This aspect was discussed in detail and supported by theoretical and experimental study. One of the most accepted is the submonolayer dissolution of Pt particles leading to the ECSA loss.⁶⁰ This originates from the formation of Pt-O at the potential range of 0.9–1.2 V and further chemical dissolution of oxidized Pt (also supported by theoretical prediction) is generally acknowledged that the specific ORR activity can be affected by position of PtO reduction peak. When PtO reduction peak is shifted toward positive potential, it means the catalyst binds oxygen species more weakly and thus the specific ORR activity is higher. As observed in Fig. 3 (ORR LSV degraded), the PtO reduction peak for 45NPs appears at more positive potential after degradation, resulting in a stable mass activity and improved ECSA (Table I). This is again correlated with the electronic structure and d-band center of the catalyst surface that controls the adsorption of oxygen species.⁶³ The introduction of Pd can alleviate the oxidation of catalyst, reduce its dissolution and finally improve the durability. There are also other possible explanations, e.g., impact of particle size distribution on the degradation rate.⁶⁴ This correlation states that larger particles are more stable due to Gibbs-Thomson energy,⁶⁴ therefore adding the Pd generates larger PtPd clusters in comparison to pure Pt, but without obvious deterioration of ORR activity. In summary, the 45NPs show the best electrochemical stability under accelerated degradation (and this indicates on some degree of Pt–Pd alloying). This is also confirmed by the stability of impedance parameters before and after degradation test (Table II). For 45NPs, there are almost no changes in R_s and Warburg parameters comparing to other samples that undergo rapid degradation (significant increase) or Pt thus loss of mass activity (Table I).

The CPE-T remains unchanged after accelerated electrochemical degradation, which indicates that morphological changes due to aging can be neglected, although ECSA drops for 30 and 60 nm PtPd catalysts. In summary, for the electrochemical stability the most important factors are the chemical composition of the catalysts surface (more Pt on the surface generally

IV. CONCLUSION

This work aims to synthesize PtPd “nanoflower” structures and to study the effect of particle size, curvature, and possible alloying on the catalytic activity for the electrochemical oxygen reduction, electrochemical stability, the mass-transfer of redox active species toward the catalytic sites, and the electro-kinetics of ORR process. Regarding the ECSA, there is no influence of the cluster size in the range between 30 and 60 nm, but significant influence of curvature and the chemical composition of the catalyst surface. The best electrochemical activity was accomplished by 45 nm nanoflowers, owing to possible alloying that enhances the O₂ adsorption and dissociation via the electro-kinetic studies. The highest exchange current density for oxygen reduction process in this system, indicating on possible PtPd alloying for the 45NP cluster resulting in the complementary process controlled by mass-transport at 0.508 V demonstrated that 45NP has the shortest effective diffusion length and the highest reaction rate constant among all nanologies, leading to the conclusion that the catalyst curvature favors the reactants transport to the catalytic active sites (for a fresh and degraded sample). In addition, the 45 nm-size nanoflower showed superior electrochemical stability that is believed to be the combined effect of alloying and the compactness of its structure. This cluster possesses the Pt-rich surface that protects underlying Pd atoms against leaching out at high potential and at low pH. For the remaining samples, Pd atoms are likely located near the surface, resulting in a rapid Pd dissolution under cathode operation—this stabilizes the entire structure. The charge transfer resistance of the 45NP cluster remains very small after a long term degradation revealing outstanding stability of its catalyst owing to its rigid and active structure with Pt-skin (opposite, increased severally orders of magnitude for 30NP and 60NP in the same degradation regime).

ACKNOWLEDGMENTS

We thank Dr. Stephanie Höppener for EDX mapping and Dr. Igor Perevyazko for his help and an access to a high speed centrifuge. This work was carried out with the financial support of Carl-Zeiss foundation (Germany).

REFERENCES

1. Y. Yoon, R. Rousseau, R. S. Weber, D. Mei, and J.A. Lercher: First-principles study of phenol hydrogenation on Pt and Ni catalysts in aqueous phase. *J. Am. Chem. Soc.* 136, 10287 (2014).
2. G. Sievers, S. Mueller, A. Quade, F. Steffen, S. Jakubith, A. Kruth, and V. Brueser: Mesoporous Pt-Co oxygen reduction reaction (ORR) catalyst for low temperature proton exchange membrane fuel cell synthesized by alternating sputtering. *J. Power Sources* 262, 55 (2014).
3. L. Yi, L. Liu, X. Wang, X. Liu, W. Yi, and X. Wang: Carbon supported Pt-Sn nanoparticles as anode catalysts for direct borohydride-hydrogen peroxide fuel cell: Electrocatalytic and fuel cell performance. *J. Power Sources* 234, 10 (2013).
4. S. Basri, S.K. Kamarudin, W.R.W. Daud, Z. Yaakob, and A.A.H. Kadhum: Novel anode catalyst for direct methanol fuel cells. *Sci. World J.* 2014, 547604 (2014).
5. F. Cheng and J. Chen: Metal-air batteries: From oxygen reduction electrochemistry to cathode catalysts. *Chem. Soc. Rev.* 41, 2172 (2012).
6. J.Y. Lee, D.H. Kwak, Y.W. Lee, S. Lee, and K.W. Park: Synthesis of cubic PtPd alloy nanoparticles as anode electrocatalysts for methanol and formic acid oxidation reactions. *Phys. Chem. Phys.* 17, 8642 (2015).
7. M. Rashid, T.S. Jun, Y. Jung, and Y.S. Kim: Bimetallic core-shell Ag@Pt nanoparticle-decorated MWNT electrodes for amperometric H₂ sensors and direct methanol fuel cells. *Sens. Actuators B* 208, 7 (2015).
8. L. Chen, L. Kuai, and B. Geng: Shell structure-enhanced electrocatalytic performance of Pt core-shell catalyst. *Cryst. Eng. Commun.* 15, 2133 (2013).
9. M. Li, X. Guo, Y. Pan, Y. Liang, Y. Wu, Y. Wen, and H. Yang: Pt/single-stranded DNA/graphene nanocomposite with improved catalytic activity and CO tolerance. *Mater. Chem. A* 3, 10353 (2015).
10. Y. Jia, J. Su, Z. Chen, K. Tan, Q. Chen, Z. Cao, Y. Jiang, Z. Xie, and L. Zheng: Composition-tunable synthesis of Pt-Cu octahedral alloy nanocrystals from PtCu to PtCu₃ via underpotential-deposition-like process and their electro-catalytic properties. *Adv. Sci.* 5, 18153 (2015).
11. M. Nesselberger, B. Ashton, J.C. Meier, I. Katsounaros, K.J.J. Mayrhofer, and M. Arenz: The particle size effect on the oxygen reduction reaction activity of Pt catalysts: Influence of electrolyte and relation to single crystal models. *J. Am. Chem. Soc.* 133, 17428 (2011).
12. M. Xiao, S. Li, X. Zhao, J. Zhu, M. Yin, C. Liu, and W. Xing: Enhanced catalytic performance of composition-tunable Pt-Cu nanoflowers for methanol electrooxidation. *ChemCatChem* 6, 2829 (2014).
13. A. Toge, T. Yokono, M. Saito, H. Daimon, A. Tasaka, and M. Inaba: Oxygen reduction reaction activity of shape controlled Pt catalysts. *ACS Trans.* 1, 2283 (2011).
14. Y. Bing, H. Liu, L. Zhang, D. Ghosh, and J. Zhang: Nano-structured Pt-alloy electrocatalysts for PEM fuel cell oxygen reduction reaction. *Chem. Soc. Rev.* 39, 2184 (2010).
15. B. Fang, B.N. Wanjala, J. Yin, R. Loukrakpan, Luo, X. Hu, J. Last, and C.-J. Zhang: Electrocatalytic performance of Pt-based trimetallic alloy nanoparticle catalysts in proton exchange membrane fuel cells. *J. Hydrogen Energy* 37, 27 (2012).
16. R.D. Adams, B. Captain, W. Fu, J.L. Smith, and M.D. Smith: Addition of platinum and palladium tri-tert-butylphosphine groups to open Pt-Fe and Pt-Ru metal carbonyl clusters. *Organometallics* 23, 389 (2004).
17. Y. Chen, Z. Liang, F. Yang, Y. Liu, and S. Chen: Ni-Pt core-shell nanoparticles as oxygen reduction electrocatalysts: Pt shell coverage. *Phys. Chem. C* 115, 24073 (2011).
18. G. Wang, B. Huang, L. Xiao, Z. Ren, H. Chen, D. Wang, H.D. Abruña, J. Lu, and L. Zhuang: Pt skin on AuCu intermetallic substrate: A strategy to maximize utilization for fuel cells. *J. Am. Chem. Soc.* 136, 9643 (2014).
19. N. Hodnik, M. Bele, and S. Hocevar: New Pt-skin electrocatalysts for oxygen reduction and methanol oxidation reactions. *Electrochem. Commun.* 23, 125 (2012).
20. M. Bele, P. Jovanovi, A. Pavlič, B. Jozinovi, M. Zorko, A. Recnik, E. Chernyshov, S. Hocevar, N. Hodnik, and M. Gaberček: A highly active Pt₃Cu intermetallic core-shell, multilayered Pt-skin carbon embedded electrocatalyst synthesized by a scale-up sol-gel synthesis. *Chem. Commun.* 50, 13124 (2012).
21. W. Li, W. Zhou, H. Li, Z. Zhou, B. Zhou, G. Sun, and Q. Xin: Nano-structured Pt-Fe/C as cathode catalyst for methanol fuel cell. *Electrochim. Acta* 49, 1045 (2004).
22. T. Toda, H. Igarashi, and M. Watanabe: Enhancement of the electrocatalytic activity of Pt-Cu alloy for oxygen reduction on Pt-Falloys. *J. Electroanal. Chem.* 460, 258 (1999).
23. H. Yang, W. Vogel, C. Lamy, and N. Alonso-Vante: Structure and electrocatalytic activity of carbon-supported Pt-Ni alloy nanoparticles toward the oxygen reduction reaction. *J. Phys. Chem. B* 108, 11024 (2004).
24. V.R. Stamenkovic, B. Fowler, B.S. Mun, G. Wang, P.N. Ross, C.A. Lucas, and N.M. Markovic: Improved oxygen reduction activity on Pt(111) via increased surface site availability. *Science* 315, 93 (2007).
25. T.R. Johns, J.R. Gaudet, E.J. Peterson, T. Miller, E.A. Stach, C.H. Kim, M.P. Balogh, and A.K. Datye: Microstructure of bimetallic Pt-Pd catalysts under oxidizing conditions. *ChemCatChem* 5, 636 (2013).
26. C. Lamy: Electrocatalytic oxidation of organic compounds on noble metals in aqueous solution. *Electrochim. Acta* 29, 1581 (1984).
27. J. Yang, J.Y. Lee, Q. Zhang, W. Zhou, and Z. Liu: Carbon-supported pseudo-core-shell Pt nanoparticles for ORR with and without methanol. *Electrochim. Acta* 155, B776 (2008).
28. Z.M. Zhou, Z.G. Shao, X.P. Qin, X.G. Chen, Z.D. Wei, and B.J. Yi: Durability study of Pt-Pd/C as PEMFC cathode catalyst. *Int. J. Hydrogen Energy* 35, 19 (2010).
29. H. Li, G. Sun, N. Li, S. Sun, D. Su, and Q. Xin: Design and preparation of highly active Pt-Pd/C catalysts for the oxygen reduction reaction. *J. Phys. Chem. C* 111, 5605 (2007).
30. K.J.J. Mayrhofer, B.B. Bliznac, M. Arenz, V.R. Stamenkovic, P.N. Ross, and N.M. Markovic: The impact of geometric and surface electronic properties of Pt-catalysts on the particle size effect in electrocatalysis. *J. Phys. Chem. B* 109, 14433 (2005).
31. K.-Y. Chan, J. Ding, J. Ren, S. Cheng, and K.-Y. Tsang: Supported Pt mixed metal nanoparticles as electrocatalysts in low temperature PEMFC. *Mater. Chem.* 14, 505 (2004).
32. S. Eriksson, U. Nylén, S. Rojas, and M. Boutonnet: Preparation of Pt catalysts from microemulsions and their applications in heterogeneous catalysis. *Appl. Catal. A* 265, 207 (2004).
33. E.I. Santiago, L.C. Varanda, and H.M. Villullas: Carbon-supported Pt-Co catalysts prepared by a modified polyol process as cathode for PEM fuel cells. *J. Phys. Chem. B* 11, 13146 (2007).
34. Z. Liu, C. Yu, I.A. Rusakova, D. Huang, and P. Strasser: Synthesis of Pt₃Co alloy nanocatalysts via reverse micelle for oxygen reduction reaction in PEMFC. *Catal.* 49, 241 (2008).
35. A.N. Golik, M. Asgari, and E. Lohrasbi: Study of oxygen reduction reaction kinetics on multi-walled carbon nano-tubes supported Pt-Pd catalysts under various conditions. *Int. J. Hydrogen Energy* 36, 3317 (2011).
36. K.D. Beard, J.W. Van Zee, and J.R. Monnier: Preparation of carbon-supported Pt-Pd electrocatalysts with improved physical properties using electroless deposition. *Appl. Catal. B* 88, 185 (2009).

37. B. Lim, M. Jiang, P.H.C. Camargo, F.C. Cho, J. Tao, X. Lu, Y. Zhu, and Y. Xia: Pd-Pt bimetallic nanodendrites with high activity for oxygen reduction. *Science* 324, 302 (2009).
38. Z. Peng and H. Yang: Synthesis and oxygen reduction electrocatalytic property of Pt-on-Pd bimetallic heteronanostructure. *Am. Chem. Soc.* 131, 7542 (2009).
39. J. Zhang, F.H.B. Lima, M.H. Shao, K. Sasaki, J.X. Wang, J. Hanson, and R.R. Adzic: Platinum monolayer on nonnoble core-shell nanoparticle electrocatalysts. *Electrochim. Acta* 52, 3 (2005).
40. K. Sasaki, J.X. Wang, H. Naohara, N. Marinkovic, K. More, H. Inada, and R.R. Adzic: Recent advances in platinum monolayer electrocatalysts for oxygen reduction reaction: Scale-up synthesis, structure and activity of Pt shells on Pd. *Electrochim. Acta* 55, 2645 (2010).
41. C. He, S. Desai, G. Brown, and S. Bollepalli: PEM fuel cell catalysts: Cost, performance and durability. *Electrochim. Acta* 141 (2005).
42. W. Sheng, S. Chen, E. Vesco, and Y. Shao-Horn: Size influence on the oxygen reduction reaction activity and instability of supported Pt nanoparticles. *J. Electrochem. Soc.* 159, B96 (2011).
43. S. Chen, H.A. Gasteiger, K. Hayakawa, T. Tada, and Y. Shao-Horn: Platinum-alloy cathode catalyst degradation: proton exchange membrane fuel cells: Nanometer-scale compositional and morphological changes. *J. Electrochem. Soc.* 157, A82 (2010).
44. J. Choe, D. Kim, J. Shim, I. Lee, and Y. Tak: Fabrication of a nanosize-Pt-embedded membrane electrode assembly and the utilization of Pt proton exchange membrane fuel cell. *Nanotechnology* 22, 7141 (2011).
45. M.B. Vukmirovic, S.T. Bliznakov, K. Sasaki, J.X. Wang, and R.R. Adzic: Electrodeposition of metals in catalyst synthesis: case of platinum monolayer electrocatalysts. *Electrochim. Acta* 56, 3 (2011).
46. X. Huang, Y. Li, Y. Li, H. Zhou, X. Duan, and Y. Huang: Synthesis of Pt-Pd bimetallic nanocrystals with controllable shape, composition, and their tunable catalytic properties. *Nano Letters* 12, 4265 (2012).
47. H. Zhang, M. Jin, J. Wang, W. Li, P.H.C. Camargo, M.J. Kim, D. Yang, Z. Xie, and Y. Xia: Synthesis of Pd-Pt bimetallic nanocrystals with a concave structure through a bromide galvanic replacement reaction. *Am. Chem. Soc.* 133, 6078 (2011).
48. G. Fu, K. Wu, J. Lin, Y. Tang, Y. Chen, Y. Zhou, and T. Lu: One-pot water-based synthesis of Pd alloy nanoflowers and their superior electrocatalytic activity for the oxygen reduction reaction and remarkable methanol-tolerance in acid media. *J. Phys. Chem. C* 117, 9826 (2013).
49. J.M. Doña Rodríguez, A. Herrera Melián, and J. Pérez Peña: Determination of the real surface area of Pt electrodes by hydrogen adsorption using cyclic voltammetry. *J. Chem. Educ.* 77, 1395 (2000).
50. A. Ignaszak, C. Song, W. Zhu, J. Zhang, A. Bauer, R. Baker, V. Neburchilov, S. Ye, and S. Campbell: Titanium carbide and its core-shelled derivative TiC@TiC catalyst supports for proton exchange membrane fuel cells. *Electrochim. Acta* 69, 587 (2012).
51. R.D. Vengrenovich, B.V. Ivanskii, I.I. Panko, S.V. Yarema, V.I. Kryvetskiy, and M.O. Stasyk: Ostwald ripening of the platinum nanoparticles in the framework of modified LSW theory. *Nanomaterials* 4, 1584 (2014).
52. S.K. Ahluwalia, S. Arisetty, J-K. Peng, R. Subbaraman, X. Wang, N. Kariuki, D.J. Myers, R. Mukundan, R. Borup, and O. Polevaya: Dynamics of particle growth and electrochemical surface area due to platinum dissolution. *Electrochim. Acta* 161, F291 (2014).
53. X. Ye, Q. Yang, Y. Wang, and N. Li: Electrochemical behavior of gold, silver, platinum and palladium on the glassy carbon electrode modified by chitosan and its application. *Talanta* 47, 1199 (1998).
54. D. Li, C. Wang, D.S. Strmcnik, D.V. Tripkovic, X. Sun, Y. Kang, M. Chi, J.D. Snyder, D. van der Vliet, Y. Tsai, V.R. Stamenkovic, S. Sun, and N.M. Markovic: Functional links between single crystal morphology and nanoparticle size with different shape: The oxygen reduction reaction. *Energy Environ. Sci.* 7, 4061 (2014).
55. M.C.S. Escañó and H. Kasai: First-principles study on surface structure, thickness and composition dependence of the stable Pt-skin/PtCo oxygen-reduction-reaction catalysts. *J. Power Sources* 247, 562 (2014).
56. C. Song and J. Zhang: *Electrocatalytic Oxygen Reduction Reaction in PEM Fuel Cell Electrocatalysts and Catalysts*, J. Zhang ed.; Springer: London, 2008; p89.
57. J. Wang, C. Wang, J. Wang, S. Miao, M. Wei, F. Yang, L. Yu, and X. Bao: Architecture of Fe/C catalyst with high activity and durability for oxygen reduction reaction. *Nano Res.* 7, 1519 (2014).
58. J. Otomo, X. Li, T. Kobayashi, C. Wen, H. Nagamoto, and H. Takahashi: AC-impedance spectroscopy of catalytic reactions with adsorbed intermediates: Electro-oxidations of 2-propanol on carbon-supported catalyst. *Electrochim. Acta* 53, 573,99 (2004).
59. C. Gabrielli, M. Keddad, N. Portail, P. Rousseau, H. Takenouti, and J. Vivier: Electrochemical impedance spectroscopy investigations of a microelectrode behavior in a thin-layer cell: Experimental and theoretical studies. *J. Phys. Chem. B* 110, 20478 (2006).
60. Y. Shao-Horn, W.C. Sheng, S. Chen, P.J. Ferreira, E.F. Holby, and D. Morgan: Instability of supported platinum nanoparticles in low-temperature fuel cells. *Catal.* 46, 285 (2007).
61. R.M. Darling and J. Meyers: Mathematical model of platinum movement in PEM fuel cells. *J. Electrochem. Soc.* 152, A242 (2005).
62. H.A. Gasteiger, S.S. Kocha, B. Sompalli, and F.T. Wagner: Activity benchmarks and requirements for Pt, Pt-alloy, and non-Pt oxygen reduction catalysts for PEMFCs. *Catal.* 46, 3009 (2005).
63. M. Liu, J. Zhang, and R. Adzic: Origin of enhanced activity in palladium alloy electrocatalysts for oxygen reduction reaction. *J. Phys. Chem. B* 111, 6772 (2007).
64. E.F. Holby, W. Sheng, Y. Shao-Horn, and D. Morgan: Pt nanoparticle stability in PEM fuel cells: Influence of particle size distribution on crossover hydrogen. *Energy Environ. Sci.* 2, 865 (2009).

Supplementary Material

To view supplementary material for this article, visit <http://dx.doi.org/jmr.2015.212>.

--- Supplementary Information ---

Pt-Pd catalytic nanoflowers: synthesis, characterization and the activity toward electrochemical oxygen reduction.

Simon Tymen, Andreas Undisz, Markus Rettenmayr, Anna Ignaszak

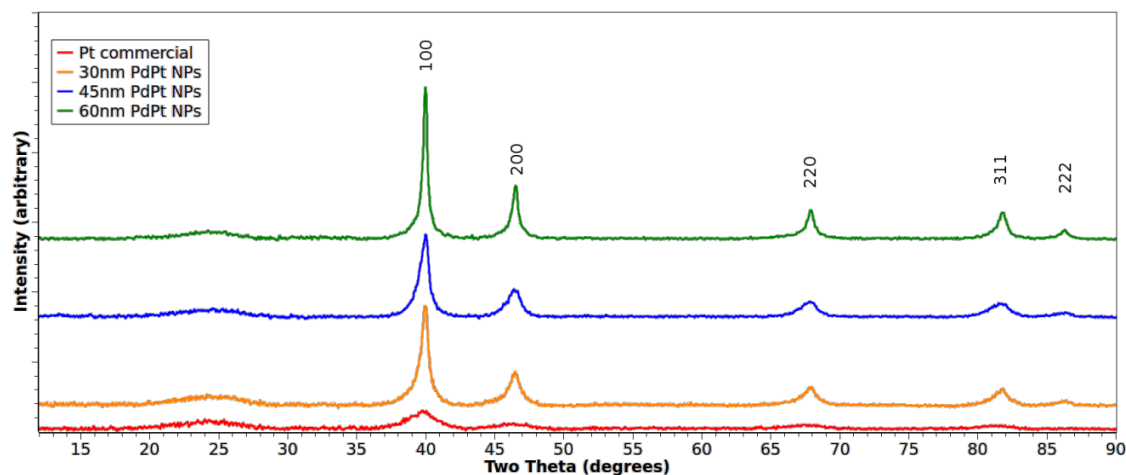


Fig. S1 XRD patterns of Pt/C commercial catalysts and 30NP, 45NP and 60 NP supported on carbon.

Table S1. Lattice constant calculated for the face-centered cubic structure of PtPd clusters.

Sample	Lattice constant (Å)
Pt reference	3.920
Pd reference	3.890
Pt/C	3.917
30NP	3.907
45NP	3.908
60NP	3.904

The number of electrons exchanged in mass-transport limited potential range (0.508 V) was calculated according to Levich equation of the diffusion current dependence on the rotation speed:

$$i_d = 0.602 \cdot n \cdot F \cdot A \cdot c_{O_2} \cdot (D_{O_2})^{2/3} \cdot \gamma^{-1/6} \cdot \omega^{1/2}$$

Where i_d is the diffusion current (or Levich current) (A), n is the number of electrons, F is the Faraday constant (96485.34 C mol⁻¹), A denotes to the area of the RDE (0.1963 cm²), c_{O_2} is the concentration of oxygen in electrolyte (1.146.10⁻⁶ mol cm⁻³), D oxygen diffusion coefficient in 0.1 M HClO₄ (1.930.10⁻⁵ cm² s⁻¹), γ is viscosity of electrolyte (1.01*10⁻² cm² s⁻¹), ω RDE rotational speed (1600 rpm or 167.55 rad s⁻¹), values according to [S1].

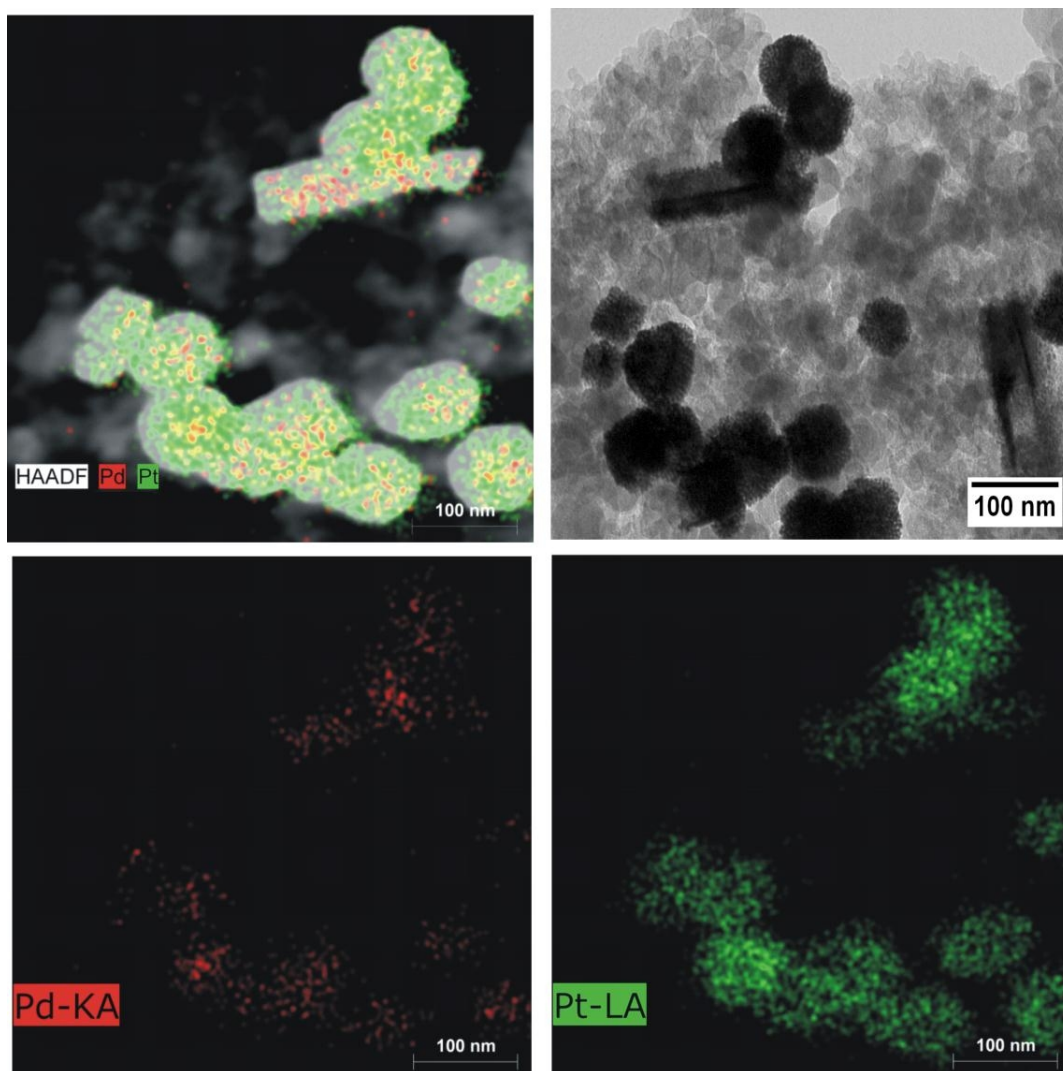


Fig. S2. Spot-resolved EDX mapping of catalytic nanoflowers (example 45NP): Pt and Pd mapping (left top) and a relevant TEM image (right top); bottom images represent distribution of individual Pt and Pd atoms in this sample.

Table S2. Mass transfer-controlled current and number of electrons exchanged at 0.508 V.

Sample	$i_d \times 10^{-4}$ (A)	n (/)
30NP (as-prepared)	-3.38	1.17
45NP (as-prepared)	-2.61	0.91
60NP (as-prepared)	-2.84	0.99
30NP (degraded)	-2.53	0.88
45NP (degraded)	-2.52	0.87
60NP (degraded)	-2.44	0.85

[S1] Hong JW, Kang SW, Choi B-S, Kim D, Lee SB, Han SW. Controlled Synthesis of Pd–Pt Alloy Hollow Nanostructures with Enhanced Catalytic Activities for Oxygen Reduction. *ACS Nano*. 2012 Mar 27;6(3):2410-9.

Publication 2

From cubic palladium to concave core-shell platinum palladium nanoparticles:
Evolution of the structure and their electrochemical properties

S. Tymen, A. C. Scheinost, M. J. Lozano-Rodriguez, C. Friebe,
U. S. Schubert

J. Electrochem. Soc. **2018**, 165 (3) H67-H77. DOI: 10.1149/2.0021803jes.

Reproduced by the permission of the ECS – The Electrochemical Society.



From Cubic Palladium to Concave Core-Shell Platinum Palladium Nanoparticles: Evolution of the Structure and Their Electrochemical Properties

Simon Tymen,^{1,z} Andreas C. Scheinost,^{2,3} M. Janeth Lozano-Rodriguez,^{2,3} Christian Friebe,^{1,4} and Ulrich S. Schubert^{1,4}

¹Laboratory of Organic and Macromolecular Chemistry (IOMC), Friedrich Schiller University, 07743 Jena, Germany

²The Rossendorf beamline, European Synchrotron Radiation Facility (ESRF), 38043 Grenoble, France

³Molecular Structure Division, Institute of Radiochemistry, Helmholtz Zentrum Dresden-Rossendorf, 01328 Dresden, Germany

⁴Center for Energy and Environmental Chemistry Jena (CEEC Jena), 07743 Jena, Germany

The PtPd nanoparticles are synthesized following different methods and intensively investigated for their catalytic properties oxygen reduction reaction (ORR), with a potential application in fuel cells. The galvanic replacement is an attractive method to prepare bimetallic particles with high catalytic activity and a high control of the morphology and chemical composition, varying with the experimental conditions during the synthesis. The influence of the time with the transformation from pure Pd nanocubes to concave core-shell PtPd nanoparticles synthesized by galvanic replacement is examined: after different times of preparation, the morphology of the particles was monitored by transmission electron microscopy (TEM) coupled with energy Dispersive X-ray spectroscopy (EDS). Via X-Ray diffraction spectroscopy (XRD), the crystallographic structure and the variation of size, lattice parameters, *d*-spacing, and composition were determined. The extended X-ray fine structure (EXAFS) measurements show the formation of a PtPd alloy at the surface of the particles for all samples. Finally, the electrochemical determination of the catalytic activity and stability tests revealed two different particle types as candidates to replace pure Pt as catalyst in the proton exchange membrane fuel cells (PEMFC) due to their enhanced stability, higher catalytic activity, and lower Pt content.

© 2018 The Electrochemical Society. [DOI: 10.1149/2.0021803jes]

Manuscript submitted August 28, 2017; revised manuscript received January 25, 2018. Published February 8, 2018.

Today, the problems of climate change and the environmental pollution necessitate the replacement of fossil fuels by means of new energy sources and sustainable technologies. In this regard, proton exchange membrane fuel cells (PEMFCs) with their high efficiencies at ambient temperature represent highly promising alternatives. One of the main chemical reactions in PEMFCs, the oxygen reduction reaction (ORR), depends strongly on the usage of suitable catalysts and, thus, many researchers are working on the development of new materials with a higher catalytic activity for the ORR. Unfortunately, most of the catalysts are based on platinum, a transition metal that does not occur abundantly and is, hence, too expensive for a large scale utilization. Different approaches are tested aiming at the reduction of the cost of the cells and the improvement of their performances. The diminution of the amount of platinum via bimetallic catalysts (core-shell, alloys, . . .)^{1,2} and nanostructured materials with different shapes and sizes of particles^{3,4} is an essential step to succeed. Different techniques exist to prepare the catalysts with one or more components, like nickel,⁵ copper,⁶ and iron⁷ to obtain particles and study their catalytic activity. During our work on platinum and palladium core-shell nanoparticles (NPs), we followed the evolution of the structure via transmission electron microscopy (TEM) coupled with energy Dispersive X-ray spectroscopy (EDS) observations and extended X-ray fine structure (EXAFS) measurements and confirmed the results via X-Ray diffraction spectroscopy (XRD) after different times of synthesis. Cyclic voltammetry (CV) and linear sweep voltammetry (LSV) permit the calculation of the electrochemically active surface area (ECSA) and the catalytic activity for ORR. After Tafel and Koutecký-Levich analysis, the electrochemical properties of the particles (catalytic activity, kinetic, stability) are compared trying to link the structure and the physical properties of the particles to their performances. The electrochemical impedance spectroscopy (EIS) experiments complete the particles characterization. With all these information, high performance and stable bimetallic core-shell PtPd nanoparticles are prepared by galvanic replacement. Furthermore, in-situ XAFS measurements are carried out to study the formation of oxides on the surface of the electrode during the oxygen reduction reaction. Our experiments were based on in-situ XAFS measurement at different potentials and, via the Fourier-transformed EXAFS spectra, we observed an evolution

of the particles (with and without oxide). With the iterative transfer factor analysis (IFTA), we followed the relative concentration of the oxide at different potentials.⁸

Method

Synthesis of PtPd nanoparticles.—Depending on the particle's type, size, shape, and composition, different methods were used to synthesize PtPd nanoparticles (NPs) in aqueous or organic solution.^{9–11} Inspired by the method of Zhang et al., using galvanic replacement for the synthesis of bimetallic core-shell nanoparticles¹² or PtPd alloy nanocages,¹³ the hexachloroplatinic acid (H₂PtCl₆) was replaced by potassium tetrachloroplatinate (K₂PtCl₄), Sigma Aldrich, 98%), which possesses platinum(II) instead of platinum(IV). The particles were prepared in two steps by galvanic replacement: Firstly the synthesis of cubic Pd nanoparticles, followed by the preparation of the core (Pd)-shell (Pt) nanoparticles. The synthesis of the Pd NPs was performed in aqueous solution: 0.6 g of ascorbic acid (AA, Sigma Aldrich, 98%), 3 g of potassium bromide (KBr, Sigma Aldrich, 99%), 1.85 g of potassium chloride (KCl, Sigma Aldrich, 99%), and 1.05 g of poly(vinylpyrrolidone) (PVP, Alfa Aesar, 98%) were added to 80 mL of distilled water. The solution was sonicated for 2 min and heated to 80 °C. After 10 min, 30 mL of sodium tetrachloropalladate (Na₂PtCl₄, 6.5 × 10⁻² mol L⁻¹, Sigma Aldrich, 98%) were added with a syringe (1 mL min⁻¹). Afterward, the solution was maintained at 80 °C under magnetic stirring for 3.5 h. The PtPd NPs were prepared in a second step: 10 mL of the solution containing Pd nanoparticles were mixed with 70 mL of an aqueous solution composed of 3 g of KBr and 0.333 g of PVP. The solution was heated to 90 °C and 30 mL of K₂PtCl₄ (3 × 10⁻³ mol L⁻¹, Sigma Aldrich, 98%) were added (1 mL min⁻¹) under magnetic stirring. Different times of synthesis were used to study the evolution of the particles: 0.6 h, 2 h, 4 h, 6 h, 8 h, and 17 h. After the synthesis, the particles, collected by centrifugation, were washed and rinsed several times with water and ethanol. Afterwards, the solution containing clean particles was dried in the oven at 70 °C.

Coating the particles on carbon powder.—For a sample, composed of 40% particles and 60% of carbon, 40 mg of particles were added to 25 mL of ethylene glycol (VWR), and the mixture was sonicated for 15 min. A mixture of 60 mg of Vulcan XC-72R carbon powder in 25 mL of ethylene glycol at pH 2 (adjusted with

^zE-mail: simon.tymen@uni-jena.de

nitric acid solution, 2 mol L⁻¹, Sigma Aldrich, 70%, purified by re-distillation) was sonicated for 30 min. After sonication, both mixtures were merged, sonicated for 1 h and stirred for one night with a magnetic stirrer. Afterwards, the mixture was heated to 40°C and filtrated. The resulting particles were collected by microfiltration and dried for 5 h at 70 °C in an oven. The analogous method was used for all the particles.

TEM-EDS characterization.—The nanoparticles were characterized with a high-resolution transmission electron microscope (HR-TEM) JEOL JEM-3010 operating at 300 keV and equipped with an X-Ray analyzer Oxford. Before the experiments, the aqueous solution containing the nanoparticles was homogenized by sonication and dispersed on a TEM grid (copper covered by a carbon film). The sample was subsequently dried under vacuum before the introduction in the main chamber of the TEM.

EXAFS measurements.—The Pt-L_{III} and Pd-K edges EXAFS measurements were performed at the Rossendorf Beamline (BM20A) at the European Synchrotron X-Ray Facility (ESRF, Grenoble, France). The synchrotron beam was monochromatized using a water-cooled Si(111) double-crystal monochromator (DCM). A first, 1.4 m long, Pt-coated, meridionally bent Si mirror was used before the DCM for collimation, and a second, 1.3 m long, Pt-coated, toroidal Si mirror after the DCM was used for vertical and horizontal focusing. The rejection of higher harmonics of the complete setup is better than 10⁻⁴. The measurements were done at room temperature, either in transmission or fluorescence mode, using ionization chambers and a 13 elements high-purity Ge detector (Canberra) with a digital spectrometer (XIA X-Map). Before measurements, the particles coated on carbon (40 wt% particles) were compressed to form pellets (1 g) with addition of boron nitride powder (BN, Sigma Aldrich, 98%) for a better stability. Energy calibration, averaging of several scans, and dead-time correction of fluorescence signals were done with the software SixPack.¹⁴ Subsequent data reduction steps were performed with the WinXAS software.¹⁵ The spectra were normalized using a first-order polynomial function fitted through the pre-edge region, and a second order polynomial function fitted through the post-edge region. Spectra were then converted from energy into photoelectrons kinetic energy units (k-space) by arbitrarily assigning the first inflexion point of the absorption edge to zero energy. The EXAFS oscillations were extracted by a spline fit to the post-edge region using the auto-spline algorithm of WinXAS. The such-obtained EXAFS functions were k³-weighted and then Fourier-transformed to R-space using a Bessel window function across a k range of 2 to 15 Å⁻¹. Theoretical phase shift and amplitude functions for the shell fits were calculated with FEFF 8.2¹⁶ based on Pt, PtPd, and Pd metal clusters with a face-centered cubic (fcc) crystallographic structure. The shell fit was then performed with WinXAS to derive coordination numbers (CN), interatomic distances (R), Debye-Waller factors (σ²), and phase shift correction (E₀). The amplitude reduction factor (S₀²) was fixed at 0.8, and the spectra were fitted in R-space (R range of 1.7 to 3 Å).

X-Ray diffraction.—The XRD experiments were done using a Rigaku Miniflex600 diffractometer equipped with an energy dispersive D/teX Ultra silicon strip detector. For XRD measures, Cu-K_{α1} radiation (wavelength: 1.54184 Å) was used at 40 kV and 15 mA. The scanning range (2θ) was from 30 to 90° with a scan rate of 1° min⁻¹ and an interval of 0.02°. Before characterization, about 30 mg of catalyst powder was pressed to obtain a homogeneous distribution in the sample holder. The determination of the composition of the particles (Pd and Pt molar fraction) was done with Pt, Pd, and PtPd fcc crystalline structures coming from the Crystallography Open Database (COD)¹⁷ with the software MAUD.¹⁸

Electrochemical measurements.—For all the measurements, a potentiostat (Princeton Applied Research VersaStat MC) with a standard three electrodes configuration was used with a glassy carbon rotational

disk electrode (RDE, Princeton Applied Research, model 636A, geometric area of 0.1963 cm²) as the working electrode, a Hg/Hg₂SO₄ electrode as the reference electrode, and a platinum wire as counter electrode. The electrochemical studies were carried out in 70 mL of HClO₄ (1 × 10⁻¹ mol L⁻¹) electrolytic solution made from 18 M microfiltrated water. Before experiments, the RDE was polished and rinsed with high purity water. All potentials are given versus the Standard Hydrogen Electrode (SHE).

The different nanoparticles were characterized in the form of an ink made by dissolution of 9 mg of PtPd/C catalyst powder in a mixture of 0.25 mL of water and 2.25 mL of isopropyl alcohol (IPA, Merck, 99.5%). After 15 min of sonication, 12 μL of the ink are deposited on the RDE glassy carbon support (3 × 4 μL) and the film was protected by the deposition of 7 μL of Nafion (perfluorinated resin solution, 5 wt%, Sigma Aldrich) diluted in methanol (1:100). After deposition, the fresh film was electrochemically cleaned by CV, 60 cycles from 0.050 to 1.200 V at 0.100 V s⁻¹. The determination of the ECSA was done with the same method in the same potential range at a scan rate of 0.020 V s⁻¹ with the electrolyte saturated with N₂. After the ECSA determination, the ORR test and the EIS experiments were conducted in an HClO₄ (1 × 10⁻¹ mol L⁻¹) O₂-saturated solution. The EIS was measured at a DC potential of 0.5 V, applying AC frequencies from 1 × 10⁵ to 5 × 10⁻² Hz and with an amplitude of 0.010V, as well as an RDE rotation velocity of 1600 rpm. The number of electrons exchanged was determined via the Koutecký-Levich analysis, with measurement at different rotational speed, from 100 to 2500 rpm, and the catalytic activity was calculated after measurements by LSV within a potential range from 0.3 to 1.2 V under rotation (1600 rpm) at 0.005 V s⁻¹. All electrochemical experiments were done at 25°C.

Results and Discussion

Characterization of the PtPd nanoparticles by TEM and EDS.—The PtPd nanoparticles were prepared using the galvanic replacement method, and the evolution of their structures was studied after different times of synthesis. The TEM-EDS investigations permitted the analysis of the structure of the NPs (size, shape, repartition, and composition) without modification of the samples (the particles were directly deposited on a TEM grid). The TEM observations revealed a progressive evolution of the NPs with the time of synthesis (Figure 1), with a particle size of around 20 nm for all the samples.

Before the galvanic replacement and the addition of Pt, pure Pd NPs with a well-defined cubic shape and an average size of 18 nm (without aggregates) were visible. Through the addition of a Pt solution, the formation of PtPd NPs via galvanic replacement and co-deposition of Pt was initiated. For the particles prepared within 0.6 h, a thin layer of Pt (confirmed by EDS) appeared on the surface of the particles (Figure 2). The Pt film formation started at the corners of the Pd cubes and the thickness of the Pt shell increased to form a layer of Pt over the Pd core. The concavity of the NPs and the thickness of the Pt layer increased with the time of synthesis. After 4 h, the particles are really concave, including the Pd core.

There were no significant variations of the size of the particles with the time of synthesis. No aggregates were visible and the shape of the particles was homogeneous (except for some samples where some core-shell nanoparticles with a flower structure were visible after 6 h and 8 h of synthesis). The EDS confirmed that the particles are composed of Pt, Pd and small quantities of Br. The presence of bromine in the spectra was due to an incomplete galvanic replacement, i.e. the bromide was not completely replaced by the Pt. An evolution of the amounts of Pt and Pd with the time of synthesis was observable (Table I): The ratio of Pt increased until 4 h and decreased for the particles synthesized in 6 h, with 22 wt% of Pt. After 8 h, there was again an augmentation (26 wt% of Pt) and, finally, for the particles synthesized in 17 h, the ratio of Pt was equivalent to the 4 h particles (35 wt%).

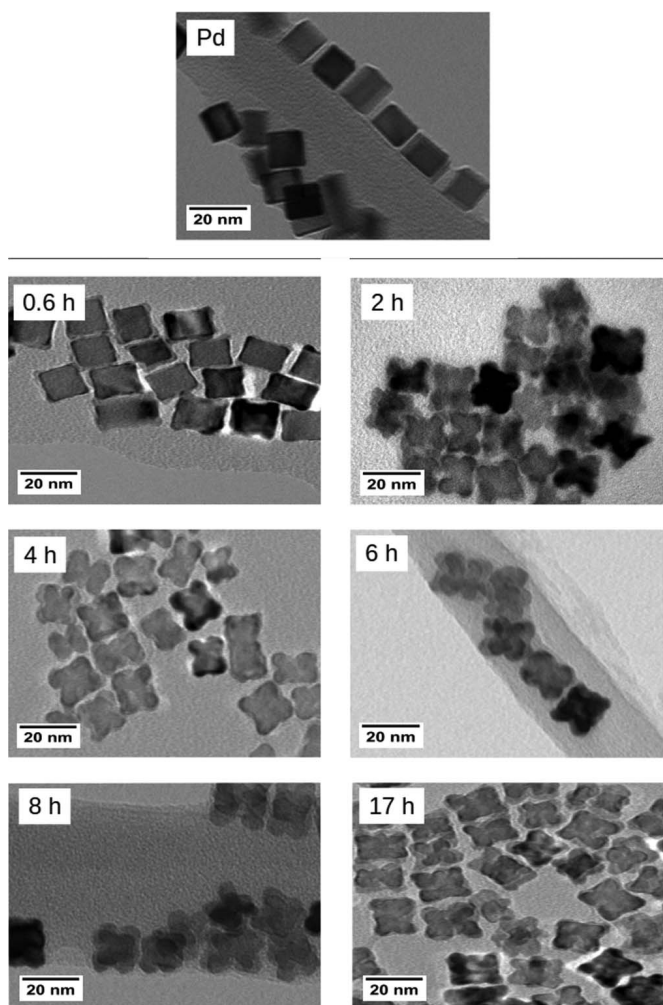


Figure 1. Evolution of the nanoparticles structure followed by TEM: Pure Pd nanocubes (up) and PtPd nanoparticles with different times of synthesis (down).

XRD analysis.—On the XRD spectra (Figure 3), the main characteristic peaks of the *fcc* Pt and Pd crystals, corresponding to the planes (111), (200), (220), and (311) are visible, confirming a *fcc* crystalline structure composed of Pd and Pt atoms for all the particles. XRD patterns for the different particles are similar, which denotes analogous bulk compositions and no peaks that correspond to Pt or Pd oxides are observable.

After the normalization of the spectra with respect to the intensity of the well-defined (111)-based peak, the inter-planar distances d were

calculated using the Bragg's law:

$$2 \cdot d \cdot \sin \theta = n \cdot \lambda \quad [1]$$

where n is the integer factor, θ is the Bragg's angle (degrees), and λ is the wavelength of the X-rays, (Cu- $K_{\alpha 1}$ radiation, 1.54184 Å). The average size of the particles, τ , was calculated from the widths of the (220) diffraction peaks on the spectra via Scherrer's equation, which is valid for nanometric objects:

$$\tau = \frac{K \cdot \lambda}{\beta \cdot \cos \theta} \quad [2]$$

K is a shape factor (between 0.9 and 1.0, here 0.94, considering an *fcc* isotropic structure), λ is the wavelength of the X-rays, β (radians) the FWHM, and θ the Bragg's angle (degrees) of the peak selected to calculate the particles size. To obtain an estimation of the quantity of Pt and Pd in the particles and to compare these values to the results coming from the EDS measurements, Vegard's law was applied. This was possible considering the system as a mixture of two components, a solid solution, with pure Pt and Pd before the mixing and the same structure (*fcc*) and temperatures.

So, the composition of the mixture is approximately determined by the equation:

$$a_{Pt,(1-x),Pd,x} = (1-x) \cdot a_{Pt} + x \cdot a_{Pd} \quad [3]$$

with x as the molar fraction of Pd in the particles.

The lattice parameters of the solid solution $a_{(Pt(1-x)Pd_x)}$, were measured by XRD, and the theoretical values of the lattice parameters of Pt, a_{Pt} , and Pd, a_{Pd} , with a *fcc* crystalline structure came from the COD, 3.923 Å and 3.891 Å, respectively. After the analysis of the spectra, the evolution of the lattice parameters for the different samples was studied (Table I).

For the commercial Pt and the Pd spectra, the same diffraction profile as for a standard material appears, with lattice parameters of 3.894 Å for the Pd and 3.913 Å for the Pt, which deviates negligibly from the theoretical ones due to inhomogeneities. For the particles, the lattice parameters and the *d-spacing* values (the interatomic distance between the planes of the crystal) are between those of pure Pd and pure Pt. These two parameters evolved in accordance with the ratio of Pt in the particles (measured by EDS): the Pt-rich particles feature higher lattice parameters and *d-spacing* values, corresponding to the expansion of the crystalline structure with the replacement of Pd atoms by Pt.

The different sizes of particles found by application of Scherrer equation (Eq. 2) were comparable to the sizes estimated from the TEM images with the software Image J. With the progression of the times of synthesis, the particle size decreased from 20 nm for the Pd nanocubes and the Pd-Pt 0.6 h core-shell nanoparticles to 13.4 nm after 6 h. For longer times, the size increased again to 16 nm. The first step of the evolution of the chemical composition of the particles, determined using Vegard's law and the weight fraction measured by EDS, was similar, featuring an increasing Pt ratio for 4 h (35 wt%

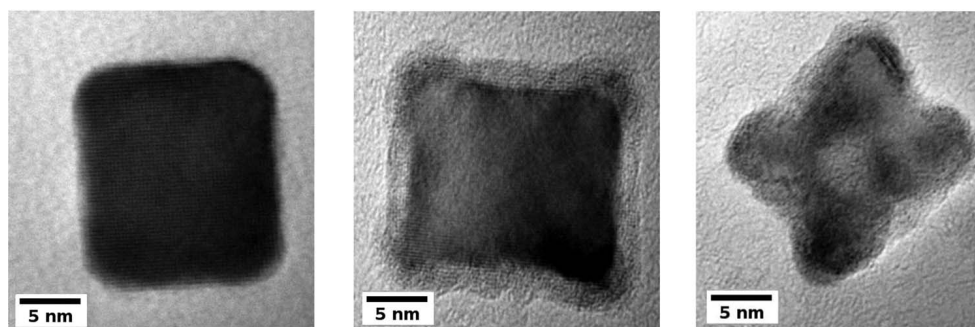


Figure 2. TEM observations of Pd nanocubes (left), the formation of a thin layer in the surface of the nanocubes for the particles synthesized in 0.6 h (middle) and the apparition of a concave structure for the particles synthesized in 4 h (right).

Table I. Summary of the results from the XRD measurements and composition of the particles (Pd and PtPd samples) measured by EDS (error 10%).

Sample	Lattice parameter (Å)	<i>d</i> -spacing (Å)	Size (nm) (XRD)	Pd molar fraction (%) (XRD)	Size (nm) (TEM)	Pd weight (wt%) (EDS)	Pt weight (wt%) (EDS)	Pd molar fraction (%) (EDS)
Pd	3.891	2.2468	19.24	100	16.1	100	0	100
PtPd 0.6 h	3.892	2.2471	20.03	94	17.2	91	9	96
PtPd 2 h	3.894	2.2482	15.53	88	16.2	81	19	87
PtPd 4 h	3.900	2.2517	14.39	70	14.6	65	35	70
PtPd 6 h	3.897	2.2496	13.43	78	14.7	78	22	80
PtPd 8 h	3.893	2.2479	16.74	91	16.4	74	26	80
PtPd 17 h	3.896	2.2498	16.06	82	15.7	65	35	71

Pt), followed by a diminution of the Pt content after 6 h. Afterwards, XRD experimental results indicate a further decreasing Pt content (8 h), which rises again for the 17 h samples. In contrast, according to EDS, the Pt content is continuously increasing from 6 h to 17 h. These differences probably come from derivations of the law, which were already observed by other researchers working on alloys.^{20,21}

EXAFS measurements.—The EXAFS measurements at Pt-L_{III} for the different PtPd nanoparticles coated on carbon were compared to pure Pt foil and Pt/C commercial sample, to see the differences between pure Pt and the particles. The Fourier-transformed spectra are presented in Figure 4. The data collected at the Pt-L_{III} edge showed a well-defined double peak between 2 and 3 Å (uncorrected phase shift) for all the PtPd nanoparticles.

The FEFF modeling using clusters with different ratios of Pd and Pt revealed that this double peak arises from the presence of both Pt and Pd neighbors in a (nearly) equal proportion within the first shell. By comparison, the commercial Pt showed only one peak as expected from the exclusive presence of Pt neighbors.

At the Pd-K edge, the main strong peak in the Fourier-transformed spectra at $R = 2.74$ Å suggests the predominance of only one type of neighbors (Figure 4), most likely the Pd, which was confirmed by the shell fit of the data (Tables II and III). As shown by the Pt-Pt and Pt-Pd data, Pt is surrounded by both Pt and Pd neighbors at distances of 2.72 to 2.74 Å, which is in line with the crystallographic value of 2.74 Å.²² The sum of both Pt-Pt and Pt-Pd CNs is close to 12, considering the relatively high error of 25%, coming from the FEFF model used to fit the spectra and the error of fitting, and the

Pd:Pt ratio is slightly above 1. Relatively small Debye-Waller factors indicate a small static and vibrational disorder. All these results are in line with the *fcc* structure (also validated by XRD), where the Pt resides in a local structure surrounded by Pd and Pt atoms.

For the data at the Pd-K edge (Table III), the Pd-Pd distance of the nanoparticles as well as for the Pd reference is also 2.74 Å, as expected for the *fcc* structure.¹² In contrast, the Pd-Pt bond length of 2.71 Å was slightly but significantly smaller than the bond length measured for the Pd-Pd pairs. Unlike the Pt values, the Pd-K edge based CNs suggested that the Pd is prevalently surrounded by other Pd atoms (CNs between 9.5 and 11.2) and only by a smaller number of Pt atoms (CNs between 0.6 and 1.8); the variation of the CNs among the different samples was not statistically significant.

The results of the analysis of the EXAFS spectra from both the Pd-K and Pt-L_{III} edges can be explained with a well-structured Pd

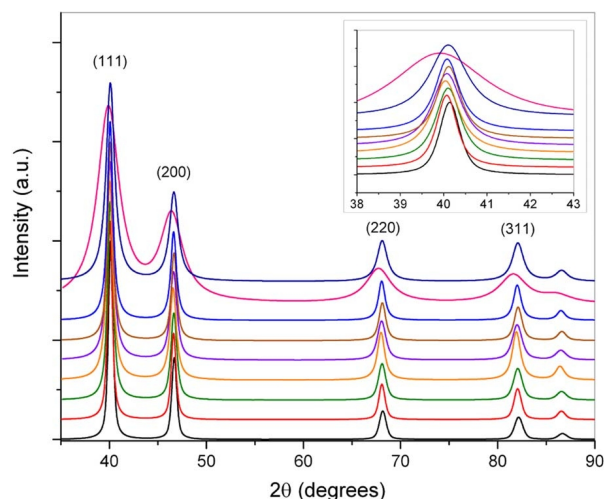


Figure 3. Shift-corrected and normalized XRD spectra with the Miller indices of the different catalysts: Pd nanocubes (black) and PtPd NPs: 0.6 h (red), 2 h (green), 4 h (orange), 6 h (violet), 8 h (brown), 17 h (blue) and pure Pt (pink), and Pd (marine).

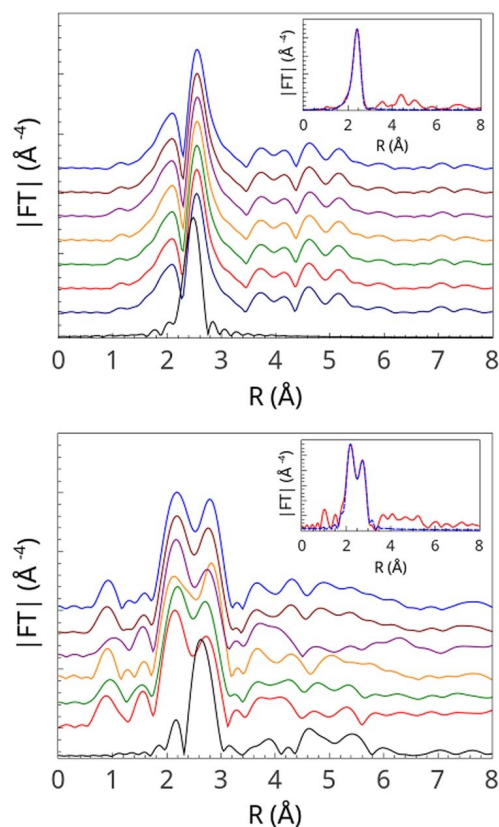


Figure 4. Fourier-transformed EXAFS spectra of the NPs at Pd-K (up) and Pt-L_{III} (down) edges. Pure Pt or Pd metal (black), Pd nanocubes (marine) and PtPd NPs: 0.6 h (red), 2 h (green), 4 h (orange), 6 h (violet), 8 h (brown), 17 h (blue). Insets: fitting of the PtPd 2h NPs: experimental (red line) and fitted (dotted blue line) Fourier-transformed EXAFS spectra (R range 1.7–3, k^3 weighted, $S_0^2 = 0.8$).

Table II. Coordination numbers (CN), interatomic distances (R), Debye Waller factors (σ^2), and energy shifts (E_0) at the Pt-L_{III} edge.

Sample	Pt-Pt shell			Pt-L _{III} edge			E_0 [eV]	R_{factor}^2 res (%)
	CN	R [Å]	σ^2 [Å ²]	CN	R [Å]	σ^2 [Å ²]		
PtPd 0.6 h	6.7	2.72	0.0058	4.8	2.72	0.0058	5.9	5.4
PtPd 2 h	6.2	2.73	0.0057	5.1	2.73	0.0057	7.1	4.0
PtPd 4 h	8.7	2.75	0.0055	3.5	2.74	0.0055	8.3	2.3
PtPd 6 h	6.7	2.74	0.0061	4.8	2.74	0.0061	7.8	3.3
PtPd 8 h	7.3	2.74	0.0056	4.8	2.74	0.0056	7.7	2.2
PtPd 17 h	7.6	2.74	0.0056	4.3	2.74	0.0056	7.8	2.7

Table III. Coordination numbers (CN), interatomic distances (R), Debye Waller factors (σ^2), and energy shifts (E_0) at the Pd-K edge.

Sample	Pd-Pt shell			Pd-K edge			E_0 [eV]	R_{factor}^2 res (%)
	CN	R [Å]	σ^2 [Å ²]	CN	R [Å]	σ^2 [Å ²]		
PtPd 0.6 h	0.6	2.71	0.0051	11.2	2.74	0.0009	9.1	0.3
PtPd 2 h	1.4	2.71	0.0054	10.7	2.74	0.0054	5.4	1.6
PtPd 4 h	1.7	2.71	0.0053	10.5	2.74	0.0053	5.6	1.7
PtPd 6 h	1.7	2.72	0.0053	9.5	2.74	0.0056	8.7	4.2
PtPd 8 h	1.7	2.70	0.0053	10.2	2.74	0.0053	5.1	1.3
PtPd 17 h	1.8	2.71	0.0052	10.2	2.74	0.0052	5.3	1.5

metal core where most of the Pd atoms possess Pd neighbors and that is surrounded by a thin Pt shell with most of the Pt atoms having Pd neighbors. Confirming the TEM and EDS observations, the higher coordination numbers for the Pt-Pt bond from the Pt-L_{III} measurements (Table II) suggest an aggregation of Pt in the surface, with a little increase after 8 and 17 h of synthesis. The fitting of EXAFS spectra at Pt-L_{III} edge, with an increasing of the coordination numbers for the Pt-Pt bond when the Pt content increase also correlates well with the EDS results.

Electrochemical properties.—*Electrochemically active surface area (ECSA).*—The ECSA was determined using the charge transferred during the hydrogen adsorption/desorption on the surface of the electrode (Q_H) and the mass (m) of deposited catalyst PtPd/C. These chemical processes appear on the voltammograms between 0.05 and 0.30 V (Figure 5). Q_H was calculated by integration of the area under the CV curve (Eq. 4):

$$Q_H = \frac{\int i dE}{\nu} \quad [4]$$

where i is the current, E is the potential, and ν is the scan rate. The ECSA was calculated following Eq. 5, considering a reference charge density for the oxidation of a monolayer of hydrogen of 2.4×10^{-4} C. cm⁻² for the pure Pd and 2.1×10^{-4} C. cm⁻² for the pure Pt and PtPd nanoparticles. The roughness factor²³ (Eq. 6) permits the comparison of the active surface area (A_{real}) and the geometric area of the electrode ($A_{\text{geometric}}$) of the different samples (Figure 6).

$$ECSA = \frac{1}{2.1 \times 10^{-4}} \times \frac{Q_H}{m_{\text{PtPd}}} \quad [5]$$

$$r_f = \frac{A_{\text{real}}}{A_{\text{geometric}}} \text{ with } A_{\text{real}} = \frac{Q_H}{m_{\text{PtPd}}} \quad [6]$$

All ECSA and roughness factor values possess an estimated total error (experimental and mathematical) of more than 10% with three samples per particle batch. The ECSA values are in the same range like the literature values for PtPd NPs coated on carbon.²⁴ For all CVs (Figure 5), three characteristic regions are visible on the voltammograms: Firstly, the hydrogen adsorption-desorption between 0.05 and 0.30 V, with the adsorption of hydrogen from 0.05 to 0.075 V and

the desorption until 0.30 V. Subsequently, the double layer charging (0.30 to 0.65 V), and, between 0.65 and 1.20 V, the formation and adsorption of hydroxide anions and oxygen on the catalyst followed by their reduction take place (Figure 5). The ECSA for the 4 h PtPd NPs ($100.6 \text{ m}^2 \cdot \text{g}^{-1}$) is higher than for the commercial Pt coated on carbon ($84.04 \text{ m}^2 \cdot \text{g}^{-1}$), while the ECSA of the particles synthesized in 2 h is similar. A significant increase of the ECSA between pure Pd and PtPd core-shell nanoparticles is apparent, with high ECSA values for the particles (Table IV) with a concave shape and a thin layer of PtPd visible on the TEM images (cf. Figures 1 and 2). For the particles with a longer time of synthesis (6 and 8 h), the ECSA decreases, with

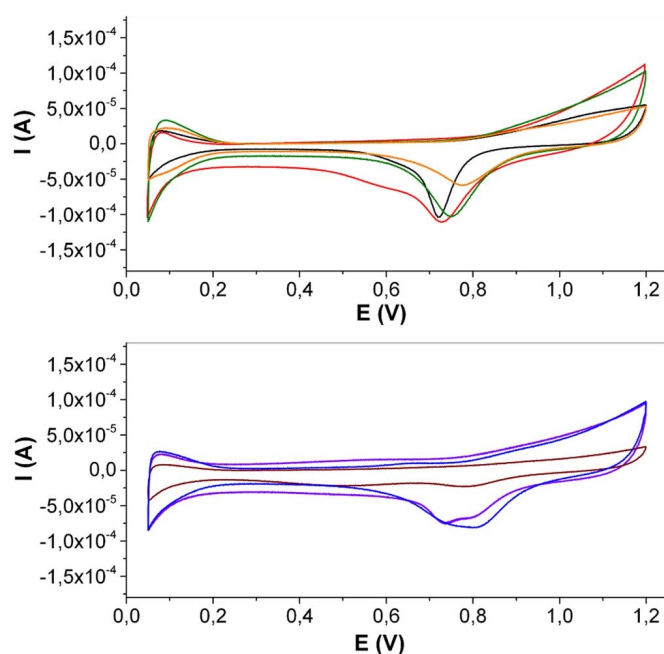


Figure 5. Voltammograms for the ECSA determination. Up: Pure Pd (black) and PtPd NPs, 0.6 h (red), PtPd 2 h (green), 4 h (orange). Down: Pt (black) and PtPd NPs, 6 h (violet), 8 h (brown), 17 h (blue).

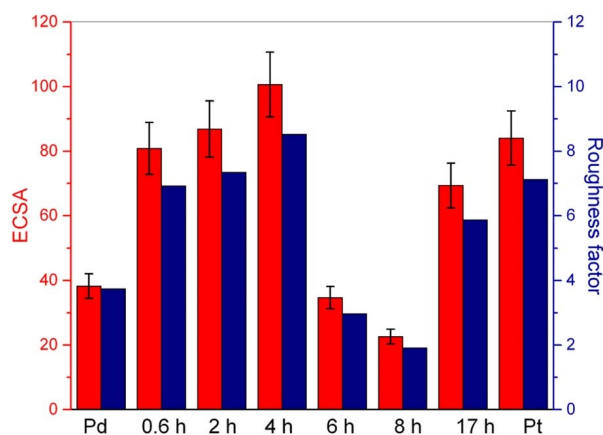


Figure 6. Electrochemically surface area (red) with errors (black) and roughness factors (blue) for the different samples.

values lower than the pure Pd nanocubes. After 17 h, the ECSA is again higher than for pure Pd nanoparticles, in the same range of the particles synthesized in less than 4 h. The higher ECSA values for the core-shell PtPd NPs (except for the particles synthesized within 6 and 8 h) compared to the pure Pd nanocubes are caused by different factors. Using the galvanic replacement, the formation of a thin Pt or PtPd layer on the surface of the Pd core occurs, which is visible in the TEM images and confirmed by the EDS measurements. The Pt shell thickness is a main parameter to control the activity of core-shell catalysts.²⁵

Furthermore, the geometric and electronic structure of the core is also important for the catalytic performances. With the development of concave nanoparticles, the structure changes significantly and important modifications of the particle shape and the thickness of the shell occur. The co-deposition of Pt and the replacement of Br atoms during the synthesis, with the formation of a PtPd alloy (cf. EXAFS results) with a different electronic structure, leads to additional chemical active sites,²⁶ which may also cause a higher ECSA value. In addition, the Pt:Pd ratio within the particles has a great influence on the ECSA and the ORR performance.^{27–29} Consequently, the evolution of the roughness factor with the time of synthesis shows a good correlation with the ECSA (Figure 6).

The small values for the particles synthesized in 6 and 8 h indicate a worse adsorption and desorption of hydrogen at the surface of the electrode. The alloy formed in the shell of the particles changes, with an evolution of the crystalline (lattice parameters and *d-spacing*) and atomic structure (coordination numbers and interatomic distances) with the synthesis time, affecting the electrochemical properties. The evolution of the shape of the particles, from pure Pd nanocubes to concave core-shell concave nanocubes, and the different Pt:Pd ratios with the time of synthesis also contribute to new chemical properties. A quantification by ICP-MS, and XPS measurements, is necessary to

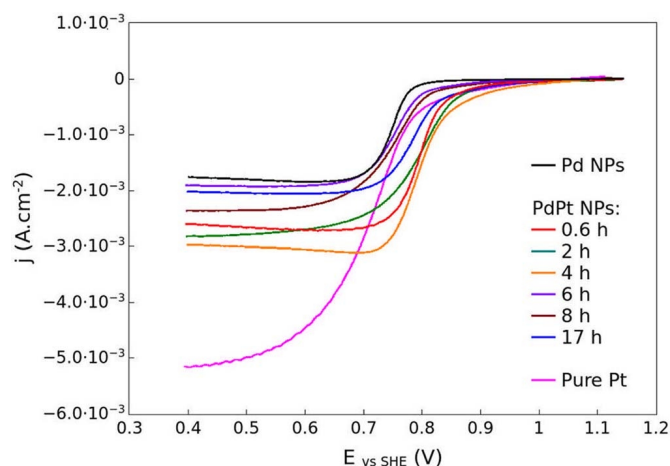


Figure 7. Characteristic voltammograms for the ORR of NPs and pure Pt coated on carbon in O₂ saturated HClO₄ aqueous solution (1.2 to 0.4 V, 5 mV s⁻¹, 1600 rpm).

gain more information, in particular via the detection of very small concentrations and their distribution on the surface of the particles.

Oxygen reduction reaction.—The ORR kinetic was studied applying the Koutecký-Levich equation on the parameters extracted from the voltammetric experiments. The electrical current (*i*), measured by LSV, was transformed into the current density *j* using the geometric area of the electrode (0.1963 cm²). Three different regions are apparent in the voltammograms: Until 0.60 V, the reaction on the surface of the electrode is controlled by diffusion processes (the mass transport). When the potential increases, between 0.60 and 0.85 V, diffusional and kinetic processes occur on the surface of the electrode with adsorption and desorption of oxygen atoms and OH radicals, and a possible formation of H₂O₂. Finally, up to 0.85 V, the dominant processes are pure kinetic phenomena. In the voltammograms (Figure 7), the onset of the ORR for the pure Pd is found at 0.75 V. For the different PtPd NPs and the pure Pt sample, the onset potential increases gradually until 0.87 V. Working with a RDE at 1600 rpm ensures fast convective transport of the active species. The catalytic activities of the particles were compared via the mass activity *j*_{mass}, defined as the kinetic current density *j*_k, normalized to the mass of nanoparticles that is deposited on the surface of the electrode, *m*_{Pd}. The current density *j* from the measurement using an RDE at 1600 rpm is composed of the kinetic current density *j*_k and the Levich current density *j*_L by the Koutecký-Levich equation:

$$\frac{1}{j} = \frac{1}{j_L} + \frac{1}{j_k} \quad [7]$$

The kinetic current density *j*_k is calculated with the values of the current densities *j* at 0.85 V and *j*_L at 0.50 V for the anodic scan. The received kinetic current density at 0.85 V was normalized to the

Table IV. Catalytic properties and their evolution for the ORR.

Sample	ECSA (m ² g ⁻¹)	Roughness factor	n (e ⁻) exchanged	ORR (0.85 V) A. g ⁻¹		
				Fresh	Degraded	Change (%)
Pd nanocubes	33.3	3.7	1.95	4.8	4.7	2
PtPd 0.6 h	80.8	7.9	2.57	17.6	15.1	14
PtPd 2 h	86.8	8.4	1.58	24.7	19.1	22
PtPd 4 h	100.6	8.5	1.93	33.4	32.7	2
PtPd 6 h	34.7	3.4	1.45	6.7	5.5	18
PtPd 8 h	22.6	2.2	1.25	8.1	9	2
PtPd 17 h	69.3	6.7	1.78	16.8	16.5	2
Commercial Pt	84.0	7.1	4.06	17.9	15.4	14

mass of catalyst (m_{PtPd}) to compare the catalytic performances of the particles for the ORR:

$$j_{\text{mass}} = \frac{j_k}{m_{\text{PtPd}}} \quad [8]$$

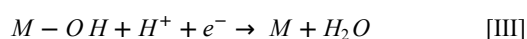
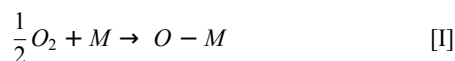
For the different samples, the ORR mass activities were determined (Table IV) whereas the Pd nanocubes show the lowest mass activity ($4.8 \text{ A} \cdot \text{g}^{-1}$) due to the absence of Pt. It is known from literature that Pd possesses a significantly lower catalytic activity for the oxygen reduction reaction in acid media than Pt or bimetallic NPs based on Pd alloys³⁰ or core-shell structures.^{31,32} The addition of another metal^{6,33} improves the catalytic properties through an increase of the number of active sites and a modification of the electronic structure of the particles. After 0.6 h, the mass activity of the NPs is more than three times higher ($17.6 \text{ A} \cdot \text{g}^{-1}$) than for Pd nanocubes and close to the commercial Pt ($17.9 \text{ A} \cdot \text{g}^{-1}$). From 0.6 to 4 h, the ORR activity of the particles increases further and is superior to the commercial Pt after 2 h ($24.7 \text{ A} \cdot \text{g}^{-1}$) and 4 h ($33.4 \text{ A} \cdot \text{g}^{-1}$). The galvanic replacement increases the concentration of Pt by co-deposition and replacement of Br atoms by Pt atoms, increasing the number of the active sites for the ORR. The most promising particles were synthesized in 4 h, with a Pd molar fraction of 0.7, which is favorable for the ORR.^{25,30,12}

Like for the ECSA, the particles synthesized in 6 and 8 h have a lower mass activity (6.7 and $8.1 \text{ A} \cdot \text{g}^{-1}$ respectively), still higher than pure Pd nanocubes. For longer synthesis times, the mass activity increases again slightly lower than for pure commercial Pt catalyst after 17 h of synthesis ($16.8 \text{ A} \cdot \text{g}^{-1}$). For the different stages of the NPs synthesis, the catalytic properties of the particles are not only linked to the amount of Pt but also to the chemical active area (ECSA and roughness factor): The catalytic performances for the ORR correlate well with the ECSA with a high catalytic activity of the ORR in case of high ECSA values. As observed on TEM images, the evolution of the particles (atomic and crystalline structure, shape) influences the catalytic properties, namely the area of the active surface for the ORR.^{34,35}

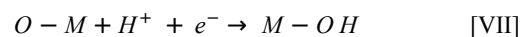
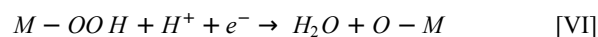
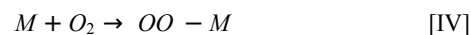
Stability of the catalyst.—In addition to their catalytic performances, the particles need to be stable with no decrease of mass activity even after long times of utilization. To study the stability of the NPs, their mass activities were determined before and after 2000 CV cycles (between 0.05 V and 1.20 V with a scan range of 0.10 V s^{-1}), revealing a different stability behavior (Table IV). Taking in account the experimental error ($\sim 10\%$), the mass activity was stable for the Pd nanocubes and the PtPd NPs that were synthesized in 4 h, 8 h, and 17 h. For the other samples, a decrease of the mass activity was observed, namely for the particles synthesized in 0.6 h (14%), 2 h (22%), and 6 h (18%) as well as for the commercial Pt (14%). For the studied samples, the particles synthesized with a molar fraction of Pd of 0.70 and 0.95 show a stable catalytic activity, with a high chemical and physical stability than the other particles.

Comparison of the kinetic properties of the NPs for the ORR.—The ORR at the surface of the electrode in HClO₄ aqueous solution is divided in different steps following two different mechanisms^{36,37} the dissociative and the associative one.

The dissociative mechanism appears like the break of the O-O bond by adsorption of O atoms on chemically active site (M) on the surface of the electrode and the formation of oxides (Pt or Pd oxide) (I). The reaction of the oxide with a proton and one electron creates a hydroxide (II). The bond between Pd or Pt and OH dissociates in acid solution and water is formed (III).



The associative mechanism includes the oxygen reduction via the formation of peroxide intermediates:



The formation of H₂O₂ is also possible in step VI via the desorption of HO₂ from the surface. Thus the occurrence of hydrogen peroxide as a stable compound indicates an incomplete electron transfer. Via Tafel and Levich analysis, the limiting step in the ORR process was investigated. The Levich analysis was executed using different rotational speeds (0, 100, 400, 900, 1600, and 2500 rpm) and the number of exchanged electrons, n , was calculated via the Levich equation:

$$i_L = 0.620 \cdot n \cdot F \cdot A \cdot C_0 \cdot D^{\frac{2}{3}} \cdot \nu^{-\frac{1}{6}} \cdot \omega^{\frac{1}{2}} \quad [9]$$

i_L is the Levich (or diffusion) current measured at 0.5 V, F the Faraday constant ($96485 \text{ C} \cdot \text{mol}^{-1}$), A the geometric area of the electrode (0.1963 cm^2), C_0 the concentration of the molecular oxygen in saturated solution ($1.26 \times 10^{-6} \text{ mol} \cdot \text{cm}^{-3}$), D the diffusion coefficient of the oxygen in the solution ($1.67 \times 10^{-5} \text{ cm}^2 \cdot \text{s}^{-1}$), ν the kinetic viscosity of the electrolyte ($1.009 \times 10^{-2} \text{ cm}^2 \cdot \text{s}^{-1}$), and ω the rotational speed of the RDE ($\text{rad} \cdot \text{s}^{-1}$). The analysis revealed that the number of exchanged electrons is close to 2 for the PtPd NPs and close to 4 for the pure Pt (Figure 8, Table V). The transfer of two electrons during the ORR revealed the formation of hydrogen peroxide during the reaction, reducing the catalytic activity. The presence of bromide in the nanoparticles poisoned the ORR with Br at the surface of the particles on chemical active sites, reducing the ECSA and the catalytic activity.

Applying a Tafel plot, the exchange current density, an important parameter for the comparison of the catalytic properties of the NPs, was determined by the extrapolation of the experimental Tafel line to the thermodynamic potential for the ORR (1.23 V) using the simplified Tafel equation:

$$E = a + b \times \log j_k \quad [10]$$

The analysis of the Tafel plots (Figure 9, Table V) revealed a pseudo-linear region of the curves between 0.75 and 0.9 V with two slopes, between 0.056 and 0.075 V dec⁻¹ for low current densities and between 0.111 and 0.162 V dec⁻¹ for high current densities. These slopes are in the same range as in the literature,^{38,39} 0.060 V dec⁻¹ for low and 0.120 V dec⁻¹ for high current densities.

The presence of a slope close to 0.060 V dec⁻¹ at high potentials (higher than 0.8 V) revealed a mix Pt/PtO at the surface of the electrode. In presence of Pt oxide, the rate determining step (RDS) is a pseudo two electrons transfer while for the pure Pt surface, (low potentials, high current density) the RDS is the first electron transfer of the oxygen reduction reaction (with the assumption of the adsorption of O₂ according to a Langmuir isotherm).^{40,41} The coverage or adsorption of oxygen-containing species causes changes in the kinetic of the oxygen reduction reaction, as it is confirmed by the results of the Tafel and Levich analysis.

For the studied samples, the values of the different current exchange densities are not completely in agreement with the ORR performances: the catalytic activity for the ORR is higher for the particles synthesized in 0.6 h and 2 h, with the exchange current densities lower than for the 17 h nanoparticles.

The catalytic performances of the particles could be higher with more active sites on the surface, with an easier adsorption-desorption,

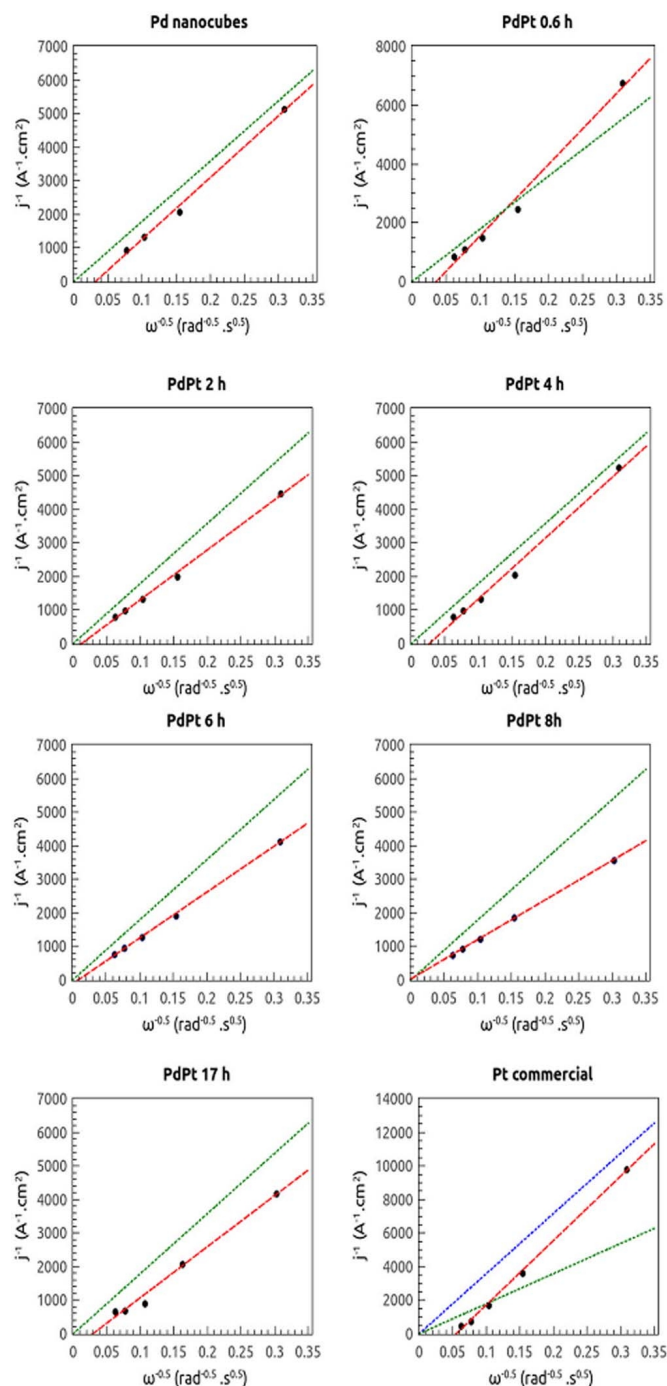


Figure 8. Levich diagrams for the different samples. Intensity measured at 0.4 V at different rotational speeds (black points), and red lines linearization following the Koutecky Levich equation. The green lines correspond to an exchange of two electrons and the blue lines to a transfer of 4 electrons during the ORR.

and with less formation of hydrogen peroxide, which poisons the ORR. Even if the number of electrons is two during the ORR, the higher catalytic properties of the PtPd NPs synthesized in 2 and 4 h can be explained by a higher number of chemical active sites, permitting to compensate the formation of oxygen peroxide. For the majority of the samples, the exchange current density decreases after the stability test, indicating a degradation of the particles, leading to deteriorated catalytic properties.

Study of the mass transport phenomena by electrochemical impedance spectroscopy (EIS).—The EIS measurements were done

Table V. Evolution of the kinetic parameters determined by Tafel analysis.

Sample	Fresh samples		Degraded samples	
	1 st Tafel slope (V .dec ⁻¹)	2 nd Tafel slope (V .dec ⁻¹)	1 st Tafel slope (V .dec ⁻¹)	2 nd Tafel slope (V .dec ⁻¹)
PtPd 0.6 h	0.058	0.110	0.053	0.109
PtPd 2 h	0.073	0.154	0.060	0.148
PtPd 4 h	0.058	0.122	0.054	0.131
PtPd 6 h	0.053	0.104	0.050	0.096
PtPd 8 h	0.053	0.106	0.053	0.107
PtPd 17 h	0.057	0.134	0.061	0.127
Commercial Pt	0.052	0.133	0.054	0.105

applying a constant convection with a RDE at 1600 rpm with an aqueous HClO₄ (0.1 mol L⁻¹) solution as electrolyte support ensuring negligible migration phenomena⁴² and a constant oxygen concentration at the electrode/electrolyte interface. For the analysis of the spectra, the samples were considered without space between the support, the particles, and the Nafion layer. The impedance was measured at a DC potential of 0.5 V, enabling a reaction that is controlled by the diffusion processes. The resulting EIS spectra, typical from diffusion

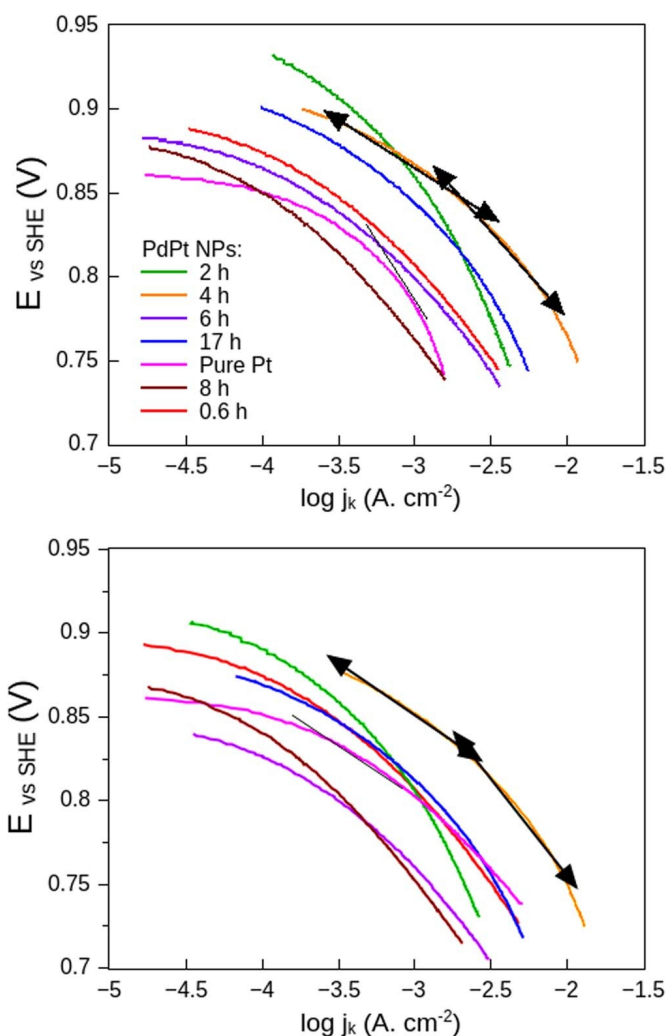


Figure 9. Tafel plots (up) before and (down) after the stability test for Pt and PtPd NPs.

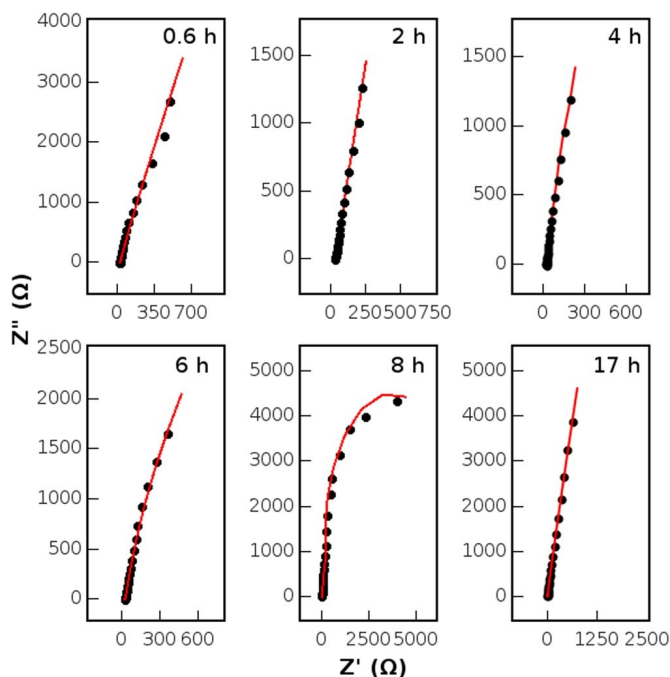


Figure 10. Experimental (black dots) and fitted (red lines) Nyquist diagrams for the nanoparticles with different synthesis times.

controlled reaction, feature two different parts in the Nyquist plots (Figure 10).

At high frequencies, a straight line with an angle versus the x-axis that is close to 45° occurs for all the samples. It is followed by a degenerated arc for the 6 h and 8 h samples, while a line with an angle versus the x-axis close to 90° appears at low frequencies for the other samples (including pure Pt). These plots are similar to the theoretical diagrams of a Randles circuit⁴³ with finite diffusion with reflective or transmissive boundary (Figure 11).

Within the Randles model circuit, the first resistor (R_s) corresponds to the resistance of the electrolyte. The presence of one inductor (L), connected in series with the resistor R_s traduces the experimental errors. The Faradaic processes are represented by the combination of a charge transfer resistor (R_{CT}), which represents the resistance for charge carriers to pass the electrolyte/electrode interface, a Warburg element to model the diffusion phenomena, and a constant phase element (CPE), a non-ideal capacitor, which is connected in parallel and describes the capacitance of the double layer between the electrolyte and the electrode surface. The double layer is formed by the separation of the ions and charged species accumulated at the surface of the electrode under the influence of the applied potential. The resulting capacitance is not represented by an ideal capacitor due to heterogeneities in the electrodes: rough and porous electrodes, inho-

mogeneous catalyst repartition on the surface of the electrode, and the Nafion layer covering the particles. The total impedance of the system is a combination of the individual impedances of the electrical components present in the equivalent circuit:

$$Z_{TOTAL} = Z_{R_s} + Z_L + Z_{(CPE, R_{CT}, W)} \quad [11]$$

with the different impedances: Z_{R_s} for the resistance of the electrolyte, $Z_{R_{CT}}$ for the charge transfer resistance, Z_L for the inductor with an inductance L, Z_{CPE} for the CPE with a capacitance Q and a dimensionless factor n, and Z_W for the Warburg element.

$$Z_{R_s} = R_s, \quad Z_{R_{CT}} = R_{CT}, \quad Z_L = j\omega L \text{ and } Z_{CPE} = \frac{1}{Q(j\omega)^n} \quad [12]$$

Considering a finite diffusion in the diffusion-controlled region, the impedance of the Warburg element, Z_W , can be represented by the equation:

$$Z_W = \frac{R_D}{\frac{j\omega L_D^2}{D}} \times \tanh \frac{j\omega L_D^2}{D} \quad \text{for a transmitting diffusion} \quad [13]$$

And

$$Z_W = \frac{R_D}{\frac{j\omega L_D^2}{D}} \times \cot h \frac{j\omega L_D^2}{D} \quad \text{for a reflective diffusion} \quad [14]$$

R_D is the diffusion resistance, D is the diffusion coefficient, L_D is the thickness of the diffusion layer and ω the radial frequency ($\omega = 2\pi \cdot f$). In the case of finite diffusion, the Nyquist diagrams are separated in two different regions at the diffusion frequency ω_D . Up to this, the impedance response is a pure Warburg diffusion while at lower frequencies ($\omega \rightarrow 0$), the impedance response depends on the chemical diffusing species: when an accumulation of species occurs at the surface of the electrode ($x = L_D$), the diffusion is reflective, with a diffusion capacitance C_D and, in case of transmitting or absorbing diffusion, the diffusing species at the surface of the electrode are directly consumed with a limiting diffusion resistance R_D . These values depend of the chemical system and the applied potential, without distinction among the charged species (metal, carbon support, Nafion and ionic species). The constant of diffusion, τ , for the layer of effective diffusion thickness L is defined as:

$$\tau = \frac{L^2}{D} \quad [15]$$

All the Nyquist plots (Figure 10) show finite diffusion phenomena during the impedance measurements at 0.5 V. After the Warburg diffusion at high frequencies (straight line at 45°), two different features were found: a straight line with an angle versus the x-axis close to 90° , characteristic of a finite diffusion with reflective boundaries occurs for all the samples except for PtPd 6 h and PtPd 8 h. For these two samples, the impedance spectra are composed of a straight line at 45° at high frequencies and a formation of an arc for the low frequencies, which is characteristic of a diffusion layer with transmissive boundary. However, after fitting, small differences were visible between the investigated samples (Table VI).

The resistance of the electrolyte (R_s) is close to 30 Ω and shows only small variations. For all measurements, the resistance for the charge transfer (R_{CT}) is small, around 0.5 to 1.0 Ω for the PtPd NPs and even 0.2 Ω for the pure Pt, indicating a facile charge transfer. R_{CT} is decreasing for the particles with an increasing concentration of Pt: 1.01 Ω for the particles synthesized in 0.6 h (Pt molar fraction 4.1%) to 0.16 Ω for the pure Pt. The particles prepared in 6 h are an exception, with a smaller resistance for the charge transfer and a Pt molar fraction of 19.5%. This can be a result of a Pt-rich surface but is in contradiction to the bad catalytic properties. It could be explained by the absence of a PtPd alloy in the surface of the particles and a reduction or disappearing of the electronic effect, inducing a reduction of the catalytic activity. The dimensionless factor of the CPE, n, is close to 1, so the parameter Q can be considered as a capacitance,

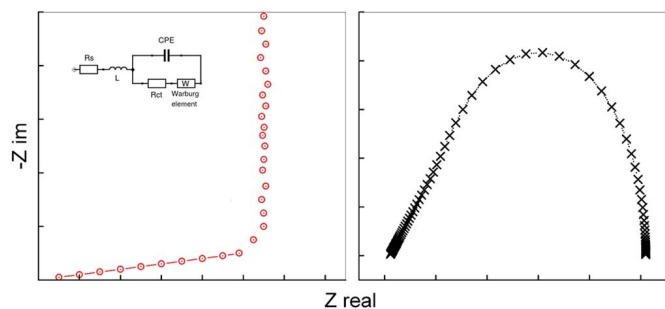


Figure 11. Theoretical Nyquist diagrams for a finite reflective (left) and transmissive (right) diffusion, with the equivalent Randles circuit (inset).

Table VI. Characteristics of the equivalent circuit after fitting of the impedance spectra for the different NPs.

Sample	R_s (Ω)	R_{CT} (Ω)	$L(H) \times 10^{-5}$	$Q(F) \times 10^{-4}$	n	R_w (Ω)	τ_w (s) $\times 10^{-5}$	W_N	L (μm)
PtPd 0.6 h	30.3	1.01	1.6	1.13	0.94	11.4	7.6	0.47	3.56
PtPd 2 h	30.5	0.78	1.6	5.60	0.84	49.6	42.1	0.47	8.38
PtPd 4 h	28.0	0.53	1.7	0.04	0.90	11.3	12.7	0.47	4.61
PtPd 6 h	23.7	0.48	1.4	0.30	0.80	14.2	13.7	0.46	4.78
PtPd 8 h	34.8	0.88	1.9	3.86	0.94	73.8	10.2	0.47	4.13
PtPd 17 h	31.4	0.52	1.7	1.88	0.93	18.7	4.9	0.48	2.86
Commercial Pt	24.6	0.16	1.4	13.9	0.85	17.9	37.8	0.47	7.95

indicating the accumulation of charged species in the diffusion layer. The small values of Q , depending on different parameters,⁴⁴ vary between 4×10^{-6} F (PtPd 4 h) and 1.39×10^{-3} F (Commercial Pt). For all the PtPd particles, according to the values after fitting, the ionic accumulation is small, particularly for the particles prepared in 4 and 6 h (4×10^{-6} and 3×10^{-5} F, respectively). The transmitting diffusion phenomena resorting from the impedance spectra of the particles prepared in 6 and 8 h, may reflect the low adsorption of the chemical active species (especially the oxygen) at the surface of the particles and so would thus justify the low catalytic performances of these particles. The higher Warburg resistance indicated a lower diffusion of charged species, hence reducing the catalytic activity of the particles synthesized in 8 h.

For the other samples, the reflecting diffusion can traduce the adsorption of oxygen atoms and better catalytic properties but without clear link with the catalytic performances. The mass transport, represented by the Warburg diffusion resistance depends on the shape and the chemical composition of the particles. For the particles prepared in 2 h (with the second ECSA and ORR properties), it can be compensated by a higher capacitance but not for the particles synthesized in 4 h. Concerning the diffusion characteristics, in the case of the ORR, the diffusion constant is associated to the potential-dependent adsorption of O_2 , the dissociation of the O-O bond and the different chemical steps of the reaction, depending on the applied potential. The inverse of the diffusion constant, τ^{-1} is related to the desorption rate constant of the intermediates of the ORR. At 0.5 V, the particles synthesized in 17 h show the highest desorption rate, followed by the particles synthesized in 0.6 h, 8 h, 4 h, 6 h, commercial Pt, and 2 h, with significant inferior values. Compared to the particles PtPd 17 h, the diffusion layer is really thick for the pure Pt and the PtPd 2 h NPs. The small values of the Warburg impedance (between 11.4 and 73.8 Ω) and charge transfer resistance agree with structured nanoparticles possessing a high number of chemical active sites, enhancing the charge transfer, and confirm the phenomena of mass transport at 0.5 V. However, the results of the impedance do not clearly confirm the catalytic performances and the physico-chemical properties of the particles determined by TEM-EDS, XRD, EXAFS, and LSV. Further measurements with a higher frequency range and with an electromagnetic protection (Faraday cage) can improve the EIS characterization.

Conclusions

The palladium (core) - platinum (shell) nanoparticles were synthesized by galvanic replacement and studied after different times of synthesis to establish relationships between the physical properties, the chemical compositions and the catalytic activity regarding the oxygen reduction reaction, a crucial reaction in fuel cells. TEM measurements revealed the evolution of the shape of the particles, from *fcc* pure palladium to cubic-concave core-shell bimetallic nanoparticles. The chemical composition of the particles varied, with an increasing amount of platinum until 4 h of synthesis (Pt molar fraction 0.3) and a subsequent decrease until 8 h, followed by a final increase up to 17 h. However, future experiments that offer a higher precision (e.g. ICP-MS) are necessary. The formation of a platinum-palladium alloy within the outer shell of the particles and a modification of the structure of the nanoparticles was revealed by EXAFS studies and

by XRD measurements, respectively. Further XPS and in-situ XPS experiments would be helpful to complete the characterization of the particles. The determination of the electrochemically active surface area (ECSA) and the catalytic activities for the oxygen reduction reaction by CV and LSV permitted to compare the catalytic performances and stabilities of the nanoparticles. As expected, the addition of platinum with the formation of an alloy in the shell of the particles influences the catalytic activity and stability. After 0.6 h, particles with a small amount of platinum (molar fraction of 0.05) and an activity and stability close to a pure commercial Pt catalyst are obtained. After 2 h, the catalyst shows a superior catalytic activity compared to the pure platinum and the best performance is achieved for the particles synthesized within 4 h, with a stable catalytic activity that is two times higher than for pure platinum and a lower amount of the expensive metal (Pt molar fraction of 0.7).

Acknowledgments

We thank all the research group working at the Rossendorf Beamline BM20 A (ESRF, Grenoble, France), Dr Stephanie Höpener for TEM and EDS mapping, Dr. Sindy Fuhrmann for the access to the XRD and her help for the data analysis, Dr. Igor Perevyazko for his help and the access to an high speed centrifugation machine. Thanks also to all the technicians of the workshop of the university for the participation in the fabrication and test of the experimental cells. This study was accomplished with the financial help of the Carl Zeiss Foundation (Germany).

ORCID

Simon Tymen  <https://orcid.org/0000-0001-7103-0045>

References

1. M. Chatenet, M. Aurousseau, R. Durand, and F. Andolfatto, *J. Electrochem. Soc.*, **150**, D47 (2003).
2. A. L. Ocampo, M. Miranda-Hernández, J. Morgado, J. A. Montoya, and P. J. Sebastian, *J. Power Sources*, **160**, 915 (2006).
3. W. An and P. Liu, *J. Phys. Chem. C*, **117**, 16144 (2013).
4. E. F. Holby, W. Sheng, Y. Shao-Horn, and D. Morgan, *Energy Environ. Sci.*, **2**, 865 (2009).
5. K. W. Park, J. H. Choi, and Y. E. Sung, *J. Phys. Chem. B*, **107**, 5851 (2003).
6. M. Bele et al., *Chem. Commun.*, **50**, 13124 (2014).
7. W. Li et al., *Electrochimica Acta*, **49**, 1045 (2004).
8. S. Tymen, A. C. Scheinost, C. Friebe, and U. S. Schubert, *Adv. Nanoparticles*, **06**, 75 (2017).
9. X. Huang et al., *Nano Lett.*, **12**, 4265 (2012).
10. J. W. Hong et al., *ACS Nano*, **6**, 2410 (2012).
11. Y. Y. Chu, Z. B. Wang, Z. Z. Jiang, D. M. Gu, and G. P. Yin, *J. Power Sources*, **203**, 17 (2012).
12. H. Zhang et al., *J. Phys. Chem. C*, **114**, 11861 (2010).
13. H. Zhang et al., *ACS Nano*, **5**, 8212 (2011).
14. S. M. Webb, *Phys. Scr.*, 1011 (2005).
15. T. Ressler, *J. Synchrotron Radiat.*, **5**, 118 (1998).
16. A. L. Ankudinov and J. J. Rehr, *Phys. Rev. B*, **56**, R1712 (1997).
17. S. Gražulis et al., *Nucleic Acids Res.*, **40**, D420 (2012).
18. L. Lutteroti, S. Matthies, and H. R. Wenk, in *Twelfth International Conference on Textures of Materials (ICOTOM-12)*, **1**, 1599 (1999).
19. A. Dutta and J. Datta, *Int. J. Hydrog. Energy*, **38**, 7789 (2013).
20. Y. K. Kuo, B. T. Liou, S. H. Yen, and H. Y. Chu, *Opt. Commun.*, **237**, 363 (2004).

21. V. A. Lubarda, *Mech. Mater.*, **35**, 53 (2003).
22. N. Toshima and T. Yonezawa, *New J. Chem.*, **22**, 1179 (1998).
23. K. J. J. Mayrhofer et al., *Electrochimica Acta*, **53**, 3181 (2008).
24. Z. M. Zhou et al., *Int. J. Hydrog. Energy*, **35**, 1719 (2010).
25. M. Oezaslan, F. Hasché, and P. Strasser, *J. Phys. Chem. Lett.*, **4**, 3273 (2013).
26. A. J. J. Jebaraj, N. S. Georgescu, and D. A. Scherson, *J. Phys. Chem. C*, **120**, 16090 (2016).
27. G. Zhang et al., *J. Phys. Chem. C*, **117**, 13413 (2013).
28. S. Thanasilp and M. Hunsom, *Renew. Energy*, **36**, 1795 (2011).
29. C. L. Lee, H. P. Chiou, S. C. Wu, and C. C. Wu, *Electrochimica Acta*, **56**, 687 (2010).
30. O. Savadogo et al., *Electrochem. Commun.*, **6**, 105 (2004).
31. V. K. Gupta, M. L. Yola, N. Atar, Z. Üstündağ, and A. O. Solak, *J. Mol. Liq.*, **191**, 172 (2014).
32. A. N. Golikand, M. Asgari, and E. Lohrasbi, *Int. J. Hydrog. Energy*, **36**, 13317 (2011).
33. K. A. Kuttiviel et al., *Nat. Commun.*, **5**, 15 (2014).
34. N. S. Porter, H. Wu, Z. Quan, and J. Fang, *Acc. Chem. Res.*, **46**, 1867 (2013).
35. N. An et al., *J. Phys. Chem. C*, **117**, 21254 (2013).
36. A. M. Gómez-Marín, R. Rizo, and J. M. Feliu, *Beilstein J. Nanotechnol.*, **4**, 956 (2013).
37. J. K. Nørskov et al., *J. Phys. Chem. B*, **108**, 17886 (2004).
38. K. D. Beard, J. W. Van Zee, and J. R. Monnier, *Appl. Catal. B Environ.*, **88**, 185 (2009).
39. K. Jukk, N. Kongi, K. Tammeveski, J. Solla-Gullón, and J. M. Feliu, *Electrochem. Commun.*, **56**, 11 (2015).
40. A. Holewinski and S. Linic, *J. Electrochem. Soc.*, **159**, H864 (2012).
41. C. Song and J. Zhang, in *PEM Fuel Cell Electrocatalysts and Catalyst Layers: Fundamentals and Applications*, J. Zhang J. Editor, p 113, Springer London (2008).
42. D. D. Macdonald, E. Sikora, and G. Engelhardt, *Electrochimica Acta*, **43**, 87 (1998).
43. J. E. B. Randles, *Discuss. Faraday Soc.*, **1**, 11 (1947).
44. N. Fouquet, C. Doulet, C. Nouillant, G. Dauphin-Tanguy, and B. Ould-Bouamama, *J. Power Sources*, **159**, 905 (2006).

Publication 3

In-situ XAFS Characterization of PtPd Nanoparticles Synthesized by Galvanic Replacement

S. Tymen, A. C. Scheinost, C. Friebe, U. S. Schubert

Adv. Nanoparticles **2017**, *6*, 75. DOI: 10.4236/anp.2017.62007. Open access article

In-Situ XAFS Characterization of PtPd Nanoparticles Synthesized by Galvanic Replacement

Simon Tymen¹, Andreas C. Scheinost², Christian Friebe^{1,3}, Ulrich S. Schubert^{1,3,4}

¹Institute of Organic and Macromolecular Chemistry (IOMC), Friedrich-Schiller University, Jena, Germany

²The Rossendorf Beamline at the European Synchrotron European Synchrotron Radiation Facility (ESRF), Grenoble, France
³Molecular Structure Division, Institute of Radiochemistry Forschungszentrum Dresden-Rossendorf (FZD), Dresden, Germany

⁴Center for Energy and Environmental Chemistry Jena (CEEC Jena), Friedrich-Schiller University, Jena, Germany

⁴Jena Center for Soft Matter (JCSM), Friedrich-Schiller University, Jena, Germany

Email: simon.tymen@uni-jena.de

How to cite this paper: Tymen, S., Scheinost, A.C., Friebe, C. and Schubert, U.S. (2017) In Situ XAFS Characterization of PtPd Nanoparticles Synthesized by Galvanic Replacement. *Advances in Nanoparticles*, 6, 75-91.
<https://doi.org/10.4236/anp.2017.62007>

Received: March 15, 2017

Accepted: May 24, 2017

Published: May 27, 2017

Copyright © 2017 by authors and Scientific Research Publishing Inc.

This work is licensed under the Creative Commons Attribution International License (CC BY 4.0).

<http://creativecommons.org/licenses/by/4.0/>



Open Access

Abstract

Platinum-palladium nanoparticles are synthesized and characterized with regard to their application in fuel cells due to their high (electro) catalytic activity. Different preparation times are applied leading to different structures from Pd cubic to core-shell PtPd concave, and different chemical compositions. The resulting particles are studied via Transmission Electron Microscopy (TEM) and in situ X-ray absorption fine structure (XAFS) measurements. The latter allows the investigation of the oxygen reduction reaction following the variations with varying applied potentials by analysis using the Iterative Transformation Factor Analysis (ITFA) and the creation of a two-component system that consists of metallic Pt-Pd and the related oxide. With the used model, the different concentrations of the oxide are linked to consecutive chemical steps of the oxygen reduction reaction. Finally, the catalytic activity of the particles is determined via linear scanning voltammetry and reveals a dependence on the shape and the composition of particles.

Keywords

Platinum, Palladium, Nanoparticles, Oxygen Reduction Reaction, In Situ XAFS, ITFA

1. Introduction

Platinum features an outstanding catalytic activity for various reactions, in particular the oxygen reduction reaction (ORR), and the oxidation of the ethanol

and the methanol. These three reactions are key steps in the working proton exchange membrane fuel cells (PEMFCs) and direct methanol fuel cells (DMFCs), which represent promising alternatives to fossil fuels as a power source for vehicles. The performances of the catalysts based on Pt can be improved by the incorporation of nanostructures with higher active surface area and, hence, higher efficiencies regarding the targeted chemical reactions. Consequently, different types of nanoparticles were synthesized possessing different sizes and shapes: Nanocubes [1], nanospheres [2] and bimetallic particles Pt-Cu [3], Pt-Pd [4], Pt-Ni [5], which enable the enhancement of the catalytic activity and also the reduction of the required amount of expensive platinum. The bimetallic particles are, e.g., alloys [6], core-shell particles [7], or nanocages [8]. In this work, we study Pt-Pd core-shell nanoparticles that are synthesized by galvanic replacement applying varying synthesis times. Different studies on Pt-Pd nanoparticles and their catalytic activity regarding the ORR were already realized, but we intended to monitor the evolution of the surface of the particles during the different steps of the reaction, namely the adsorption of oxygen and the formation of oxides, through the monitoring of the Pt-Pd and Pt-O bond. Here, the *in situ* XAFS technique represents a powerful method to study the surface of the particles during the ORR [1] [9] [10]. However, *in situ* Extended X-ray absorption fine structure (EXAFS) and X-ray absorption near edge structure (XANES) experiments, the standard fitting approach for the analysis of the spectra is not always suited to separate the different species that are present in the system. Thus, we analyzed our results using the Iterative Transformation Factor Analysis (ITFA) [11], which enabled the comparison of the different particles via their spectra and catalytic properties.

2. Experimental Section

2.1. Materials and Methods

Sodium tetrachloropalladate (Na₂PdCl₆, 98%), potassium tetrachloroplatinate (K₂PtCl₆, 98%), ascorbic acid (AA, 98%), potassium bromide (KBr, 99%), Nafion®, perfluorinated resin solution (5 wt.%) and nitric acid (HNO₃, purified by distillation) were purchased from Sigma Aldrich. Isopropyl alcohol (IPA, 99.5%) was purchased from Merck, ethylene glycol from VWR and poly(vinylpyrrolidone) (PVP, 98%) from Alfa Aesar. The black carbon XC-72R was purchased from Vulcan and the microfiltration membrane (0.45 μm filter) from Diapore, the plain carbon cloth (model 1071) from FuelCellsEtc and the graphite conductive adhesive, alcohol-based (42,465) from Alpha Aesar.

2.2. Synthesis of PtPd Nanoparticles

Depending on the particle type, size, shape, and composition, different methods were used to synthesize PdPt nanoparticles (NPs) in aqueous or organic solvents [12] [13] [14]. The synthesis of bimetallic core-shell nanoparticles [15] and PdPt alloy nanocages [8] was based on the work by Zhang [16]. Hexachloroplatinic acid (PtCl₆) was replaced by potassium tetrachloroplatinate (K

which possesses a lower oxidation state for the platinum (Pt(II)).

The galvanic replacement method to synthesize the particles was performed in two steps: First, the synthesis of Pd cubic nanoparticles, followed by the Pt-Pd core-shell nanoparticles. The Pd NPs were prepared in a solution of 0.6 g of ascorbic acid, 3 g of potassium bromide, 1.85 g of potassium chloride, and 1.05 g of poly(vinylpyrrolidone), in 80 mL of distilled water. After sonication (2 min), the solution was heated to 80 °C. After 10 min, 30 μL of PdCl_2 ($6.5 \times 10^{-3} \text{ mol}\cdot\text{L}^{-1}$) was added with a syringe (1 mL). Afterwards, the solution was kept for 3.5 h at 80 °C under magnetic stirring with a rotational speed of 1200 rpm. The platinum was added in a second step to form the PdPt nanoparticles. 10 mL of the solution containing Pd nanoparticles were mixed with 70 mL of an aqueous solution containing 3 g of KBr and 0.333 g of PVP. After heating to 90 °C, 30 mL of PtCl_4 ($3 \times 10^{-3} \text{ mol}\cdot\text{L}^{-1}$) were added (1 mL $\cdot\text{min}^{-1}$) under magnetic stirring (1200 rpm). Three synthesis durations were used to study the evolution of the particles and their performances: 0.6 h, 2 h and 8 h respectively. Subsequently, the particles were collected by centrifugation, washed several times with water as well as ethanol and dried in an oven at 70 °C.

2.3. Preparation of the Particles for the *In-Situ* XAFS and Electrochemical Measurements

To study the particles *in-situ* XAFS and electrochemical means, a mixture with carbon applying a particles-carbon weight ratio of 2:3 was used. The same method was used to coat the particles on carbon for all samples: A solution with 40 mg of particles in 25 mL of ethylene glycol was sonicated for 15 min and a second solution containing 60 mg of carbon Vulcan XC-72R powder diluted in 25 mL of ethylene glycol adjusted at pH 2 (with nitric acid solution), 2 mol $\cdot\text{L}^{-1}$ was sonicated for 30 min. Then, both solutions were mixed, sonicated for 1 h and kept one night under magnetic stirring. Afterwards, the mixture was heated to 40 °C and filtrated. Microfiltration was used to collect the particles coated on carbon, and they were dried for 5 h at 70 °C in an oven. After coating on carbon an ink was created by addition of 9 mg of particles coated on carbon in a solution containing 0.25 mL of water and 2.25 mL of isopropyl alcohol.

2.4. Electrochemical Measurement of the Catalytic Activity

All measurements were carried out in an electrochemical cell containing HClO_4 ($1 \times 10^{-1} \text{ mol}\cdot\text{L}^{-1}$) electrolyte with a platinum wire as counter electrode, a Hg/HgSO₄ (0.654 V vs. standard hydrogen electrode (SHE) in saturated KCl) reference electrode and a rotating disk electrode (Princeton Applied Research RDE 0008) with a geometric area of 0.196 cm² (diameter of 5 mm) as the working electrode. Before the measurements, the glassy carbon disk was polished, rinsed with deionized water, then cleaned ultrasonically in ultra-pure water for 15 min, and rinsed with isopropanol and acetone. After 15 min of sonication, 16 μL of ink containing the particles coated on carbon was deposited on the carbon disk, covered by 7 μL of a Nafion® solution (volumetric ratio of Nafion

to methanol was 1:100), and all was dried under ambient conditions. Prior to the measurement of the ORR, the electrode conditioning was conducted by cyclic voltammetry from 0.050 to 1.200 V (all the potentials are versus the SHE) with a scan rate of 0.100 V·s⁻¹ until reproducible voltammograms were obtained. The electrochemical performance for the oxygen reduction reaction (ORR) was determined using linear scan voltammetry (LSV) applied to the rotating disk electrode in the potential range from 0.300 to 1.200 V with a scan rate of 5 × 10⁻² V·s⁻¹ and a rotational speed of 1600 rpm, in a saturated electrolyte.

2.5. Characterization via TEM-EDS

The nanoparticles were studied using a high-resolution transmission electron microscope (HR-TEM) JEOL JEM-3010 operating at 300 keV and equipped with an X-Ray analyzer Oxford to perform energy dispersive spectroscopy (EDS) analysis. Just before the measurement, the homogenization of the aqueous solution containing nanoparticles was done by sonication. Subsequently, one drop of solution was deposited on a TEM grid (copper covered by a carbon film) and dried under vacuum.

2.6. XAFS Measurements

All XAFS experiments were performed at the Rossendorf Beamline (BM20) European Synchrotron Radiation Facility (ESRF), Grenoble, France. A water-cooled Si (111) double-crystal monochromator (DCM) was used to monochromatize the synchrotron beam. Before the DCM, collimation was done with a 1.0 m long, Pt-coated, meridionally bent silicon mirror. A second, 1.3 m long, Pt-coated, toroidal silicon mirror focused the beam vertically and horizontally after the DCM. The rejection of higher harmonics of the complete setup is better than 10⁻⁴. The measurements, in fluorescence mode, were done at room temperature using ionization chambers and a 13-elements high-purity germanium detector (Canberra) with a digital spectrometer (XIA X-Map).

For the XAFS measurements, pellets that were prepared from 1 g of particles coated on Vulcan XC72-R carbon powder (40wt.-% particles) and boron nitride for a higher stability were used. The particles were characterized using the Pt-L_{III} and Pd-K edges, providing information about the Pt-Pt edge, the Pd-Pd edge (Pd-K edge), and the Pt-Pd bond (Pt and Pd-K edge).

In-situ measurements were performed using a three electrodes system with a home-made cell filled with 8 mL of an HClO₄ (10⁻¹ mol·L⁻¹) aqueous solution. The counter electrode was a plain carbon cloth (0.5 cm × 2.5 cm) covered by conductive graphite, and an Ag/AgCl electrode was used as reference.

The working electrode was a plain carbon cloth covered by conductive graphite and was used to study the particles: 100 μL of the ink were deposited on the working electrode and then protected through the deposition of 16 μL of Nafion solution (ratio 1:100 Nafion: methanol). The area of the working electrode in solution was 0.52 cm². After 5 min of monitoring the open circuit potential and 80 cycles from 0.05 to 1.10 V at 0.1 V·s⁻¹, the measurements were done at differ-

ent potentials: 0.65, 0.85 V (oxidation), 1.20 V (vertex point), 1.00, 0.85, 0.65, 0.35 V (re-reduction) (Figure 1). For all measurements, the energy calibration, based on the average of several scans, and the dead-time correction of the fluorescence signals were done with the SixPack [16] software. Subsequent data reduction steps were performed with WinXAS [17]. For the normalization of the spectra, a first-order polynomial function was fitted to the pre-edge region, and a second-order polynomial function was fitted to the post-edge region.

Subsequently, the conversion from energies to photoelectrons kinetic energy units (k-space) was performed by arbitrarily assigning the first inflexion point of the absorption edge to zero energy. The auto-spline algorithm of WinXAS permitted the extraction of the EXAFS oscillations from the post-edge region by a spline fit. After k^{-1} weighting, the obtained EXAFS functions were Fourier-transformed to the R space using a Bessel window function across the k range from 2 to 12 Å⁻¹. The theoretical phase shift and amplitude functions for the shell fits were calculated using the FEFF 8.2 source code [18] based on Pt, Pt- and Pd metal clusters with face-centered cubic (fcc) structure. The shell fit was performed with WinXAS to derive coordination numbers (CN), interatomic distances (R), Debye-Waller factor and phase shift corrections (ΔE).

2.7. Analysis of Spectra via Principal Component Analysis, Varimax, and Iterative Target Transformation Factor Analysis

The evolution of the in-situ XAFS spectra was studied using a program developed by A. Rossberg, A. C. Scheinost [19] [20], permitting the analysis of the XAFS spectra via the Iterative Transformation Factor Analysis (ITFA) with a calculus of Varimax and Iterative Target Test (ITT). The first step of the ITFA is the Principal Component Analysis (PCA) [21]. The goal of the PCA is to identify the number of independent components that are required to reproduce the experimental spectrum. The work-flow uses the theoretical root mean square functions developed by Malinowski [22]: The real error (RE), the embedded (IE), and the semi-empirical indicator (INA). All these functions depend on the

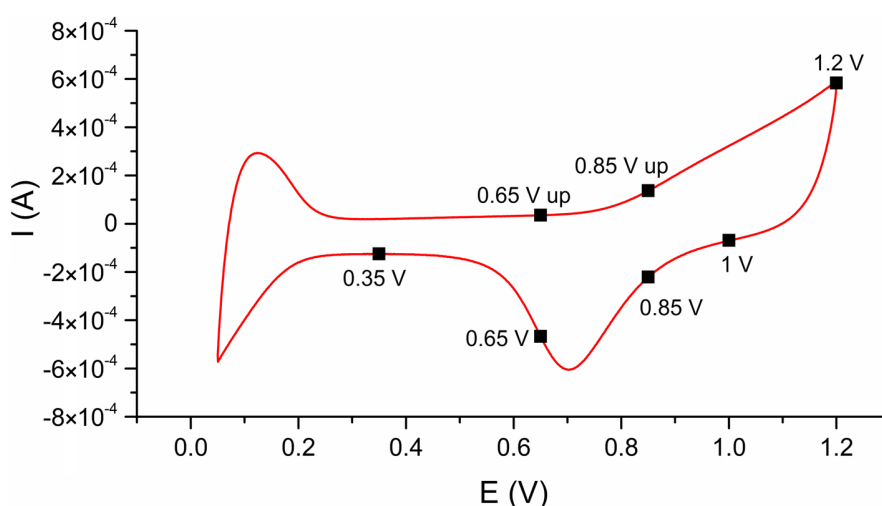


Figure 1. Standard ORR cycle and points used for the in-situ XAFS measurements.

number of components. Firstly, the eigenvectors and the factor loadings have to be set, representing the n -dimensional factor space with an orthogonal basis formed by the eigenvectors. For one sample, with seven spectra, the PCA is carried out with a factor loading of seven, the maximum number of components necessary to reconstruct the spectra. With the reduction of the dimensional factor, differences between the spectra, corresponding to the different components, become apparent. Finally, differences with a dimensional factor of two were found: Two main spectra (corresponding to two different components) permitted the reconstruction of the experimental spectrum of one sample. The other spectra are attributed to the experimental error and the noise. After the PCA and the reconstruction of the spectra, the evolution of the relative concentrations of the main components visible for the samples is followed using the Varimax method and the Iterative Target Test (ITT). The Varimax method, a statistical rotation method developed by H. F. Kaiser [23], aims at preferably high or low loadings for the factors of the linear combinations that resemble the different experimental spectra by rotation of the underlying n -dimensional space. Thus, an assignment of the single components of the spectra to the different spectra is possible, and, hence, the interpretation of the data becomes easier. Namely, applying the Varimax method allows the identification of correlations of the spectra with the different components. Using the spectra with the highest or lowest factor loading, the main components were identified and the ITT enabled the calculation of their relative concentrations.

3. Results and Discussion

3.1. TEM Images and EDS Measurements

The evolution of the shape of the particles, in particular their concavity, was monitored using TEM imaging (Figure 2). After 0.6 h, particles with a size of ca. 18 nm and a cubic shape were obtained. The formation of very thin layers that cover the cores of the cubes is apparent (darker edges in the TEM image). After 2 h, the particles feature a concave shape and contain more platinum, as evidenced from the lower contrast between the core and the external thicker layer. For the longest synthesis time, 8 h, the particles contain more platinum, but the shape

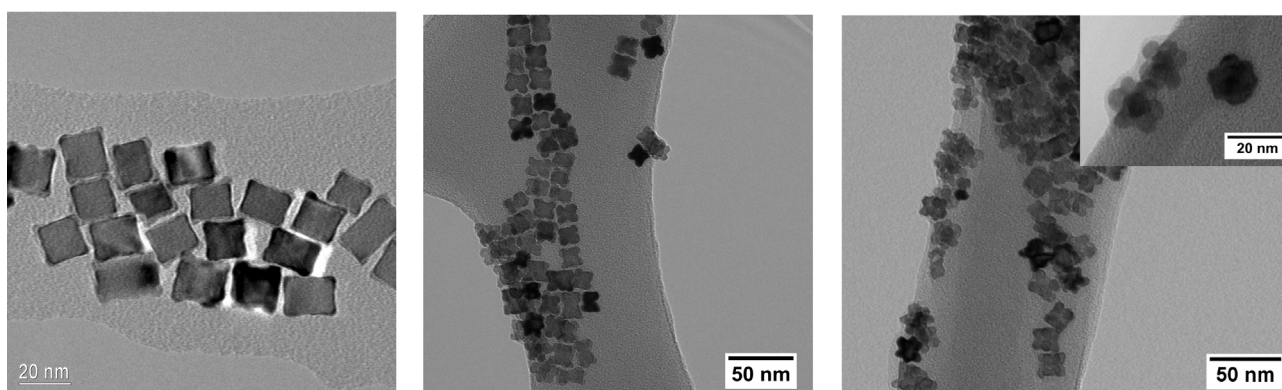


Figure 2. TEM images of 1) PtPd 0.6 h (left), PtPd 2 h (middle), PtPd 8 h (right).

of the particles are only negligibly different from those obtained after 2 h. However, additional larger, hexagonal structures with a small cubic, dark core (~ 1 nm) covered by a lighter layer to form hexagons were observed. With EDS measurements on different particles, from the dark core to the shell, an evolution of the chemical composition for the different particles is visible, with a higher concentration of Pt in the shell (lighter layer). These observations suggest the external layer is mainly constituted of platinum, while the core consists of palladium with a small amount of platinum. The particles mainly consist of palladium and show an increasing amount of platinum from 9% to 26% with increasing reaction time (Table 1). One high resolution EDS mapping can help to confirm this analysis.

3.2. EXAFS Measurements at the Pt-L_{III} and Pd-K Edges

After the Fourier transformation of the EXAFS spectra that were collected at the Pt-L_{III} edge, a well-defined double peak between 2 and 3 Å becomes apparent in all the particles (Figure 3). Modeling with FEFF using Pt and Pd clusters with

Table 1. Evolution of the amount of Pt and Pd in the particles measured by EDS.

Sample	Pt (wt.-%)	Pd (wt.-%)	Pt/Pd error (%)
0.6 h	8.6	91.4	9.9/2.8
2 h	19.1	81.0	5.9/8.3
8 h	26.4	73.6	8.1/7.6

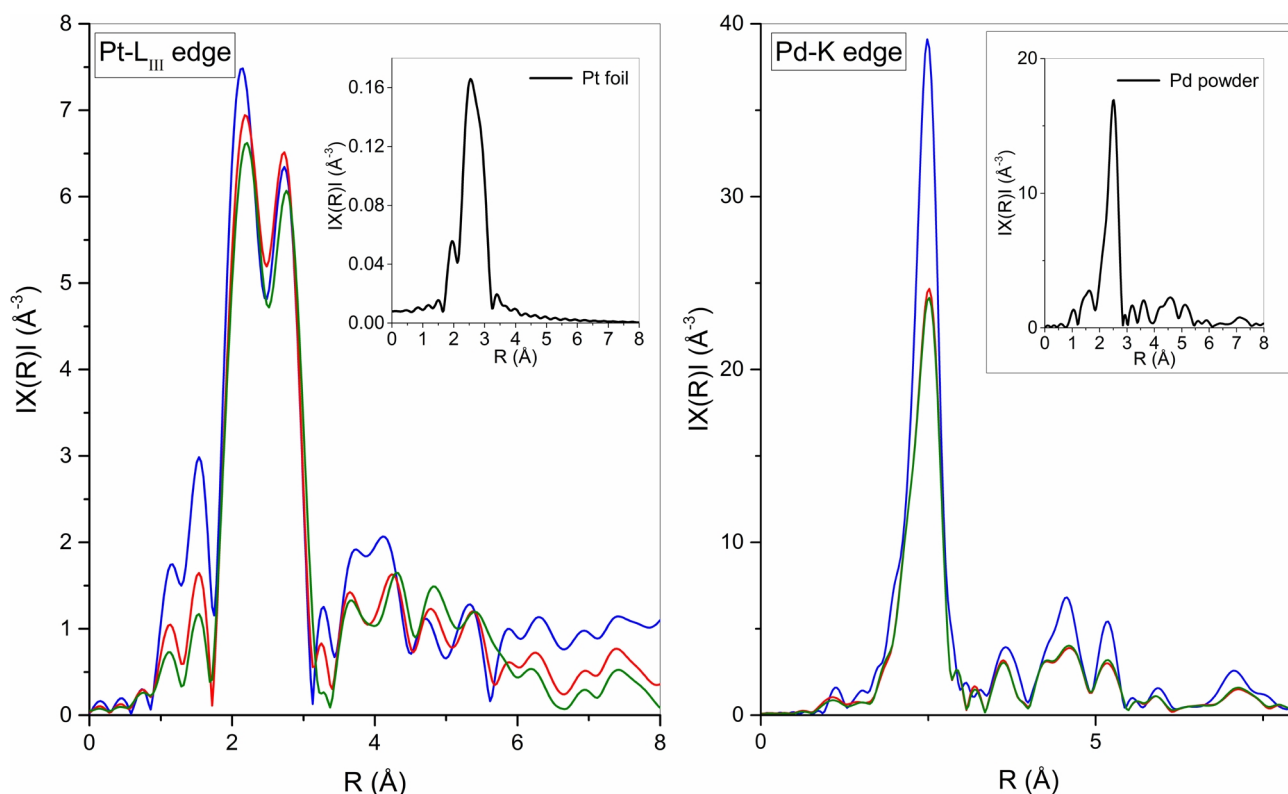


Figure 3. Fourier-transformed EXAFS spectra (uncorrected shift) of nanoparticles: 0.6 h (blue), 2 h (red), 8 h (green) at Pt-L_{III} and Pd-K edges.

Table 2. Coordination numbers (CN), interatomic distances (R), Debye-Waller factor (σ), and energy shifts (ΔE_0) achieved from the Pt-L₃ edge analysis.

Sample	Pt-Pt shell			Pt-Pd shell			ΔE_0 [eV]	R_{factor}^2 res (%)
	CN	R [Å]	σ [Å ²]	CN	R [Å]	σ [Å ²]		
0.6 h	6.7 Pt-Pt	2.72	0.0058	4.8 Pt-Pd	2.72	0.0058	5.9	5.4
2 h	6.2 Pt-Pt	2.73	0.0057	5.1 Pt-Pd	2.73	0.0057	7.1	4.0
8 h	7.3 Pt-Pt	2.74	0.0056	4.8 Pt-Pd	2.74	0.0056	7.7	2.2

Table 3. Coordination numbers (CN), interatomic distances R, Debye-Waller factor (σ), and energy shifts (ΔE_0) achieved from the Pd-K edge analysis.

Sample	Pd-Pt shell			Pd-Pd shell			ΔE_0 [eV]	R_{factor}^2 res (%)
	CN	R [Å]	σ [Å ²]	CN	R [Å]	σ [Å ²]		
0.6 h	0.6 Pd-Pt	2.71	0.0051	11.2 Pd-Pd	2.74	0.0009	9.1	0.3
2 h	1.4 Pd-Pt	2.71	0.0054	10.7 Pd-Pd	2.74	0.0054	5.4	1.6
8 h	1.7 Pd-Pt	2.70	0.0053	10.2 Pd-Pd	2.74	0.0053	5.1	1.3

different elemental ratios allows the attribution of this double peak to the presence of neighboring Pt and Pd in similar proportions in the first shell. Compared to the nanoparticles spectra, only one peak is visible for the Pt foil, which is in agreement with particles with only one type of neighbors, namely Pt atoms. In the Fourier-transformed Pd-K-edge spectra, the single main peak ($R \sim 2.74$ Å) suggests the predominance of only one type of neighboring atoms, most likely palladium.

The analysis of the obtained data with WinXAS software using models based on FEFF confirmed the first conclusions drawn from the experimental EXAFS spectra (Table 2).

The hypothesis of Pt atoms surrounded by platinum and palladium neighbors based on the Pt-L₃ edge spectra, is verified by the resulting equal distances between the Pt atoms and their neighbors of 2.72 to 2.74 Å.

These values are in line with the crystallographic data [24]. The Pt/Pd ratio is close to 1 and the sum of Coordination Numbers (CN) of Pt-Pt and Pt-Pd is close to 12 (considering an error of 25% for the CN).

With these results and the small Debye-Waller factors, indicating a small static and vibrational disorder, a shell possessing an fcc structure where platinum is surrounded by platinum and palladium atoms is most likely.

The analysis of the Pd-K edge spectra also yielded Pd-Pd distances for nanoparticles and for the reference of 2.74 Å, which is in agreement with theoretical values for the fcc structure [24]. The Pd-Pt interatomic distance is significantly smaller than the Pd-Pd distance (Table 3).

Compared to the Pt atoms, the coordination numbers, between 10.2 and 11.2 for the Pd-Pd bond, suggest the predominance of Pd atoms neighbored by other Pd atoms and only a small number of Pt atoms (CN between 0.6 and 1.7). The

different values determined by the fitting of the EXAFS curves for both Pt and Pd edges suggest that the nanoparticles possess a well-structured metal core of palladium where most of the Pd atoms have Pd neighbors, surrounded by a thin shell of Pt atoms where most of Pt atoms still have Pd neighbors.

3.3. In-Situ XAFS Studies

The modifications of the structure and composition of the PtPd nanoparticles with changing potential were studied. For every sample, spectra were measured at the characteristic potentials of the ORR cycle (cf. Figure 1) resulting in several spectra per sample. After in-situ measurements and the dead-time corrections using the SixPack software, the spectra were normalized and the functions were k^3 -weighted. Afterwards, the spectra were analyzed using Iterative Transformation Factor Analysis (ITFA).

By comparison with EXAFS standard spectra and modeling with FEFF, two components are assigned to the corresponding structures and chemical species, namely to a component with a Pt-O bond and to a component based on a Pt-Pt or Pt-Pd bond, which possess rather similar values. A measurement at the Pd-K edge could provide more information about the Pd-Pd and Pd-Pt bond.

The experimental spectra were reproduced applying the ITFA (Figure 4) with a combination of the two components (except for PtPd at 8 h) using a model, with a higher weight on the first component, suggesting a combination of Pt-O and Pt-Pd bonds within the samples. Regarding the measurements of Pt-Pd for the particles synthesized in 8 h, the experimental spectra can be reproduced with only one component, suggesting the presence of only one component and an insignificant amount of the second one, which is most likely the Pt-O component. The coordination numbers (CN), interatomic distances (R), Debye-Waller factors (σ^2), and energy shifts (ΔE) are presented in Table 4, the analysis of the spectra is shown in Figure 4. The FEFF model is suitable for the analysis of the

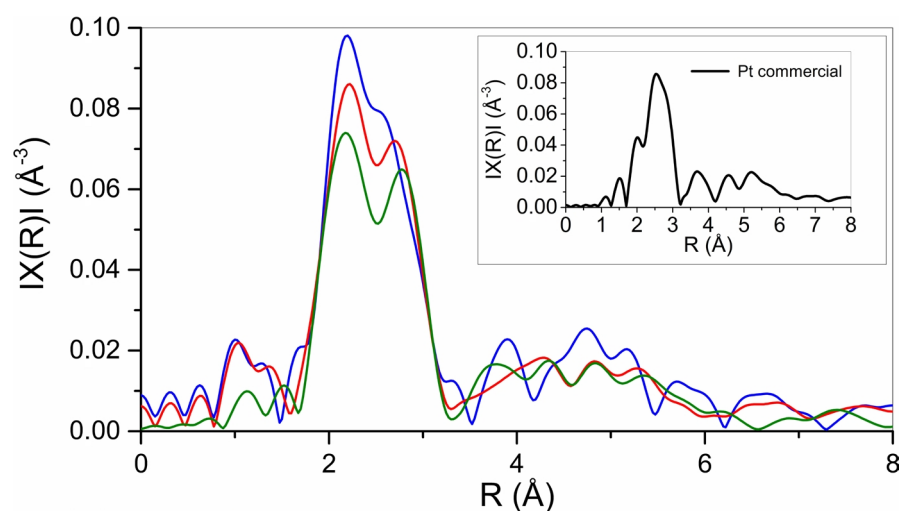


Figure 4. EXAFS spectra for the Pt-Pd nanoparticles at different synthesis times at 0.35 h (blue), 0.6 h (red), 2 h (green).

Table 4. Coordination numbers (CN), interatomic distances R, Debye-Waller factor (σ), and energy shifts (ΔE_0) from the Pt-L edge spectra at 0.35 V determined by curve fitting.

Sample	Pt-Pt shell			Pt-Pd shell			ΔE_0 [eV]	R_{factor}^2 res(%)
	CN	R [Å]	σ [Å ²]	CN	R [Å]	σ [Å ²]		
0.6 h	6.9 Pt-Pt	2.70	0.0021	5.1 Pt-Pd	2.70	0.0030	5.0	1.4
2 h	7.4 Pt-Pt	2.72	0.0019	4.6 Pt-Pd	2.71	0.0022	6.4	2.3
8 h	7.6 Pt-Pt	2.72	0.0015	4.4 Pt-Pd	2.71	0.0030	6.3	2.1
Pt commercial	12 Pt-Pt	2.74	0.0080				7.2	4.6

experimental data with only small residuals. The small Debye-Waller factors indicate insignificant vibrational and static disorder, pointing particles with well-defined structure. The determined values (Table 4) are similar to the values achieved from the ex-situ XAFS spectra (Table 2 and Table 3). Notably, for the ex-situ and, the in-situ XAFS spectra at 0.35 V, the peak that corresponds to the Pt-O bond ($R \sim 1.8$ Å) is not visible and the spectra can be fitted assuming only Pt, Pt-Pd and Pd metal clusters with face-centered cubic (fcc) structure using WinXAS software. Thus, the absence of oxide at an applied potential of 0.35 V is confirmed.

3.4. Evolution of the Structure with the Applied Potential

After the PCA, the reconstruction of the spectra (XANES and EXAFS) using two principal components (Pt metal and Pt oxide) allows the monitoring of the evolution of the samples with changing potential (Figure 5). The FEFF-based model of a Pt oxide cluster yields a peak at ~ 2 Å, corresponding to a theoretical length of the Pt-O bond of 2 Å.

For all samples (excluding the PtPd 8-h NPs), the Fourier-transformed EXAFS spectra feature a peak at $R \sim 1.8$ Å, which appears and disappears with the different potentials, while the inverse behavior occurs for the double peak between 2 and 3 Å, which is attributed to the Pt-Pd and Pt-Pt bond (only Pt-Pt for the commercial platinum). From 0.85 to 0.35 V, the single peak vanishes, and reappears when the potential reaches 0.85 V again. Comparing the results with the Pt oxide model achieved from FEFF and the EXAFS database, this peak was assigned to the Pt-O bond. This suggests the formation of a thin layer of Pt oxide with oxygen atoms adsorbed on the surface of the particles when the potential is higher than 0.85 V. At 1.0 V and at Figure 5), the peak corresponding to the Pt-O bond appears very distinctively in the spectra, except for the 8 h NP. These results are confirmed by the analysis of the experimental EXAFS curves using an FEFF model with Pt-Pt, Pt-Pd, and Pt oxide clusters (Table 5). For the commercial Pt, two Pt-Pt bonds were used for the curve fitting: One Pt-Pt bond (path 1) for pure Pt nanoparticles and a second one (path 2) corresponding to the Pt nanoparticles with Pt oxide. The results of the curve fitting (Table 5), including the Pt oxide in the model, are validated by small residual factors. Like for the EXAFS spectra measured at 0.35 V, the particles are well structured.

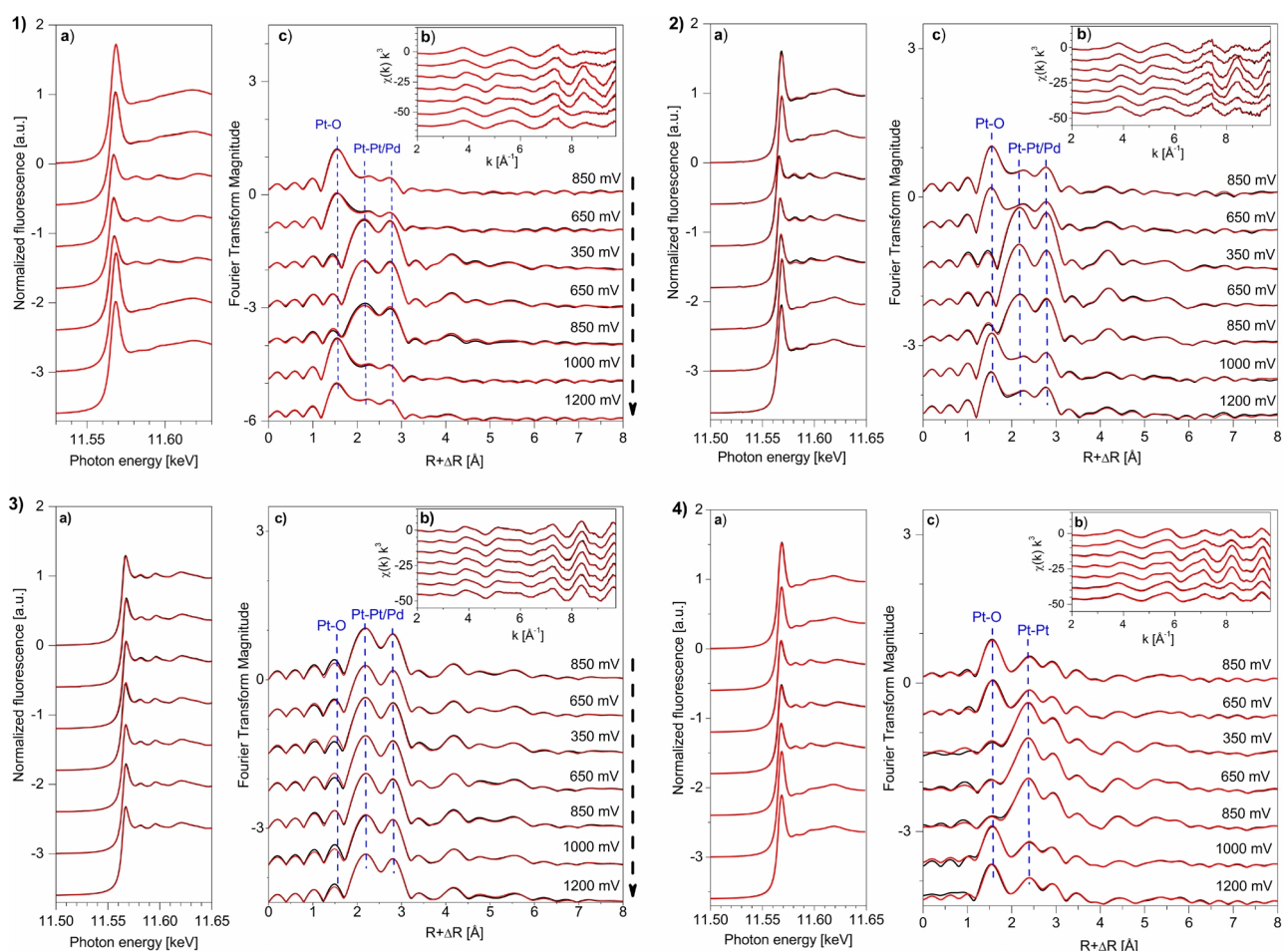


Figure 5. Experimental (black) and reconstruction (red) of XANES (left), EXAFS (insert) and Fourier transformed EXAFS (right) for the different potentials: (1) 0.6 h, (2) 2 h, (3) 8 h, (4) Pt commercial.

Table 5. Structural parameters of the particles at 1 V, Pt-L

Sample	Pt-Pt shell			Pt-O shell			Pt-Pd shell			ΔE_0 [eV]	R_{factor}^2 (%)
	CN	R [Å]	σ [Å ²]	CN	R [Å]	σ [Å ²]	CN	R [Å]	σ [Å ²]		
Pt _{commercial} Path 1	6 Pt-Pt	2.74	0.0091	0 Pt-O	0	0.0000	0.0		0.0000	9.5	5.43
Pt _{commercial} Path 2	7 Pt-Pt	3.08	0.0275	2.2 Pt-O	1.99	0.0046	0.0		0.0000	9.5	5.43
0.6 h	7.4 Pt-Pt	2.66	0.0129	3.6 Pt-O	1.98	0.0065	1.7 Pt-Pd	2.70	0.0065	6.2	4.43
2 h	9.7 Pt-Pt	2.69	0.0178	2.4 Pt-O	1.99	0.0022	2.7 Pt-Pd	2.75	0.0092	6.6	3.76
8 h	7.6 Pt-Pt	2.74	0.0040	0 Pt-O	0.00	0.0000	4.0 Pt-Pd	2.74	0.0041	6.9	0.23

with small Debye-Waller factors. For the Pt-Pt shell, these factors are higher at 1.00 V than at 0.35 V for all the particles (excepted for the 8 h NPs), which could be due to the presence of Pt oxide, causing a disorder in the shell structure of the particles.

The lengths of the Pt-O bond, close, (~ 1.99 Å), are close to the theoretical value (2.07 Å) but the CN are smaller (CN = 6 in theory for pure Pt oxide). This is most likely due to the Pt oxide present at 1.00 V, unstructured compared to the Pt and Pd atoms well organized in a fcc crystalline system. Considering the

experimental errors, the lengths of the Pt-Pt and PtPd bonds are close to theoretical values (2.807 Å for the Pt-Pt bond and for the Pt-Pd bond) and to the bond length at 0.35 V. For the PtPd nanoparticles after 0.6 h and 2 h, the double peak shows a slight asymmetry with a higher peak height at 2.2 Å, which occurs for small potentials and disappears progressively with increasing potential. This was also observed by other researchers working on PtPd nanoparticles [25]. For the PtPd nanoparticles at 8 h, no significant changes are present and the spectrum can be reproduced with only one component. Thus, due to the lack of change with changing potential, the formation of an oxide layer is highly unlikely for these particles.

3.5. Studying the Relative Concentrations with the ITFA

For the systems based on two components, these were assigned to the oxide and the metal and the changes of their relative concentrations with changing potential were examined. The concentrations were normalized using the achieved concentration of the commercial Pt sample, presuming that only one metallic component is present and that the surface is constituted of pure platinum metal when the applied potential is 0.35 V and of platinum oxide when the potential is 1.00 V, as is stated in the related literature [26] [27] [28].

Like that, the evolution of the relative concentrations was monitored: When the potential is decreasing, the concentration of metal is increasing while, in contrast, the concentration of the oxide is increasing with increasing potential, which was already observed in former studies on Pt and PtPd nanoparticles [25]. Obviously, the PtPd NP after 8 hours, whose spectra are only on one component, cannot be analyzed using this model.

3.6. The ORR: Different Chemical Processes

For the oxygen reduction reaction, two main mechanisms are suggested: An a

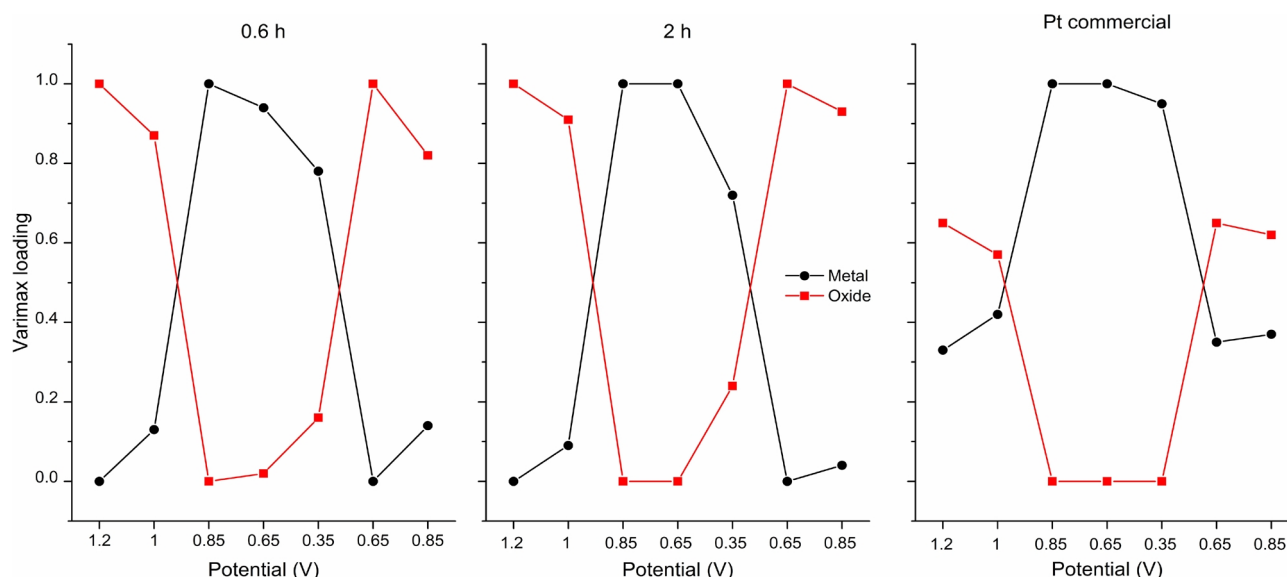
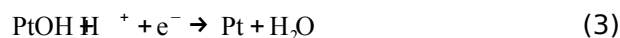
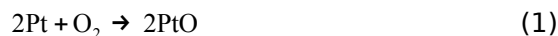


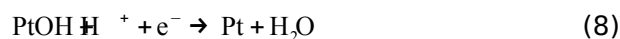
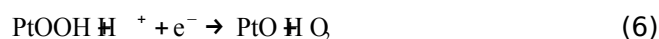
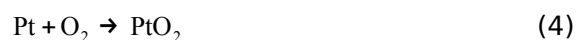
Figure 6. Evolution of the relative concentrations with the potential.

sociative and a dissociative one [26] [28] [29].

Dissociative ORR mechanism



Associative ORR mechanism



The first step of the associative mechanism is the adsorption of oxygen at the active sites of the electrode conserving the O-O bond, in contrast to the dissociative mechanisms, where the bond between the oxygen atoms is broken before adsorption on the electrode. The last steps of both mechanisms (Equations ((2), (3), (7), and (8))) are equal and, at higher potentials, both mechanisms can occur. As already stated, above 0.85 V, the XPS measurements suggest the presence of Pt-O bonds. Up to 1.00 V, the amount of oxide is increasing accompanied by a high degree of surface oxidation [30], the relative concentration of the oxide determined using the Varimax method for our experimental data analysis is close to 1 while it is 0 for the metal.

3.7. Catalytic Activity of the Particles

The mass activity (MA), relative to the mass of catalyst loaded for the electrochemical oxygen reduction, was determined using linear sweep voltammetry with a rotating disk electrode (RDE). The rotation of the electrode ensures fast and effective convective transport of the electroactive species. The MA is related to the kinetic current density at 0.85 V, where the electrochemical processes are controlled by the electron transfer. According to the Koutecký-Levich equation, j_k is defined by:

$$1/j = 1/j_k + 1/j_d \quad (9)$$

where j is the total current density (measured at 0.85 V) and j_d is the diffusion-controlled current density (measured at 0.40 V). The mass activity (MA) is calculated from the kinetic current density relative to the mass of the nanoparticles m_{NP} deposited at the surface of the RDE:

$$MA = j_k / m_{NP} \quad (10)$$

The resulting mass activities of the different samples are summarized in Table 6.

The achieved mass activities are similar to reported values for Pt and Pt-Pd nanoparticles used as catalyst for the ORR [31] [32]. According to the

Table 6. Catalytic activity for the different samples.

Sample	0.6 h	2 h	8 h	Pt _{commercial}
Mass activity (A/g)	17.4	25.9	8.8	18.7

mental results, the Pt-Pd nanoparticles synthesized in 2 h represent the best system for the ORR catalysis, with a mass activity superior to the commercial Pt, and the performances of the particles synthesized in 0.6 h are rather good. Compared to the other samples, the 8 h NPs show a lower catalytic activity. With a smaller amount of platinum than the pure powder, the PtPd NPs at 0.6 h and the PtPd NPs at 2 h feature a good performance as catalysts for the ORR. The cubic shape of the particles and the Pt-Pd alloy on the surface of the particles may be the reason for their catalytic performance, with a higher electrochemical surface area and a beneficial composition of the alloy (Pt/Pd ratio) for the ORR.

Similar results have been found by other researchers suggesting an influence of the composition of the alloy [14] [33].

4. Conclusion

The behavior and performance regarding the oxygen reduction reaction (ORR) was studied for different PtPd nanoparticles by means of electrochemical and *in situ* XAFS measurements. For the latter, different electrochemical potentials were applied to reveal differences between the XAFS spectra of the different ORR steps. Iterative Transformation Factor Analysis (ITFA) was used to analyze the achieved experimental data. As the first step, the Principal Component Analysis (PCA) of the spectra, showed two main components, Pt or Pt-Pd in a metallic and in an oxide form, which allowed the reproduction of the experimental spectra. Continuing the ITFA using the Varimax method and the Iterative Target Test (ITT), the evolution of the relative concentrations of the different forms of the particles was monitored. The oxide appears at potentials from 0.65 V and, is the main form up to 1.00 V. For the metallic species, the relative concentration is increasing with decreasing potentials down to 0.3 V where it is the major component. The development of the structural parameters (CN, σ , R) was calculated by analysis of the measured curves using WinXAS with Pt-Pd and PtO models that had been achieved through the FEFF code. The resulting values are in agreement with the results of the *in situ* XAFS measurements at the Pd-K edge would be helpful to gain information about the formation of Pd oxide during the ORR. Linear scanning voltammetry was used to evaluate the electrochemical performance of the different particles. However, characterization of the particles with other methods (X-ray photoelectron spectroscopy, impedance spectrometry) is required to receive more detailed and more meaningful correlations between the nanoparticles' structures and their catalytic activities.

Acknowledgements

We thank the research group working at the Rossendorf Beamline BM20A in the

ESRF (Grenoble, France), Dr. Stephanie Höppener for EDS mapping, Dr. Igor Perevyazko for his help and access to a high-speed centrifugation, and workshop of the university for the participation in the fabrication of the experimental cell. This work was carried out with the financial support of the Zeiss Foundation (Germany).

References

- [1] Nogami, M. et al. (2010) Synthesis of Porous Single-Crystalline Platinum Nanocubes Composed of Nanoparticles. *Journal of Physical Chemistry Letters* 1, 568-571. <https://doi.org/10.1021/jz900342q>
- [2] Ojani, R., Valiollahi, R. and Raouf, J.B. (2014) Comparison between Graphene Supported Pt Hollow Nanospheres and Graphene Supported Pt Solid Nanoparticles For Hydrogen Evolution Reaction. *Energy* 74, 871-876. <https://doi.org/10.1016/j.energy.2014.07.062>
- [3] Bele, M. et al. (2014) A Highly Active Pt-Cu Intermetallic Core-Shell, Multilayered Pt-Skin, Carbon Embedded Electrocatalyst Produced by a Scale-Up Sol-Gel Synthesis. *Chemical Communications* 13124-13126. <https://doi.org/10.1039/C4CC05637J>
- [4] Du, S., Lu, Y. and Steinberger-Wilckens, R. (2014) PtPd Nanowire Arrays Supported on Reduced Graphene Oxide as Advanced Electrocatalysts for Methanol Oxidation. *Carbon* 79, 346-353. <https://doi.org/10.1016/j.carbon.2014.07.076>
- [5] Mu, R., Guo, X., Fu, Q. and Bao, X. (2011) Oscillation of Surface Structure and Reactivity of PtNi Bimetallic Catalysts with Redox Treatments at Variable Temperatures. *Journal of Physical Chemistry Letters* 2, 20590-20595. <https://doi.org/10.1021/jp206517r>
- [6] Bing, Y., Liu, H., Zhang, L., Ghosh, D. and Zhang, J. (2010) Nanostructured Pt-Alloy Electrocatalysts for PEM Fuel Cell Oxygen Reduction. *Chemical Society Reviews* 39, 2184-2202. <https://doi.org/10.1039/b912552c>
- [7] An, W. and Liu, P. (2013) Size and Shape Effects of Pd@Pt Core-Shell Nanoparticles: Unique Role of Surface Contraction and Local Structural Flexibility. *Journal of Physical Chemistry Letters* 4, 16144-16149. <https://doi.org/10.1021/jp4057785>
- [8] Zhang, H. et al. (2011) Facile Synthesis of Pd-Pt Alloy Nanocages and Their Enhanced Performance for Preferential Oxidation of CO in Excess Hydrogen. *Nano* 5, 8212-8222. <https://doi.org/10.1021/nn202896q>
- [9] Halder, A., Jia, Q., Trahan, M. and Mukerjee, S. (2013) X-Ray Absorption Spectroscopy Probing the Enhanced Electrochemical Activity of Ternary PtRu@Pb Catalysts. *Electrochimica Acta* 108, 288-295. <https://doi.org/10.1016/j.electacta.2013.06.087>
- [10] Wiltshire, R.J.K. et al. (2005) A PEM Fuel Cell for *Situ* XAS Studies. *Electrochimica Acta* 50, 5208-5217. <https://doi.org/10.1016/j.electacta.2005.05.038>
- [11] Carvalho, A.R., Wattoom, J., Zhu, L. and Breerton, R.G. (2006) Combined Kinetics and Iterative Target Transformation Factor Analysis for Spectroscopic Monitoring of Reactions. *Analyst* 131, 90-97. <https://doi.org/10.1039/B510875F>
- [12] Huang, X. et al. (2012) Synthesis of PtPd Bimetal Nanocrystals with Controllable Shape, Composition, and Their Tunable Catalytic Properties. *Nanoparticles* 2, 4265-4270. <https://doi.org/10.1021/nl301931m>
- [13] Chu, Y.Y., Wang, Z.B., Jiang, Z.Z., Gu, D.M. and Yin, G.P. (2012) Facile Synthesis of Hollow Spherical Sandwich PtPd/C Catalyst by Electrostatic Self-Assembly

- Polyol Solution for Methanol Electrooxidation. *Journal of Power Sources* 2011, 22, 17-25. <https://doi.org/10.1016/j.jpowsour.2011.11.025>
- [14] Hong, J.W. et al. (2012) Controlled Synthesis of Pd-Pt Alloy Hollow Nanostructures with Enhanced Catalytic Activities for Oxygen Reduction. *ACS Nano*, 6, 2410-2419. <https://doi.org/10.1021/nn2046828>
- [15] Zhang, H. et al. (2011) Synthesis of Pd-Pt Bimetallic Nanocrystals with a Concave Structure through a Bromide-Induced Galvanic Replacement. *ACS Nano* 133, 6078-6089. <https://doi.org/10.1021/ja201156s>
- [16] Webb, S.M. (2005) SIXPack: A Graphical User Interface for XAS Analysis Using IFEFFIT. *Physica Scripta* 115, 1011-1014. <https://doi.org/10.1238/physica.topical.115a01011>
- [17] Ressler, T. (1998) WinXAS: A Program for X-ray Absorption Spectroscopy Data Analysis under MS-Windows. *Journal of Synchrotron Radiation* 5, 116-122. <https://doi.org/10.1107/S0909049597019298>
- [18] Ankudinov, A.L. and Rehr, J.J. (1997) Relativistic Calculations of Spin-Dependent X-Ray-Absorption Spectra. *Physical Review B* 56, R1712-R1716. <https://doi.org/10.1103/physrevb.56.r1712>
- [19] Rossberg, A. and Scheinost, A.C. (2005) Three-Dimensional Modeling of EXAFS Spectral Mixtures by Combining Monte Carlo Simulations and Target Transformation Factor Analysis. *Analytical and Bioanalytical Chemistry* 383, 56-66. <https://doi.org/10.1007/s00216-005-3369-z>
- [20] Rossberg, A. et al. (2009) Identification of Uranyl Surface Complexes on Ferrihydrite: Advanced EXAFS Data Analysis and CD-MUSIC Modeling. *Environmental Science & Technology* 43, 1400-1406. <https://doi.org/10.1021/es801727w>
- [21] Abdi, H. and Williams, L.J. (2010) Principal Component Analysis. *Computational Statistics* 25, 433-459. <https://doi.org/10.1002/wics.101>
- [22] Malinowski, E.R. and Howery, D.G. (1980) *Factor Analysis in Chemistry*. Wiley Interscience, New York.
- [23] Kaiser, H.F. (1958) The Varimax Criterion for Analytic Rotation in Factor Analysis. *Psychometrika* 23, 187-200. <https://doi.org/10.1007/BF02289233>
- [24] Gražulis, S. et al. (2012) Crystallography Open Database (COD): An Open-Access Collection of Crystal Structures and Platform for World-Wide Collaboration. *Nucleic Acids Research* 40, 420-427. <https://doi.org/10.1093/nar/gkr900>
- [25] Nagamatsu, S. et al. (2013) Potential-Dependent Restructuring and Hysteresis in the Structural and Electronic Transformations of Pt/C, Au(Core)-Pt(Shell)/C, and Pd(Core)-Pt(Shell)/C Cathode Catalysts in Polymer Electrolyte Fuel Cells Characterized by In Situ X-ray Absorption Fine Structure. *Journal of Physical Chemistry C* 117, 13094-13107. <https://doi.org/10.1021/jp402438e>
- [26] Gómez-Marín, A.M., Rizo, R. and Feliu, J.M. (2013) Some Reflections on the Understanding of the Oxygen Reduction Reaction at Pt. *Journal of Nanotechnology* 2013, 956-967. <https://doi.org/10.3762/bjnano.4.108>
- [27] Antoine, O., Bultel, Y. and Durand, R. (2001) Oxygen Reduction Reaction Kinetics and Mechanism on Platinum Nanoparticles inside Nanotubes. *Journal of Electroanalytical Chemistry* 499, 85-94. [https://doi.org/10.1016/S0022-0728\(00\)00492-7](https://doi.org/10.1016/S0022-0728(00)00492-7)
- [28] Song, C. and Zhang, J. (2008) *PEM Fuel Cell Electrocatalysts and Catalyst Layers*. Springer-Verlag, London, 89-134. https://doi.org/10.1007/978-1-84800-936-3_2
- [29] Nørskov, J.K. et al. (2004) Origin of the Overpotential for Oxygen Reduction at a Fuel-Cell Cathode. *Journal of Physical Chemistry B* 108, 17886-17892. <https://doi.org/10.1021/jp047349j>

- [30] Jacob, T. (2007) Theoretical Investigations on the Potential-Induced Formation of Pt-Oxide Surfaces. *Journal of Electroanalytical Chemistry*, 607, 158-166.
<https://doi.org/10.1016/j.jelechem.2007.03.023>
- [31] Park, J.H., Sohn, Y., Jung, D.H., Kim, P. and Joo, J.B. (2016) Pt deposited Pt-Pd/C Electrocatalysts with the Enhanced Oxygen Reduction Activity. *Journal of Industrial and Engineering Chemistry*, 36, 109-115. <https://doi.org/10.1016/j.jiec.2016.01.039>
- [32] Li, H., et al. (2007) Design and Preparation of Highly Active Pt-Pd/C Catalyst for the Oxygen Reduction Reaction. *Journal of Physical Chemistry*, 111, 5605-5617.
<https://doi.org/10.1021/jp067755y>
- [33] Liu, L., et al. (2012) Enhanced Oxygen Reduction Reaction Activity and Characterization of Pt-Pd/C Bimetallic Fuel Cell Catalysts with Pt-Enriched Surfaces in Acid Media. *Journal of Physical Chemistry*, 116, 23453-23464.
<https://doi.org/10.1021/jp308021a>



Scientific Research Publishing

Submit or recommend next manuscript to SCIRP and we will provide best service for you:

Accepting pre-submission inquiries through Email, Facebook, LinkedIn, Twitter, etc.
A wide selection of journals (inclusive of 9 subjects, more than 200 journals)
Providing 24-hour high-quality service
User-friendly online submission system
Fair and swift peer-review system
Efficient typesetting and proofreading procedure
Display of the result of downloads and visits, as well as the number of cited articles
Maximum dissemination of your research work

Submit your manuscript at: <http://papersubmission.scirp.org/>
Or contact anp@scirp.org